UNIVERSITY OF CALIFORNIA SAN DIEGO

Comprehensive analysis of left ventricular cardiac function using 4DCT data

A dissertation submitted in partial satisfaction of the

requirements for the degree Doctor of Philosophy

in

Bioengineering

by

Gabrielle Marie Colvert

Committee in charge:

Professor Elliot McVeigh, Chair
Professor Francisco Contijoch
Professor Anthony DeMaria
Professor Andrew McCulloch
Professor Jeff Omens
Professor Daniela Valdez-Jasso

2021

The Dissertation of Gabrielle Marie Colvert is approved, and it is acceptable in quality and form for publication on microfilm and electronically.

University of California San Diego

2021

DEDICATION

To my family for their unconditional love and support through it all.

TABLE OF CONTENTS

LIST OF ABBREVIATIONS

4DCT: 4D X-ray Computed Tomography

AHA: American Heart Association

AS: Aortic Stenosis

AUC: Area Under the Curve

CAD: Coronary Artery Disease

CMR: Cardiac Magnetic Resonance Imaging

CNR: Contrast-to-Noise Ratio

CPD: Coherent Point Drift

CRT: Cardiac Resynchronization Therapy

CTA: Computed Tomography Angiography

CURE: Circumferential Uniformity Ratio Estimate

DLP: Dose Length Product

E_{cc}^{CT}: 4DCT-derived regional endocardial circumferential strain

E_{ll}^{CT}: 4DCT-derived regional endocardial longitudinal strain

ECG: Electrocardiogram

Echo: Echocardiography

ED: End-Diastole/End-Diastolic

EDV: End-Diastolic Volume

EF: Ejection Fraction

ES: End-Systole/End-Systolic

ESV: End-Systolic Volume

GCS: Global Circumferential Strain

GLS: Global Longitudinal Strain

LA: Left Atrium

LAA: Left Atrial Appendage

LAX: Long Axis

LBBB: Left Bundle Branch Block

LDA: Linear Discriminant Analysis

LGE: Late Gadolinium Enhancement

LPS: Lead Placement Score

LV: Left Ventricle/Left Ventricular

LVOT: Left Ventricular Outflow Tract

MACE: Major Adverse Cardiac Event

MI: Myocardial Infarction

ML: Maximum Likelihood

MR: Mitral Regurgitation

NPV: Negative Predictive Value

NYHA: New York Heart Association

PCA: Principal Component Analysis

PPV: Positive Predictive Value

PSF: Point Spread Function

ROC: Receiver Operating Characteristic

RS_{CT}: CT Regional Endocardial Shortening

RV: Right Ventricle/Right Ventricular

SAX: Short Axis

SNR: Signal-to-Noise Ratio

TAVR: Transcatheter Aortic Valve Replacement

TMVI: Transcatheter Mitral Valve Implantation

TOS: Time to Onset of Shortening

WMA: Wall Motion Abnormality

LIST OF FIGURES

LIST OF TABLES

ACKNOWLEDGEMENTS

I would like to thank my family most especially. Without them, this work would not have been possible. When the going got tough, you helped me keep going.

Thank you to my thesis advisor, Dr. Elliot McVeigh, for his mentorship and guidance over the past five years. Thank you for all the insightful conversations and for the encouraging words of support, even when I could not see the value in my results.

I would also like to thank all the members of the Cardiovascular Imaging Lab for their guidance, helpful discussions, friendship, and many happy hours. I will miss our teatime chats and our lunchtime World Cup viewing parties. I do hope you keep the tradition alive!

I would like to thank the NIH NHLBI, the ARCS Foundation, and the Siebel Scholars foundation for not only their financial support during my time as a graduate student but for allowing me to a part of their inspiring communities.

Chapters 1 and 2, in part, has currently been submitted for publication of the material, Gabrielle M. Colvert, Ashish Manohar, Francisco J. Contijoch, James Yang, Jeremy Glynn, Philipp Blanke, Jonathon A. Leipsic, Elliot R. McVeigh. “Novel 4DCT method to measure regional left ventricular endocardial shortening before and after transcatheter mitral valve implantation.” The dissertation author was a primary author of this paper.

Chapters 1 and 3, in part, are currently being prepared for submission for publication of the material, Gabrielle M. Colvert, Ashish Manohar, Brendan T. Colvert, Zhennong Chen, Chansu Kim, James Yang, Andrew Schluchter, Maria Ledesma-Carbayo, Anders S. Knudsen, Jens C. Nielsen, Elliot R. McVeigh. “Predicting 6-month post CRT outcomes using 4DCT-derived metrics of left ventricular shape, function, and dyssynchrony.” The dissertation author was a primary author of this paper.

Chapters 4, 5, and 7, in part, are a reprint of the material as it is published in: Gabrielle M. Colvert, Juan E. Ortuño, W. Patricia Bandettini, Marcus Y. Chen, Maria J. Ledesma-Carbayo, Elliot R. McVeigh. “4DCT-derived Endocardial Left Ventricular Torsion Correlated with CMR

Tagging-derived Torsion in the Same Subjects." in JACC: Cardiovascular Imaging (2020). The dissertation author was a primary author of this paper.

Chapters 4, 5 and 7, are in part a reprint of the material as it is published in: Gabrielle M. Colvert, Ashish Manohar, Brendan T. Colvert, Andrew Schluchter, Francisco J. Contijoch, Elliot R. McVeigh. "Novel measurement of LV twist using 4DCT: quantifying accuracy as a function of image noise." in Proc. SPIE 10953, Medical Imaging 2019: Biomedical Applications in Molecular, Structural, and Functional Imaging. The dissertation author was a primary author of this paper.

Chapters 4 and 6, in part, has currently been submitted for publication of the material, Gabrielle M. Colvert, Ashish Manohar, Brendan T. Colvert, Juan E. Ortuño, Zhennong Chen, James Yang, W. Patricia Bandettini, Marcus Y. Chen, Maria J. Ledesma-Carbayo, Elliot R. McVeigh. "Regional left ventricular endocardial strain from 3D deformations fields derived from 4DCT images." The dissertation author was a primary author of this paper.

VITA

2016 BS in Biomedical Engineering at the University of Southern California

2018 MS in Bioengineering at the University of California San Diego

2021 PhD in Bioengineering at University of California San Diego

PUBLICATIONS

G. M. Colvert, A. Manohar, F. J. Contijoch, J. Yang, J.Glynn, P. Blanke, J. A. Leipsic & E. R. McVeigh, "Novel 4DCT Method to Measure Regional Left Ventricular Endocardial Shortening Before and After Transcatheter Mitral Valve Implantation," *Structural Heart*, May 2021, DOI: 10.1080/24748706.2021.1934617

G.M. Colvert, J.E. Ortuño, W.P. Bandettini, M.Y. Chen, M.J. Ledesma-Carbayo, E.R. McVeigh, "4DCT-derived endocardial left ventricular torsion correlates with CMR-tagging derived torsion in the same subjects," *JACC: Cardiovasc Imag*, July 2020, DOI: 10.1016/j.jcmg.2020.05.022

A. Manohar, **G.M. Colvert**, A. Schluchter, F. Contijoch, E.R. McVeigh, "Anthropomorphic left ventricular mesh phantom: a framework to investigate the accuracy of SQUEEZ using Coherent Point Drift for the detection of regional wall motion abnormalities," *J of Med Imag*, December 2019

A. Manohar, L. Rossini, **G.M. Colvert**, D.M. Vigneault, F. Contijoch, M.Y. Chen, J.C. del Alamo, E.R. McVeigh, "Regional dynamics of fractal dimension of the left ventricular endocardium from cine computed tomography images," *J of Med Imag*, November 2019

G.M. Colvert, A. Manohar, B.T. Colvert, A. Schluchter, F. Contijoch, E.R. McVeigh, "Novel Measurement of LV twist using 4DCT: quantifying accuracy as a function of image noise," *Proc. SPIE Medical Imaging,* March 2019

ABSTRACT OF THE DISSERTATION

Comprehensive analysis of left ventricular cardiac function using 4DCT data

by

Gabrielle Marie Colvert

Doctor of Philosophy in Bioengineering

University of California San Diego, 2021

Professor Elliot McVeigh, Chair

The increased complexity of percutaneous procedures continues to demand new imaging techniques to assist these interventions and improve clinical planning and outcomes. Recent developments in 4D X-ray computed tomography (4DCT) technology, including dose reduction protocols, iterative reconstruction methods, and wide-range detectors, allow for full 3D volumes to be acquired across the entire cardiac cycle within a single heartbeat with very low radiation dose. In addition, with the use of a contrast bolus, 4DCT provides highly reproducible and high-resolution metrics of left ventricular (LV) endocardial function. This dissertation thoroughly investigates the development and application of novel methods for evaluating both global and regional LV function using 4DCT data. These novel methods present highly translational research

which can be implemented immediately on many existing CT scanners as well as on existing datasets, retrospectively. First, we evaluate the accuracy and reproducibility of previously developed and validated metrics, like CT SQUEEZ, and newly proposed algorithms for measuring LV rotation, torsion, longitudinal strain, and circumferential strain through phantom experiments and cross-modality comparison studies. Then, we demonstrate the feasibility of these methods in patients with various cardiovascular disease states, such as mitral regurgitation (MR) and heart failure. In transcatheter mitral valve (TMVI) patients we show that analysis of 4DCT-derived metrics of LV function can provide a more precise understanding of the effect of MR and TMVI on regional LV function and remodeling than current imaging methods. In heart failure patients, we show that 4DCT-derived metrics of LV shape, global and regional LV function, and dyssynchrony have the potential to predict response to cardiac resynchronization therapy (CRT) through the development of the lead placement score (LPS). Overall, these results demonstrate that 4DCT imaging, combined with the novel methods we have developed, is a remarkably promising candidate for transforming clinical cardiac imaging, especially for patients undergoing transcatheter-based procedures.

Chapter 1: Introduction to minimally invasive transcatheter cardiac interventions and noninvasive imaging

1.1 The growth of percutaneous interventions and the need for noninvasive imaging

Although heart disease remains the leading cause of death in the United States, the mortality rate has dropped by more than 60% in the last 75 years [1], [2]. These lower death rates are accompanied by a growing number of adults over the age of 65, which is projected to account for 22% of the population by 2040 [3]. While this is a significant achievement for both science and medicine, it is well documented that a predominant risk factor for cardiovascular disease is age [4]. As life expectancy increases, the prevalence of heart failure and valvular heart diseases, such as aortic stenosis and mitral regurgitation, is on the rise [5]–[7]. In fact, aging and population growth in the last 30 years has led to a 112% increase in the number of deaths attributed to nonrheumatic valve disease [8]. In addition, heart failure is now the most common diagnosis in hospitalized adults over the age of 65 [7].

For heart failure patients with reduced left ventricular (LV) ejection fraction (EF) and New York Heart Association (NYHA) class I-IV, the Class I recommendation for treatment after initial diagnosis is to start guideline-directed management and therapy of beta blockers and diuretics as needed [9]. However, approximately 50% of these patients will be readmitted to the hospital at least once within a year after diagnosis (80% after 5 years) [7]. While studies have shown that medication use falls short of the target doses from landmark clinical trials, many of these patients are also hospitalized for reasons other than heart failure [7], [10]. This is evidence of the high comorbidity burden in this group. For patients with moderate to severe valvular disease, medical therapies are primarily for symptom control and repair or replacement of the valve is the treatment of choice [5]. However, these patients also present significant challenges for clinical care due to the presence of multiple comorbidities leading to higher surgical risk for many procedures [4],

[11]. The need for better treatment options for high risk heart failure and valvular disease patients sparked the development of minimally-invasive percutaneous interventions [11]–[15].

1.2 Transcatheter heart valve replacement

1.2.1 Transcatheter aortic valve replacement

Recently, transcatheter aortic valve replacement (TAVR) has emerged as the standard of care treatment for patients with severe aortic valve stenosis with intermediate to high surgical risk [5], [16]. As success rates improve in higher-risk populations, younger, lower-risk patients are more likely to become eligible for these catheter-based interventions as demonstrated by the PARTNER 3 clinical trials [17], [18]. However, long-term follow-up of transcatheter valve durability and left ventricular (LV) remodeling is currently unknown for these devices [18]. Noninvasive imaging can play a critical role in defining *in vivo* standardized metrics of LV remodeling and structural valve deterioration based on image-derived criteria [19]. Once these are well-defined and understood, noninvasive imaging can potentially be used to predict long-term response to valve implantation and device failure.

The timing of TAVR in lower-risk patients also needs to be assessed. If the procedure is performed too early, the procedural risk would outweigh the low annual risk of cardiovascular death [18]. However, if it is performed too late, irreversible myocardial damage may have already occurred [20]. Therefore, image-derived criteria can also be used for patient stratification and clinical planning of TAVR [21]. In addition, these roles of noninvasive imaging for TAVR can also be extended to future transcatheter procedures. The rapid growth, development, and success of TAVR demonstrated that transcatheter therapies may offer benefits over surgical valve replacement, especially in high risk patients [22]. These benefits include avoiding cardiopulmonary bypass, rapid ventricular pacing, or sternotomy and shorter hospital recovery times [23].

1.2.2 Transcatheter mitral valve implantation

Mitral regurgitation (MR) is the leakage of blood back into the left atrium (LA) as the LV contracts. There are two types of MR: 1) Primary, or degenerative, MR affecting the leaflets of the valve and caused by degenerative disease, rheumatic disease, connective tissue disorders, and infective endocarditis, and 2) secondary, or functional, MR affecting the LV and LA caused by ischemic and nonischemic cardiomyopathies [22]. Both types of MR can cause increased blood volume and increased pressure in the LV, LA, and pulmonary veins [22]. This forces the heart to work harder to pump blood forward through the aorta leading to progressive LV dilation, dysfunction, and heart failure with substantial morbidity and mortality if left untreated [24]. Because of this, several transcatheter mitral valve implantation (TMVI) therapies are currently being developed with promising early results [22], [25], [26].

Due to the complex structure and function of the mitral valve, TMVI, even more so than TAVR, also heavily relies on pre- and periprocedural noninvasive imaging [25], [27] . For example, the mitral valve has a relatively large annulus which is noncircular, lies close to the LV outflow tract, and is subject to high cyclic LV systolic pressures [24], [28]. Therefore, advanced noninvasive imaging techniques are already being used to determine patient suitability during anatomical screening and device sizing, characterize the landing zone and delivery access points, and identify patients at risk for LV outflow tract obstruction [12], [25], [29]. We hypothesize that noninvasive imaging also has the potential to help determine which patients will benefit from valve repair or replacement procedures based on quantifiable prognostic parameters.

Typically, LVEF is a parameter used to quantify cardiac function as well as eligibility and fitness for certain procedures. According to the AHA/ACC guidelines for valvular heart disease, surgery is a Class I indication for patients with severe primary MR and LVEF >30%; in contrast there is only a Class IIb indication for surgery in those with LVEF <30% [30]. However, when MR is present, EF may not adequately represent LV systolic function because a significant proportion

of the stroke volume flows retrograde into the left atrium [31], and it has been shown that EF is a late indicator of LV dysfunction [32], [33]. As an alternative, recent studies have demonstrated that myocardial deformation parameters, such as global longitudinal and circumferential strain, are more sensitive measures and can be utilized to detect disease earlier than significant changes in EF [34], [35]. Yet, many patients with secondary MR tend to also have dyssynchronous function and highly regional abnormalities; hence, these global metrics cannot accurately capture the full picture of LV function [35]. High resolution regional measurements of myocardial function could provide a better characterization of the extent of LV dysfunction in patients with MR. We hypothesize that this more personalized approach to determining a functional threshold for mitral valve replacement could lead to better patient selection and clinical outcomes.

1.2.3 Tendyne mitral valve replacement system

To date, the Tendyne TMVI device (Tendyne Holdings, LLC, Roseville, Minnesota – a subsidiary of Abbott Vascular, Santa Clara, CA) is the only one of its kind with “Conformité Europoéenne” (CE) mark [23]. As shown in Figure 1, the device has a self-expanding nitinol double-frame, trileaflet porcine valve in the inner frame, D-shaped outer frame to conform to anatomic shape of the annulus, anterior cuff to aid in valve sealing, and a tether to stabilize the device which is anchored to the epicardial surface through the apex with the epicardial pad [23], [24]. The Tendyne device is fully repositionable and retrievable [23]. A study which examined the first 100 patients to receive the device showed that it reached safety standards and was highly effective in relieving MR and improving symptoms [26]. The cohort consisted of subjects with either primary or secondary MR that were 75.4 ± 8.1 years old with a high prevalence of severe, symptomatic heart failure (66%), LV dysfunction (EF 46.4 ± 9.6%), and comorbidities (Society of Thoracic Surgeons Predicted Risk of Mortality Score 7.8 ± 5.7%) [26].

While these initial results are promising, larger studies will be conducted to assess longer-term outcomes with the Tendyne device. These results should also be compared to other

therapeutic options for patients with symptomatic MR who are at high surgical risk, such as transcatheter mitral valve repair [26]. As discussed previously, noninvasive imaging will play a critical role in the long-term follow-up of these patients. Therefore, noninvasive imaging has the potential to improve clinical planning, allow for a better understanding of the effects of MR and TMVI on cardiac function and remodeling, and identify prognostic parameters which can be used to predict response to the procedure [36], [37].

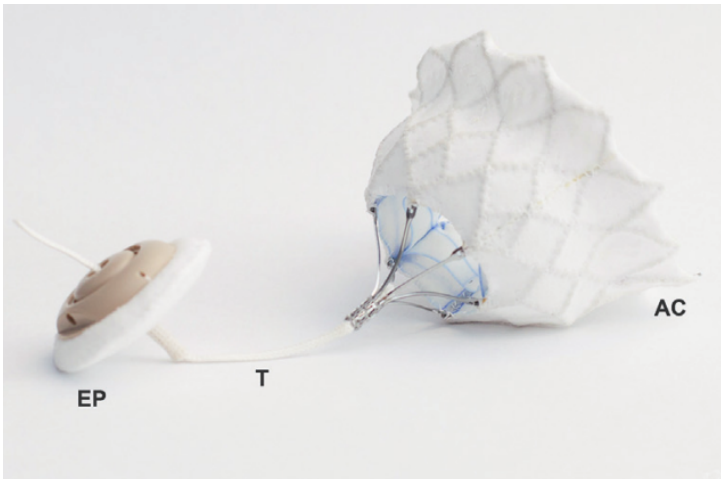

Figure 1. The Tendyne TMVI device with the epicardial pad (EP), tether (T), and anterior cuff (AC) which is delivered transapically. The tether and epicardial pad stabilize the device while the anterior cuff aids in valve sealing. The device is fully repositionable, fully retrievable, and self-expanding and is the only one of its kind to receive a CE mark. Image reproduced from the Tendyne Global Feasibility Trial study [24].

1.3 Cardiac Resynchronization Therapy

A percutaneous intervention called cardiac resynchronization therapy (CRT) emerged as a promising therapy in the 1990s for a subset of heart failure patients [14]. Since then, CRT has been one of the most successful therapies developed for heart failure patients in the last 30 years [14], [38]. Now, CRT is a class I recommendation for patients with NYHA class II-IV, LVEF less than 35%, and abnormal electrical activation, as indicated by a wide QRS complex on an electrocardiogram (ECG) [9]. Previous trials have shown that in this group, which accounts for approximately 25% of all heart failure patients, CRT reduced the rate of death and hospitalization, reduced symptoms, improved quality of life, and can lead to reverse LV remodeling and improved

EF [14], [39], [40]. Despite these promising results, approximately 30% to 50% of patients do not respond to the treatment depending on the definition used to classify response to CRT [14], [41]–[45]. Therefore, decreasing the non-responder rate to CRT remains an unmet clinical need, especially given the relatively high cost of the procedure and potential complications related to non-response leading to increased risk of hospitalization or death [15], [46]. Studying and quantifying the mechanisms of LV dyssynchrony in order to understand why patients do not respond to CRT has been an active area of research for over three decades, but the role of imaging is still unclear [47]–[49].

1.3.1 Left ventricular lead placement and response to CRT

CRT involves LV and right ventricular (RV) electrical stimulation with a pacemaker or implantable cardioverter-defibrillator (ICD) with the capacity for simultaneous biventricular pacing [14]. Recent studies have shown that placing the LV lead in myocardial scar or outside of mechanically late-activated regions may result in suboptimal response [44], [45], [50]. Mechanical dyssynchrony of LV activation has been somewhat successfully characterized using cine magnetic resonance imaging (CMR), CMR tagging, cine DENSE, and more recently, cardiac computed tomography (CT) and speckle tracking echocardiography (echo) [41], [43], [45], [51]–[56]. Because this is a complex field, and various approaches have been attempted, the most recent studies using CT, echo, and MRI for image-guided LV lead placement for improving response to CRT are summarized in Table 1.

Using CT imaging, Truong *et al*. found that their CT dyssynchrony metrics were associated with 2-year major adverse cardiac events (MACE) but not with 6-month CRT response. Their dyssynchrony parameters were measured form endocardial and epicardial contours and quantified time to maximum wall thickness and inward wall motion. Using first-pass CT perfusion, they also quantified myocardial scar burden and found that a lead concordant to regionals of maximal wall thickness was associated with less MACE [57]. Fyenbo *et al.* also used CT to identify

myocardial scar from regions of hypoperfusion and found that a higher scar burden and proximity of the scar to the LV pacing site was associated with echo non-response but not clinical response [50]. Lastly, in a recent prospective study with 18 subjects, Gould *et al.* found that dP/dt_{max} was superior in the target versus non-target segment based on maximum time to peak contraction (measured by endocardial contours) and freedom from myocardial scar (measured from late iodine enhancement imaging from CT) [45].

Using CMR cine DENSE and late gadolinium enhancement (LGE) imaging, Bilchick *et al*. found that mechanical, electrical, and scar properties at the lead placement were strongly associated with CRT response and clinical events, such as death, hospitalization for heart failure, implantation of a left ventricular assist device (LVAD), or appropriate ICD therapies [58]. When CMR DENSE strain imaging was combined with the Seattle Heart Failure Model, they were able to stratify patients effectively for CRT based on their risk score [59]. Lastly, Auger *et al*. also used CMR DENSE imaging to show that the time to onset of shortening (TOS) correlated better with electrical activation compared to time to peak strain (TPS) and, in their cohort, TOS was a predictor of LV reverse remodeling whereas TPS was not [59].

Using echo, Chung *et al.* measured 12 conventional and tissue doppler-based parameters of dyssynchrony in large multi-center trial and found high variability in the estimates and poor correlation with clinical outcomes. Because of these results, no single echo measure of dyssynchrony in this study was recommended to improve patient selection for CRT beyond the current guidelines [60]. Borquist *et al*. also found that using speckle-tracking echocardiography to measure the time to peak radial strain and CMR LGE to quantify scar, imaging-guided lead placement did not result in increased echo or clinical response [49]. In contrast, Khan *et al.* and Aalen *et al*. found that echo-guided lead placement might increase CRT response using time to peak radial strain, metrics of septal and lateral myocardial work, and myocardial viability from CMR LGE [41], [61].

Table 1. Recent studies that used image-guided LV lead placement to try and improve response to CRT. Studies are summarized for CT, MRI, and echo-based methods.

Modality	Study	Year	N	NYHA Class > II (%)	LBBB (%)	Chronic RV pacing (%)	Definition of Response to CRT	Non-response rate (%)	Predictors
CT	Gould *et al.* [45]	2021	18	39	74	9	≥15% decrease in 2D echo-derived LVESV at 6-months;	28	Time to peak contraction (from endo. contours) used to identify latest mechanically activated AHA segment for lead placement, late iodine enhancement for CT scar imaging
	Fyenbo *et al.* (Subset of ImagingCRT study) [50]	2019	140	51	N/A	14	Echo Response: >5% increase in 2D echo-derive ED; Clinical response: as improvement in New York Heart Association (NYHA) class and 10% increase in the 6 min walk test, or freedom from hospitalization for heart failure or death at 6-months	Echo: 22; Clinical: 31	Myocardial scar (from regions of hypoperfusion in CT)
	Truong *et al.,* (DIRECT study) [57]	2018	54	83	83	60	Clinical composite score (CCS) based on 6-month death, hospitalization, discontinuation of CRT, improvement in NYHA class	40	Time to maximum wall thickness and inward wall motion (from endo. and epi. contours), myocardial scar imaging using first-pass CT perfusion

Table 1. Recent studies that used image-guided LV lead placement to try and improve response to CRT. Studies are summarized for CT, MRI, and echo-based methods (continued).

Modality	Study	Year	N	NYHA Class > II (%)	LBBB (%)	Chronic RV pacing (%)	Definition of Response to CRT	Non-response rate (%)	Predictors
MRI	Bilchick *et al.* [59]	2020	100	91	65	N/A	Echo: ≥15% decrease in 2D echo-derived LVESV at 6-months Clinical: freedom form death, heart transplant, LVAD, or appropriate ICD therapies	Echo: 45; Clinical: 53	CURE-SVD measured from CMR cine DENSE, Seattle Heart Failure Model (SHFM-D) *
	Auger *et al.* [43]	2017	6 healthy volunteers; 50 heart failure patients	82	64	N/A	≥15% decrease in 2D echo-derived LVESV at 6-months	N/A	From CMR cine DENSE: time to onset and time to peak E_{cc}, QRS to LV intrinsic activation interval (QLV), absence of scar at lead (from late Gd enhancement)
	Bilchick *et al.* [58]	2014	75	96	89	N/A	≥15% decrease in 2D echo-derived LVESV at 6-months	47	From CMR cine DENSE: CURE, time to onset of E_{cc} at lead, absence of scar at lead (from late Gd enhancement), QRS to LV intrinsic activation interval (QLV)

Table 1. Recent studies that used image-guided LV lead placement to try and improve response to CRT. Studies are summarized for CT, MRI, and echo-based methods (continued).

Modality	Study	Year	N	NYHA Class > II (%)	LBBB (%)	Chronic RV pacing (%)	Definition of Response to CRT	Non-response rate (%)	Predictors
Echo	Borgquist *et al.* [49]	2020	102	75	74	10	≥15% decrease in 2D echo-derived LVESV at 6-months	44	In imaging guided group: LV lead placed at site of latest contraction with amplitude > 9.5% to signify freedom from scar as measured by echo speckle-tracking 2D radial strain imaging + Late Gd enhanced MRI to identify scar
	Aalen *et al.* [41]	2020	200	N/A	86	13	≥15% decrease in 2D echo-derived LVESV indexed to body surface area at 6-months	42	Myocardial work measure by pressure-strain (longitudinal strain by speckle-tacking echo) analysis and viability by CMR Late Gd Enhancement (125/200 patients)
	Khan *et al.*, (TARGET study) [62]	2012	220	100	N/A	N/A	Echo response of ≥15% decrease in 2D echo-derived LVESV at 6-months and clinical response defined as improvement in NYHA class, all-cause mortality, and combined all-cause mortality and heart failure-related hospitalization	Echo: 30; Clinical: 17	In imaging guided group: LV lead was placed at the site of latest contraction with amplitude > 10% to signify freedom from scar as measured by echo speckle-tracking 2D radial strain imaging

Table 1. Recent studies that used image-guided LV lead placement to try and improve response to CRT. Studies are summarized for CT, MRI, and echo-based methods (continued).

Modality	Study	Year	N	NYHA Class > II (%)	LBBB (%)	Chronic RV pacing (%)	Definition of Response to CRT	Non-response rate (%)	Predictors
Echo	Chung *et al.,* (PROSPECT trial) [60]	2008	498	100	N/A	N/A	Improved Clinical Composite Score (CCS) and ≥15% decrease in 2D echo-derived LVESV at 6-months; CCS was composed of death, hospitalization, discontinuation of CRT, improvement in NYHA class	CCS: 31; LVESV: 44	12 Conventional and tissue doppler-based parameters of dyssynchrony

*SHFM-D score (typical range -2 to 2) was determined based on the following covariates: ischemic etiology of cardiomyopathy, age, weight, systolic blood pressure, LV ejection fraction, New York Heart Association functional class, digoxin use, use of an angiotensin-converting enzyme inhibitor or angiotensin receptor blocker, use of beta-blockers, use of statins, daily doses of loop diuretics, serum sodium, serum creatinine, and serum hemoglobin

1.3.2 Current unmet needs in image-guided LV lead placement for CRT

The imaging techniques shown in Table 1 have been utilized to calculate metrics such as peak LV strain, time to peak strain, time to onset of shortening (TOS), and the circumferential uniformity ratio estimate (CURE) index in order to fully characterize LV function and dyssynchrony and locate regions of late-activated myocardium [41], [43]–[45], [51], [56], [58]. TOS, a parameter which highlights late-activated segments of the LV, has been shown to be more strongly correlated with LV reverse remodeling 6-months post CRT compared to time to peak strain [43]. CURE is a global parameter describing the dyssynchrony of the LV that ranges from 0 to 1, where 1 indicates perfectly synchronous contraction, and 0 represents complete anti-phase contraction of one side of the LV to the other [44]. CURE has also been shown to be strongly associated with LV reverse remodeling post CRT [58]. In addition, myocardial scar has also been identified using late gadolinium enhancement with MRI in patients without existing pacing devices [63]. However, 28% of patients eligible for CRT already have a RV pacing or ICD system in place, which may be unsuitable for MR because of significant image degradation due to metal artifacts or if the devices are not MRI-compatible. [45].

While some of the studies summarized in Table 1 for quantifying imaging-derived parameters have shown prognostic value for improving response to CRT, poor reproducibility of initial echo-based methods, contraindications for MRI scan protocols, lack of trained technicians in image acquisition and analysis, and the absence of open source or commercial availability of MRI DENSE software has hindered the clinical utility and implementation of the proposed methods [45], [64], and no imaging method is currently recommended for CRT planning. This indicates the need for a widely available imaging modality and highly reproducible method for guiding CRT in order to continue the quest of increasing the response rate in selected patients.

1.4 Technological developments in noninvasive imaging

The increased complexity of percutaneous procedures demanded, and continues to do so, new imaging techniques to assist these interventions. Standard catheterization laboratory modalities, such as fluoroscopy, were crucial for guidance during the development of new procedures. However, fluoroscopy lacks adequate soft-tissue contrast and does not easily allow for visualization of 3D structures for precise planning [65]. Advances in noninvasive imaging have supported the growth and maturation of interventional cardiology by addressing these limitations [11], [16]. Modalities such as echo, MRI, and CT were crucial in initial preprocedural planning and device selection because they could provide information on the exact location, size, and severity of cardiac pathologies and surrounding anatomy for determining catheter access points [12], [16], [65], [66]. More recently, noninvasive imaging has expanded its applicability and there is active research testing the use of physiological function in addition to anatomy in order to predict how a patient will respond to specific treatments. With technological advancements for both the procedures and the imaging modalities, clinical outcomes have improved significantly [21].

1.5 Current methods for quantification of left ventricular function using noninvasive imaging

As mentioned previously, current selection criteria for many cardiac procedures are often based on prognostic parameters linked to LV function [32]. LV EF defined as the stroke volume divided by end-diastolic volume, is a global measure of systolic function and has been correlated with mortality in patients with heart failure [67]–[70]. Yet, a significant reduction in EF is a late consequence of disease and may result in irreversible myocardial dysfunction [32], [33], [71]. In addition, when MR is present, EF may not adequately represent the true inotropic status because blood moves backwards into the left atrium [35]. Myocardial deformation parameters, such as global longitudinal strain (GLS), global circumferential strain (GCS), and LV twist, have proven to be superior to EF as a measure of function and a predictor of mortality and cardiac events [32]–[35], [67], [72]–[76]. They are more direct measurements of myocardial contractility and therefore

less dependent on LV geometry and loading conditions compared to EF [74], [75]. However, in patients with highly regional dysfunction, or myocardial dyssynchrony, these global metrics cannot accurately capture the full picture of LV function [35]. This indicates the need for more sensitive and regional measurements of cardiac function to understand the extent of LV dysfunction in patients with complex cardiac dysfunction.

1.5.1 Echocardiography

2D Speckle-tracking echocardiography has been proposed for measuring regional strain because of its high temporal resolution, however, both the image acquisition and analysis process are subject to operator variability. During acquisition, the operator prospectively chooses the imaging plane based on the available acoustic window. Foreshortening in the long axis, tilting of the beam in the short axis, and through-plane motion can lead to errors in measurements [32]. The analysis requires the user to draw epicardial and endocardial contours to define the myocardium in the 2D slice and the segmental strain varies depending on which wall layers are incorporated by the user [32]. This leads to highly non-reproducible results when “blind” analysis is performed by the operator.

1.5.2 Cardiac magnetic resonance imaging

Although MRI tagging is considered the gold standard for highly accurate and reproducible myocardial deformation, there are contraindications for some patients with implanted devices. In addition, the requirement for multiple identical heartbeats, long scan times, and several breath holds is not ideal for patients with irregular cardiac rhythms or very sick patients [77]. Lastly, image analysis is not trivial and necessitates manual segmentation or correction of contours which are subject to variability [78]. For these reasons, MRI tagging has only seen use in research settings.

1.6 4D x-ray computed tomography

Although some studies have begun to demonstrate the prognostic value of regional measures of LV function, the ability to quantify and leverage these metrics in the clinic has thus

far been limited, primarily due to 2D imaging, inter- and intra-operator variability, dependence on operator experience, and scan protocols with contraindications for unhealthy patients as discussed above [79]. We propose to address the limitations of these modalities by using 4DCT to conduct regional analysis of myocardial function. 4DCT allows for full 3D volumes to be acquired across the entire cardiac cycle within a single heartbeat. In addition, 4DCT provides very high spatial resolution images (typically, voxel sizes of 0.5 x 0.5 x 0.6 mm) which allow for visualization of submillimeter features on the endocardial surface with the use of a contrast bolus. These intricate features can serve as fiducial markers which support motion tracking. Studies have shown that differential geometry features of the myocardial surfaces can be used to estimate deformation fields from 3D anatomic images [80], [81]. Lastly, CT is already used for planning many transcatheter interventions and evaluation of coronary anatomy and therefore scanning protocols can easily be adapted to include functional analysis [16], [24], [27] with a very small additional radiation dose [82].

1.6.1 Recent technological advancements for 4DCT

The advantages mentioned above make 4DCT a remarkably promising candidate for transforming clinical cardiac imaging. We hypothesize that single heartbeat 4DCT volumes can be used to acquire precise noninvasive measurements of regional endocardial cardiac function to quantify myocardial dysfunction. Although there is a concern regarding patient radiation dose in CT, with recent technological developments such as dose reduction protocols, iterative reconstruction methods, and wide-range detectors, the average dose for a full functional cardiac scan has decreased significantly in the past 5 years and images of diagnostic quality can be obtained with submillisievert radiation dose [83].

1.6.2 CT regional endocardial shortening

Taking advantage of these technological developments, Dr. Elliot McVeigh and his lab pioneered the technique of using contrast-enhanced 4DCT images to measure contour-free

endocardial deformation. They defined a parameter called CT SQUEEZ, or stretch quantifier of endocardial engraved zones, which quantifies the change in area of a triangular mesh face on the endocardial surface over time and has no directional sensitivity [78]. CT SQUEEZ can be measured in a single heartbeat and measures regional deformation in 3D, thereby eliminating through-plane artifacts traditionally seen with 2D imaging [78]. This parameter was shown to distinguish normal from infarcted regions in porcine hearts *in vivo* [78], validated against MR tagging in canines [84], and produced highly reproducible measurements in a cohort of 25 humans with normal LV function from standard clinical coronary CTA exams [77]. To more closely resemble traditional strain, CT regional endocardial shortening, or RS_{CT}, was defined as SQUEEZ-1 so that a negative value represented tissue which was contracting, and a positive value represented tissue which was stretching. Lastly, CT SQUEEZ laid the technological foundations for further development of novel methods for measuring LV function using 4DCT. These methods are introduced and validated in Chapters 4-7.

1.7 Thesis Outline

This thesis is broken into 7 subsequent chapters.

The second chapter introduces and evaluates the feasibility of a comprehensive method for quantifying baseline values and changes in high-resolution RS_{CT} in patients before and 1-month after TMVI using contrast-enhanced 4DCT. As TMVI is a relatively new procedure, this is the first study to quantify regional effects of mitral regurgitation on LV function and the subsequent changes after device implantation. We also evaluate the reproducibility of RS_{CT} in a subset of these patients with highly abnormal LV geometries and function.

The third chapter describes the development of the lead placement score (LPS) which could be used to improve 4DCT-guided CRT. In this chapter, we use 5-fold cross-validated linear discriminant analysis (LDA) to create the LPS and evaluate the prognostic value of 4DCT-derived metrics of LV shape, global and regional function, and dyssynchrony, such as LV end-diastolic

volume (EDV), LV end-systolic volume (ESV), $CURE_{tot}$, $CURE_{sys}$, TOS, RS_{CT}, endocardial end-diastolic sphericity (Sph_{ED}), and endocardial end-systolic sphericity (Sph_{ES}).

The fourth chapter introduces and describes in detail the novel algorithms for measuring endocardial LV rotation, torsion, and regional longitudinal and circumferential strain from 4DCT data. These novel methods were built on the technological foundations laid by the previously-validated CT SQUEEZ method, but they improve the analysis by computing endocardial strains in local "patches" of point clouds representing the endocardial surface, improving sensitivity to mesh quality and introducing directional strain.

The fifth chapter describes the validation of the novel methods proposed in chapter 4 with phantom experiments. The accuracy of 4DCT-derived endocardial LV rotation, torsion, regional longitudinal strain, and regional circumferential strain are quantified for different standard clinical scanning conditions using a 3D-printed anthropomorphic LV endocardial phantom. The precision of these metrics is also evaluated in 10 independent analyses at the lower limits of image quality (very low dose scanning) achieved using standard clinical reconstruction protocols.

The sixth chapter demonstrates that 4DCT-derived regional strain can be evaluated using standard clinical images in human subjects and compares these estimates to CMR tagging-derived regional strain. Normal values of 4DCT-derived regional longitudinal, $\mathrm{E}_{ll}^{\mathrm{CT}}$, and circumferential, $\mathrm{E}_{cc}^{\mathrm{CT}}$, strain are derived in a cohort of subjects with normal LV function. This normal set of values was also used to identify abnormal segments in two subjects with previous MI with high precision.

The seventh chapter demonstrates that 4DCT-derived rotation and torsion can also be evaluated using standard clinical images in human subjects. This chapter describes the results of the first known study to perform a direct comparison between 4DCT and 2D CMR tagging-derived endocardial LV rotation and torsion in human subjects. Normal values of 4DCT-derived rotation

and torsion and the reproducibility of these metrics are measured in subjects with normal LV function.

The final chapter provides a summary of the results of this dissertation and discusses the broader implications for the field of cardiovascular imaging and interventional cardiology. This chapter also suggests future studies and opportunities for 4DCT-derived metrics of cardiac function.

1.8 Acknowledgements

Chapter 1, in part, has currently been submitted for publication of the material, Gabrielle M. Colvert, Ashish Manohar, Francisco J. Contijoch, James Yang, Jeremy Glynn, Philipp Blanke, Jonathon A. Leipsic, Elliot R. McVeigh. “Novel 4DCT method to measure regional left ventricular endocardial shortening before and after transcatheter mitral valve implantation.” The dissertation author was a primary author of this paper.

Chapter 1, in part, is currently being prepared for submission for publication of the material, Gabrielle M. Colvert, Ashish Manohar, Brendan T. Colvert, Zhennong Chen, Chansu Kim, James Yang, Andrew Schluchter, Maria Ledesma-Carbayo, Anders S. Knudsen, Jens C. Nielsen, Elliot R. McVeigh. “Predicting 6-month post CRT outcomes using 4DCT-derived metrics of left ventricular shape, function, and dyssynchrony.” The dissertation author was a primary author of this paper.

Chapter 2: Analysis of regional and global left ventricular function using 4DCT before and after transcatheter mitral valve implantation

2.1 Introduction

In addition to improvements in bioprosthetic devices and surgical technologies, advances in noninvasive imaging have supported the outcomes of transcatheter procedures [11], [16]. Their role has expanded from anatomical pre-procedural planning to include analysis of cardiac physiology for diagnosis, periprocedural guidance, and post-procedural follow-up [16], [24], [25]. We hypothesize that noninvasive imaging also has the potential to help determine which patients will benefit from valve repair or replacement procedures based on quantifiable prognostic parameters [12], [25], [29].

Transcatheter mitral valve implantation (TMVI) is a relatively new procedure for treating MR; however, its effect on regional LV function has yet to be characterized. 4D x-ray computed tomography (4DCT) is a promising method for evaluating changes in regional cardiac function in patients with abnormal LV geometry and local dysfunction because of its high 3D spatial resolution and full heart volume coverage within a single heartbeat [29], [83]. The goal of this chapter was to investigate the feasibility and reproducibility of evaluating 4DCT-derived regional endocardial shortening (RS_{CT}) in patients receiving TMVI. Local areas of hypokinesis and LV dysfunction are frequent in this population and therefore represent a particularly relevant cohort to study regional LV function. RS_{CT} was previously shown to correlate well with MRI-tagging derived myocardial strain and therefore serves as a surrogate of strain in this work [84]. Due to the small cohort of patients, we did not attempt to evaluate factors that correlated with patient outcomes. To the best of our knowledge, this is the first study to use 4DCT to quantify 3D regional LV function in subjects before and after TMVI.

2.2 Materials and Methods

2.2.1 Subjects

All subjects included in the present analysis were enrolled in the Expanded Clinical Study of the Tendyne Mitral Valve System (NCT02321514) between November 2014 and November 2017 across 24 hospitals. Institutional Review Board approval and informed patient consent was obtained at each of the individual sites. Twenty-four patients treated with TMVI due to significant MR (grade 3 or 4) and deemed unsuitable for conventional mitral valve surgery were considered for analysis. Seventeen subjects had 4DCT exams before and 1-month after TMVI with at least end-diastolic (ED) and end-systolic (ES) phases and were therefore included in this preliminary proof-of-concept study. Table 2 lists the reasons that 7 patients were not analyzed. The CT exams were conducted at 8 different study sites as part of Tendyne's Global feasibility study as previously described [26]. Ten subjects had retrospective imaging with full R-R cycles which were analyzable at baseline and 1-month, and 7 subjects had at least ED and ES included in the phases imaged. The subjects were scanned on a single-beat Toshiba Aquilion ONE, multi-beat Siemens SOMATOM Definition, multi-beat Siemens SOMATOM Force, or a multi-beat Philips iCT 256. The minimum and maximum pixel spacing was 0.344 mm and 1.145 mm, respectively. Lastly, the minimum and maximum slice thickness was 0.5 mm and 1.5 mm, respectively. LV volumes were computed from the 4DCT scans by counting the number of voxels identified as blood pool in the LV segmentation from the tip of the endocardial apex to the mitral valve plane. These volumes excluded the papillary muscles and were used to calculate LV ejection fraction (EF).

Table 2. Reason images were not analyzed for comparison of 4DCT-derived regional endocardial shortening before and 1-month after TMVI.

Reason for images not analyzed	Number of patients excluded
Irregular Heartbeat (Double beat leading to incomplete ejection of blood)	2
Step Artifact	4
Low contrast between LV blood pool and myocardium (poor contrast injection timing)	1
Total	7/24

2.2.2 Analysis of 4DCT-derived regional endocardial shortening

The LV blood pool was segmented from the 4DCT images in 3D using a region-growing algorithm in ITK-SNAP (ver. 3.6.2) [85] in order to extract the endocardial surface for the analysis. The threshold for segmenting the LV blood pool was determined mathematically using Otsu's method on a region-of-interest in a mid-axial slice at ED containing the contrast-enhanced blood pool and the surrounding myocardium [86]. We obtained a surface representation of the endocardium to include the full LV from the endocardial apical tip to the mitral valve plane [87]. In 3D, two planes were defined manually to separate the left atrium and the LV outflow tract (LVOT) from the LV. The mitral valve plane was cut at the mitral annulus using the posterior segment of the D-shaped annulus as a landmark as this region of the annulus is most planar [28], [88]. The plane defining the aortic outflow tract was cut tangent to the surface of the LV blood pool and intersected the left and right trigone where the mitral annulus meets the LVOT [28]. This LV blood pool segmentation was repeated in all timeframes available from the 4DCT. Triangular meshes of the endocardial boundary were extracted from the 3D segmentation using *isosurface* in MATLAB and point-cloud registration [89] was performed on these surfaces in order to obtain 3D displacement fields across the cardiac cycle as previously described [77], [78]. Figure 2 summarizes the process of obtaining these displacement fields from the 4DCT data. After point-cloud registration, RS_{CT} was defined as

$$RS_{CT} = \sqrt{\frac{Area(t,x)}{Area(ED,x)}} - 1 \tag{2.1}$$

where the area is calculated for face, x, at time, t, and the reference timeframe of ED (Figure 3). A negative RS_{CT} value indicates that the endocardial surface in that region is contracting while a positive RS_{CT} value indicates that the surface is stretching.

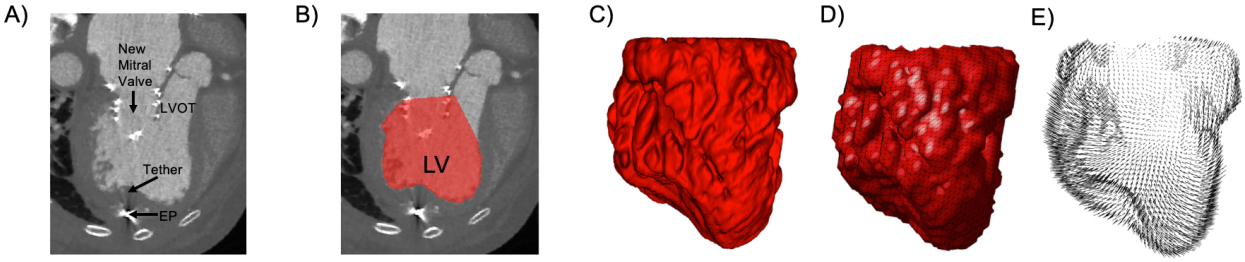

Figure 2. A) Contrast-enhanced 4DCT image containing the left ventricle (LV), LV outflow tract (LVOT), and the TMVI device including the tether and epicardial pad (EP), B) Segmentation of LV blood pool is performed using a region growing algorithm. The threshold for segmentation is determined using Otsu's method, C) 3D view of segmented LV blood pool, D) Endocardial surface extracted from the segmentation in MATLAB, E) Point-cloud registration is used to solve for the 3D displacement field of the endocardial surface between timeframes.

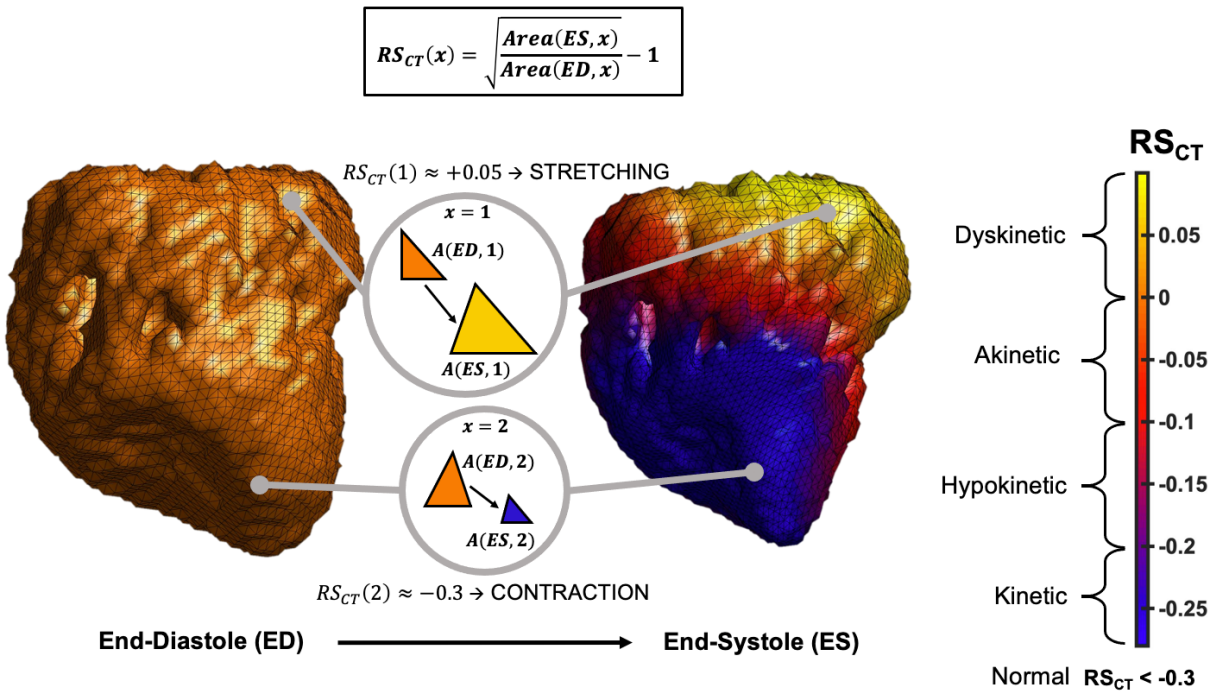

Figure 3. RS_{CT} is defined by the equation shown and was characterized as normal ($RS_{CT} \leq -0.3$), kinetic ($-0.3 < RS_{CT} \leq -0.2$), hypokinetic ($-0.2 < RS_{CT} \leq -0.1$), akinetic ($-0.1 < RS_{CT} \leq 0$), and dyskinetic ($RS_{CT} > 0$) before and 1-month after TMVI.

2.2.3 Characterization of changes in RS_{CT} between baseline and 1-month after TMVI

High resolution maps of RS_{CT} were measured (90 LV segments, 5 longitudinal x 18 circumferential) to capture the highly variable changes in geometry and function of these patients with severe MR, frequent LV dyssynchrony, and local myocardial deformation from the epicardial pad. For subjects with images spanning the entire R-R cycle, peak RS_{CT} was defined as the minimum point on the RS_{CT} vs. time curves for each segment within a window of ±25% of the time of minimum LV volume. For subjects with images over a partial interval of the R-R cycle, peak RS_{CT} was defined at the time of minimum LV volume. Bullseye plots were constructed to compare peak RS_{CT} in all 90 segments pre and post TMVI. As the specific anchoring system of the Tendyne TMVI device uses a tether and epicardial pad, abnormal local deformation of the LV was expected in the region near the pad. Therefore, the epicardial pad was identified on the CT images and its location was marked on the bullseye plots (Figure 4).

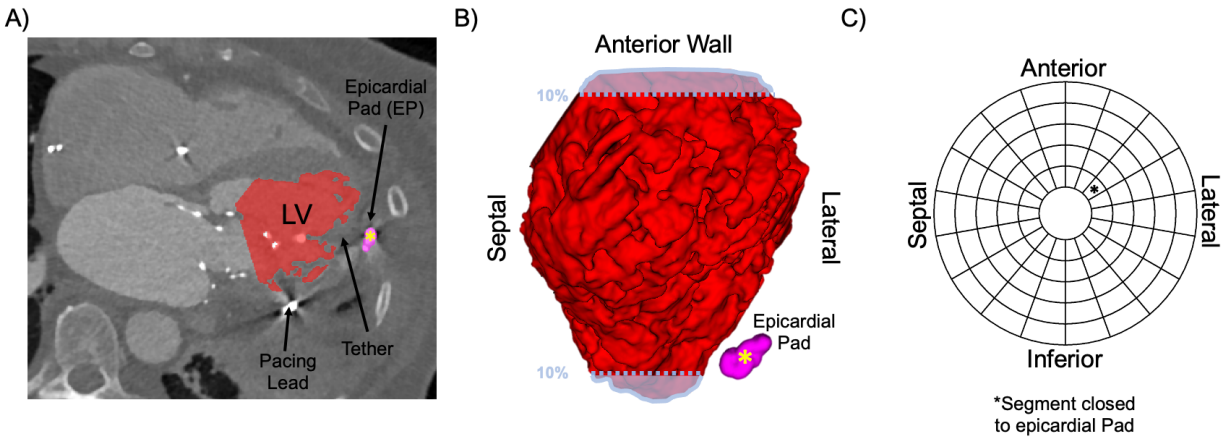

Figure 4. A) Axial view of segmented left ventricle (LV) and epicardial pad (EP), B) 3D view of segmented LV and EP. Only when creating the bullseye plots, the top and bottom 10 percent of the ventricle are excluded due to higher registration errors in these regions, C) Bullseye plot with 90 segments (18 circumferential x 5 longitudinal) marking the segment closest to the EP with an asterisk (*).

Normal peak RS_{CT} was measured from a cohort of 23 subjects with normal LV function and determined to be -0.32 ± 0.06 averaged over the entire LV. The characteristics of these subjects are shown in Table 3. Given the natural variation in RS_{CT} in these normal LVs, peak RS_{CT} in the TMVI patients in each segment was characterized as normal ($RS_{CT} \leq -0.3$), "kinetic" ($-0.3 < RS_{CT} \leq -0.2$), hypokinetic ($-0.2 < RS_{CT} \leq -0.1$), akinetic ($-0.1 < RS_{CT} \leq 0$), and dyskinetic ($RS_{CT} > 0$) as shown in Figure 3. The "kinetic" category between normal and hypokinetic was created in order to distinguish between the subjects who begin with somewhat normal function despite MR ("kinetic") and those with lower function at baseline (hypokinetic). Eighty-nine percent of Tendyne patients have secondary MR with advanced heart failure [26]; therefore, few patients have normal function, and the precision of RS_{CT} estimates [90] supported creating this additional "kinetic" functional category between normal and hypokinetic.

Table 3. Characteristics of subjects with normal LV function. *LVEF: left ventricular ejection fraction, **GLS: global longitudinal strain

N	23
Age, years	60 ± 12
Males (%)	12 (53%)
4DCT-derived LVEF*	70% ± 5%
4DCT-derived GLS**	21% ± 2%

2.2.4 Statistics

All statistical analyses were performed in MATLAB (2018b, MathWorks Inc.). To determine if changes in ED and ES volumes and EF were significant across the 17 subjects, paired, two-sided Wilcoxon signed rank tests were performed with a significance level of $\alpha = 0.05$. Segmental changes in RS_{CT} between pre and post TMVI were also evaluated for significance using paired, two-sided Wilcoxon signed rank tests with significance level of $\alpha = 0.05$. These paired differences were evaluated in each subject for all 90 segments. In addition, analysis on the apical region (two inner rings of the bullseye) was performed to attempt to isolate the effect of the epicardial pad. These statistical tests were used instead of the student t-test for two reasons: 1) the small cohort size and 2) RS_{CT} was not normally distributed (evaluated using the Kolmogorov-Smirnov Test for Normality) in many of the subjects due to their highly abnormal LV function. Correlation coefficients and corresponding p-values were also computed between global and regional metrics of LV function derived from 4DCT.

2.2.5 Reproducibility of RS_{CT} in TMVI patients

Because of the variability in image quality, the highly abnormal LV geometries of Tendyne patients, and the wide dynamic range of peak RS_{CT} within each subject, we evaluated the reproducibility of our method for measuring high-resolution regional endocardial function in a subset of this group of patients. In order to quantify intra-observer variability, the first observer (Observer 1) who performed the RS_{CT} analysis on all 17 subjects re-segmented the ED and ES

phases of the 5 patients with the largest decreases in EF post TMVI for both baseline and 1-month post TMVI 4DCT exams. Observer 1's second round of segmentations were performed at least 4 months after performing the original segmentation. These newly segmented timeframes were used to calculate RS_{CT} at ES and the 90 segment bullseye plots were compared with Observer 1's results from the first segmentation. Correlation and Bland-Altman plots were constructed to measure the variability.

For measurement of inter-observer variability, an Observer 2 was recruited to segment the same 5 patients at ED and ES for the pre and post TMVI exams. Observer 2's 90 segment bullseye plots were compared to Observer 1's two separate analyses. Again, correlation and Bland-Altman plots were created to show the variability. To quantify a single average limit of agreement from the Bland-Altman between the two comparisons, the propagation of error rules was followed. The mean bias was calculated as the average of the two biases and the mean standard deviation computed as:

$$dT = \frac{\sqrt{(d_{12})^2+(d_{22})^2}}{2} \tag{2.2}$$

where d_{12} is the standard deviation from Observer 1's first analysis and Observer 2 and d_{22} is the standard deviation from Observer 1's second analysis and Observer 2.

2.3 Results

2.3.1 Main Findings

The baseline characteristics of the 17 subjects evaluated in this study are shown in Table 4. Comprehensive analysis of the changes in global and regional cardiac function post TMVI using 4DCT was performed on all 17 subjects and is illustrated in Figure 5 for an example subject. Due to the heterogeneous pattern of RS_{CT} at baseline, and the subsequent complex change in RS_{CT} post TMVI, we created this visual report for each patient in order to perform comparisons between subjects. In this report, we show the changes in 4DCT-derived global LV function through changes

post TMVI in EDV, ESV, and EF (Figure 5A). High resolution maps of regional LV function at Baseline and 1-month post TMVI are shown side-by-side in 90 segment bullseye plots of peak RS_{CT} (Figure 5B); these maps show the original functional state of the LV, and the condition of the LV post TMVI. We enumerate the *changes* in RS_{CT} functional categories post TMVI in tabular form in Figure 5C; this summarizes the number of segments that increase contraction vs. decrease contraction post TMVI. These tabular results are also displayed in a bullseye plot to analyze the spatial patterns in these changes (Figure 5D). The “overall” changes in functional categories over the entire LV are captured in the histogram show in Figure 5E which gives the viewer an immediate appreciation of the total number of segments changing their functional status.

Table 4. Basics characteristics of patients included in this study (N=17)

Age, years	73.7 ± 8.6	
BMI	26.3 ± 6.2	
STS-PROM, %	6.1 ± 2.8	
NYHA Functional Class	II (%)	4 (23.5)
	III (%)	12 (70.6)
	IV (%)	1 (5.9)
Etiology of MR	Primary (%)	1 (5.9)
	Secondary (%)	16 (94.1)
Hospitalization for Heart Failure within 6 months (%)	3 (17.6)	
History of Congestive Heart Failure (%)	13 (76.5)	
Diabetes Mellitus (%)	5 (29.4)	
Coronary Artery Disease (%)	11 (64.7)	
Prior Myocardial Infarction (%)	7 (41.2)	
Prior CABG (%)	5 (29.4)	
Prior Percutaneous Coronary Intervention (%)	5 (29.4)	
Pacemaker Implanted (%)	7 (41.2)	
Prior Valve Intervention/Surgery (%)	0 (0)	
Peripheral Artery Disease (%)	2 (11.8)	
Current or Prior Smoker (%)	11 (64.7)	
COPD (%)	10 (58.8)	
Hypertension	13 (76.5)	
GFR < 60, mL/min	10 (58.8)	
Medications	ACE Inhibitor or ARB (%)	10 (59.8)
	Beta-receptor antagonist (%)	14 (82.4)
	Vasodilator (%)	1 (5.9)
	Diuretic (%)	14 (82.4)
	Digoxin (%)	3 (17.6)
	Anticoagulant (%)	9 (52.9)

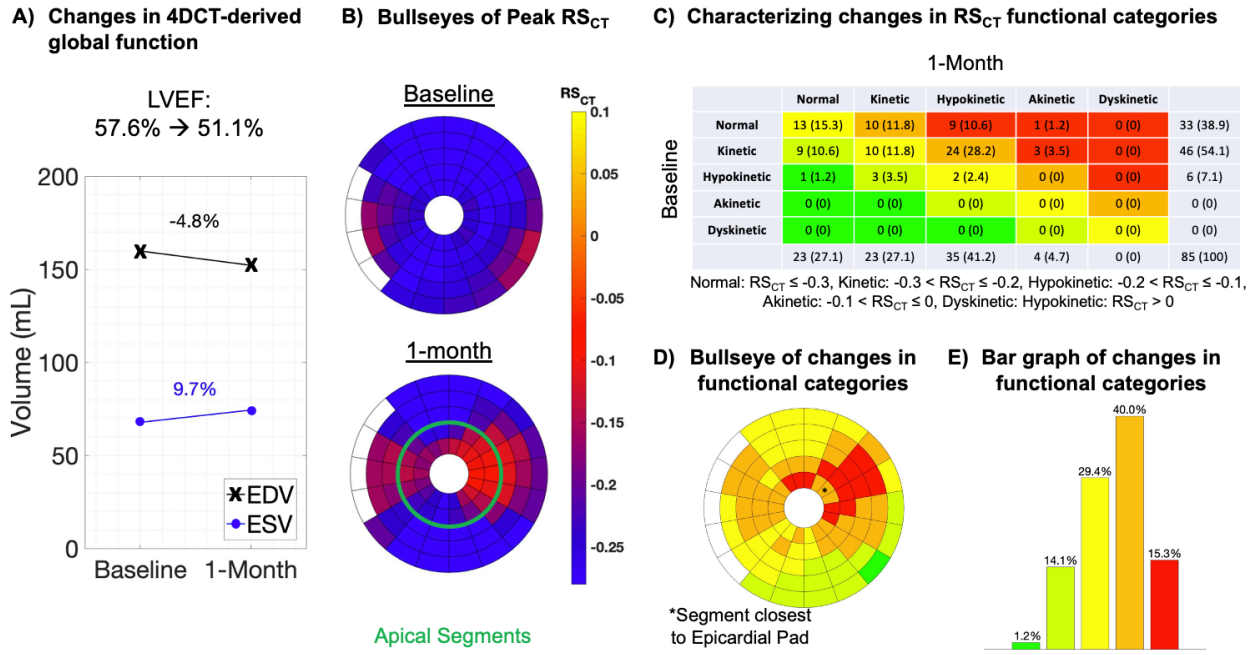

Figure 5. A) 4DCT-derived end-diastolic (ED) and end-systolic (ES) volumes were computed and used to calculate ejection fraction (EF) pre and post TMVI, B) Bullseye plots of peak RS_{CT} at baseline and 1-month post TMVI. The apical segments were defined as the two inner rings of the bullseye, C) Characterization of changes in regional function between baseline and 1-month: segments that did not change are shown in yellow, those that decreased by 1 category are orange, those that increased by 1 category are light green, and those that decreased or increased by 2+ categories are red or bright green, respectively, D) Bullseye plot showing the spatial distribution of the changes categorized in panel C, and E) Bar graph displaying the percentage of segments in a category from panel C.

From this preliminary study, it was clear from the baseline RS_{CT} maps shown in Figure 6 that the baseline LV functional state of the patients who received the Tendyne device was highly variable. From Figure 7, it is was also evident that the mechanical response to TMVI was highly variable between subjects, and the patterns of the change in RS_{CT} were highly localized and heterogeneous over the LV. Figure 8 contains illustrative comparisons between subjects with similar relative decreases in EF but regionally different mechanical responses to TMVI and are discussed further below.

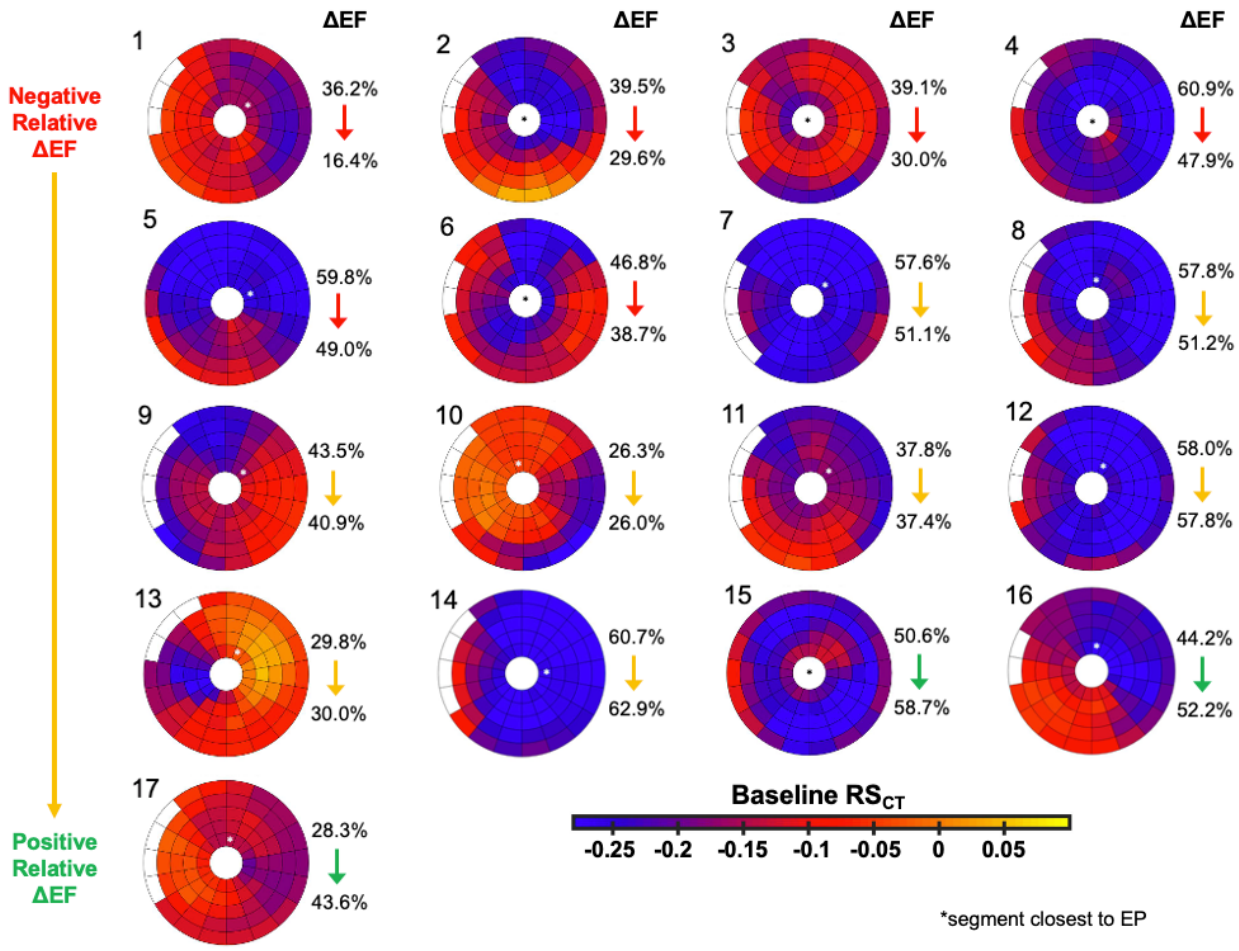

Figure 6. High resolution 90 segment (18 circumferential x 5 longitudinal) bullseye plots displaying baseline regional peak endocardial RS_{CT} (as shown in Figure 5B) for all 17 subjects. They are ordered from by the largest relative decrease in ejection fraction (EF) to the largest relative increase in EF. The segment closest to the epicardial pad (EP) is marked by the asterisk (*) and the change in EF between baseline and 1-month post TMVI is displayed next to the bullseye plot.

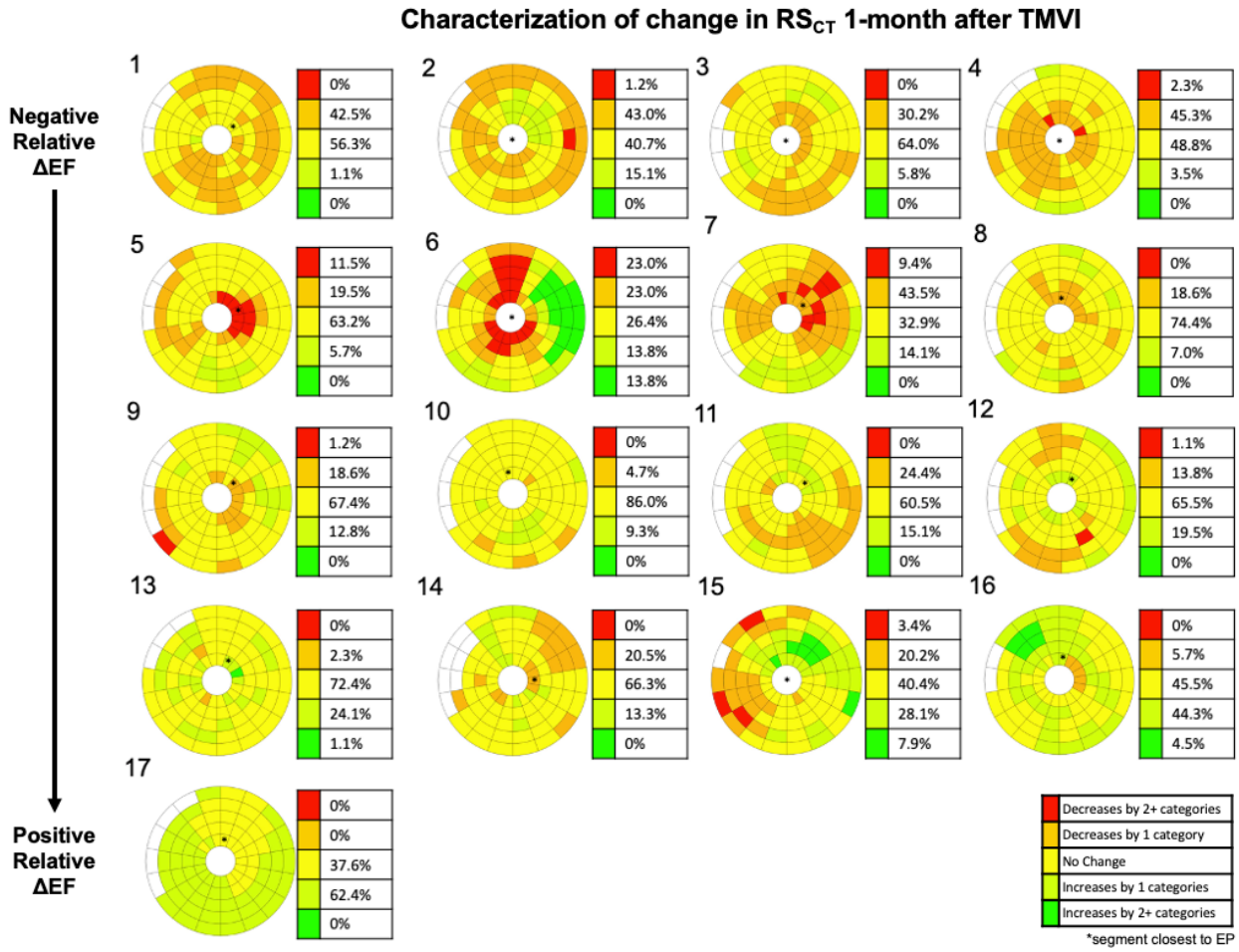

Figure 7. High resolution 90 segment (18 circumferential x 5 longitudinal) bullseye plots for all 17 subjects displaying changes between baseline and 1-month scans in the category of regional shortening: normal, kinetic, hypokinetic, akinetic, and dyskinetic (as shown in Figure 5D). Total percentages are also shown (as shown in Figure 5E). Again, subjects are ordered from by the largest relative decrease in ejection fraction (EF) to the largest relative increase in EF. The segment closest to the epicardial pad (EP) is marked by the asterisk (*).

2.3.2 Example comparisons between subjects with similar changes in ejection fraction

In this section, by way of two comparisons, we show the variable nature of both the original myocardial function pattern and the very different local response to TMVI while generating the same response according to EF.

Comparison 1: Subjects 1 and 2 in Figure 8A had baseline EFs ~39 percent and showed the same decrease in this global parameter after TMVI. Yet, their baseline functional maps were very different ($p<0.05$) and the changes in RS$_{CT}$ post implantation were also very different. At

baseline, subject 2 displayed global hypokinesia with some higher functioning tissue located in the apex. After TMVI, RS_{CT} in the apex was greatly reduced. For subject 1, at baseline a larger portion of tissue outside the apex on the anterior and antero-lateral wall was functioning well (20% was normal/kinetic in this region compared to 5% for subject 2). After TMVI, the magnitude of RS_{CT} *increased* in the anterior and antero-lateral apical region despite placement of the epicardial pad in the apex. In both subjects there was reduced function observed outside of the apical region. While an expected reduction in RS_{CT} is seen in many subjects in the apical regions near the epicardial pad, this does *not* explain the total change in local function as shown in these subjects.

Comparison 2: Subjects 3 and 4 had high pre TMVI EFs for this cohort (~58 percent) and had similar decreases in EF post TMVI, which is consistent with elimination of the substantial regurgitant volume. At baseline, subject 3 had mostly normal or kinetic tissue while subject 4 had a small region of hypokinetic tissue on the infero-septal wall. Post TMVI, patient 4 lost some function in the local region near the EP while subject 3 lost much more normal or kinetic tissue at the apex and surrounding tissue, as is evident in Figure 8B. However, in subject 3 there was a small region of tissue on the basal-inferior wall that has increased RS_{CT} post-procedure, while there was no localized change in RS_{CT} in subject 4 outside the apex.

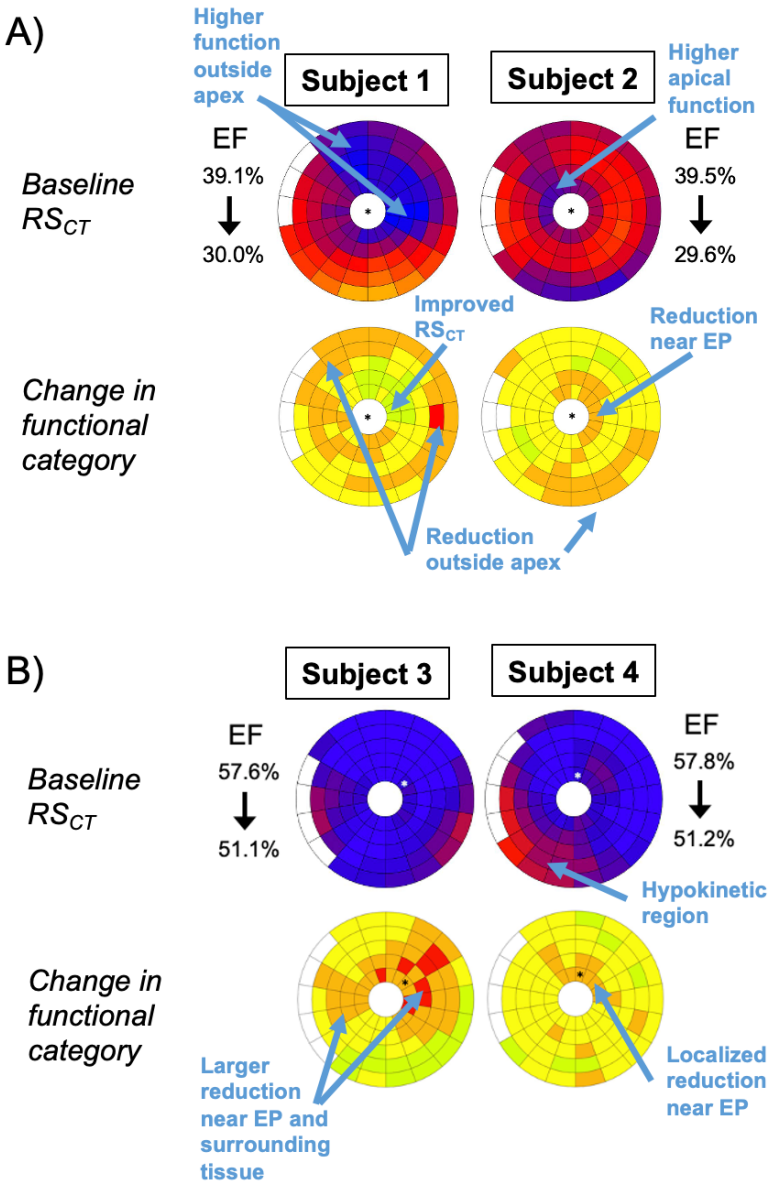

Figure 8. Example subjects are highlighted for comparison of baseline RS_{CT} patterns and changes in RS_{CT} 1-month after TMVI: A) subjects 1 and 2 showing decreased ejection fraction (EF) after TMVI and B) subjects 3 and 4 showing decrease in EF but relatively higher baseline EF. Regions of interest are labeled for each of these comparisons. *Epicardial Pad (EP)

2.3.3 Reproducibility of RS_{CT}

Both intra- and inter-observer variability were similar as shown in Figure 9. Segmental end-systolic RS_{CT} values were highly correlated for all three comparisons and the bias was small. The 95% confidence limit on the Bland-Altman plots for intra-observer variability was ±0.061 and for inter-observer variability it was ±0.053 as an average for the two comparisons. In addition,

Figure 9C shows for an example subject the 90 segment bullseye plots comparing Observer 1's first analysis, Observer 1's second analysis, and Observer 2's analysis. Despite small differences in RS_{CT}, the main features of these spatially heterogeneous regional shortening maps are extremely similar for all 3 analyses.

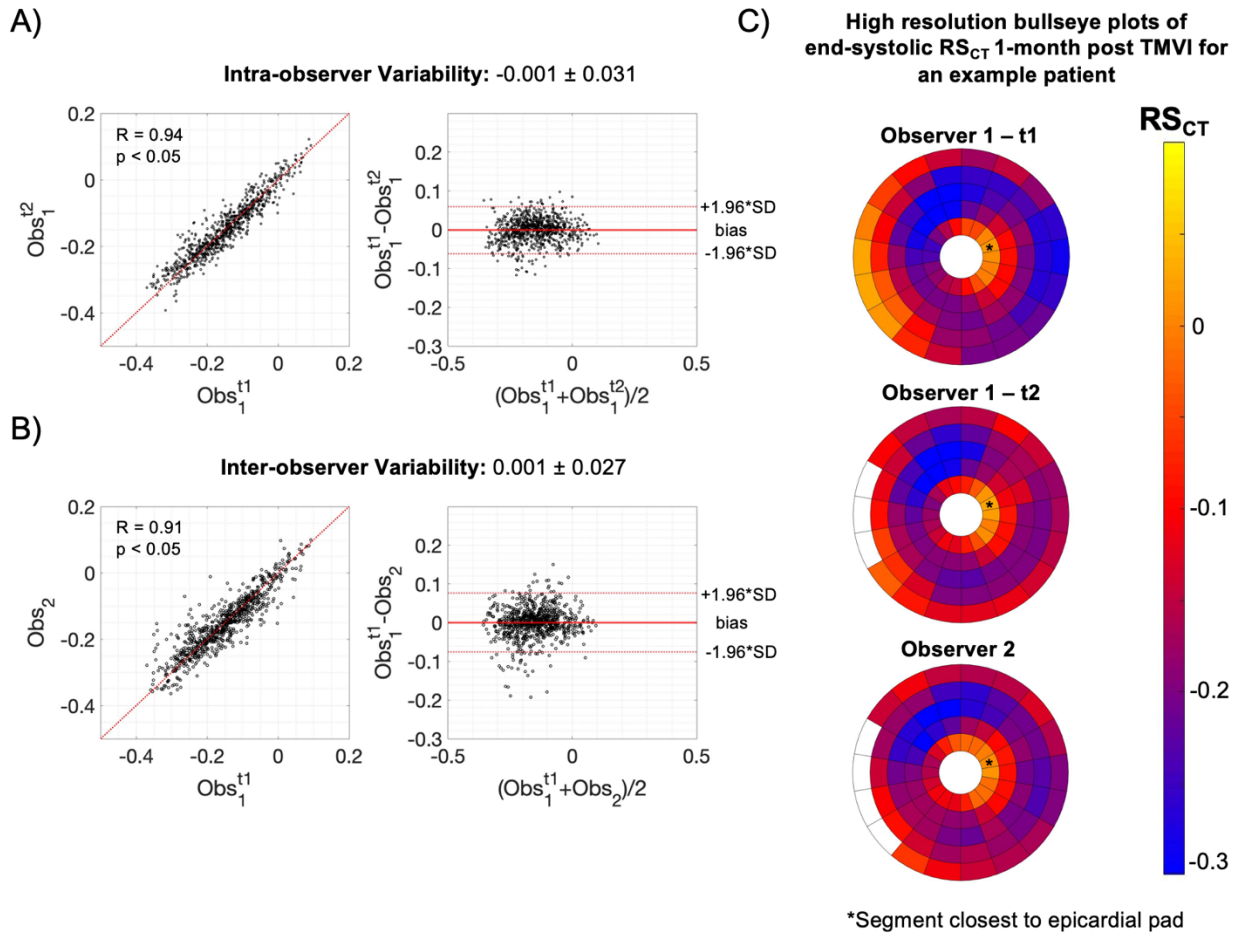

Figure 9. Correlation and Bland-Altman Plots comparing A) Observer 1's first (t2) and second analysis (t2), B) Observer 1's first analysis (t2) with Observer 2's analysis for a subset of 5 subjects for both baseline and 1-month 4DCT exams. C) High resolution bullseye plots of end-systolic RS_{CT} for an example patient 1-month post TMVI for all 3 independent analyses.

2.3.4 Observations of global LV metrics

In this small cohort of patients, there was a statistically significant change in ED volume post TMVI but no significant change in other global parameters such as ES volume (p=0.46), or EF (p=0.10) as shown in Figure 10. EF changed by less than 5 percent in 6 subjects. Three

subjects had an increase in EF with two subjects increasing between 5-10 percent and one patient increasing more than 10 percent. Eight subjects had a decrease in EF with five subjects decreasing between 5-10 percent and three subjects decreasing more than 10 percent.

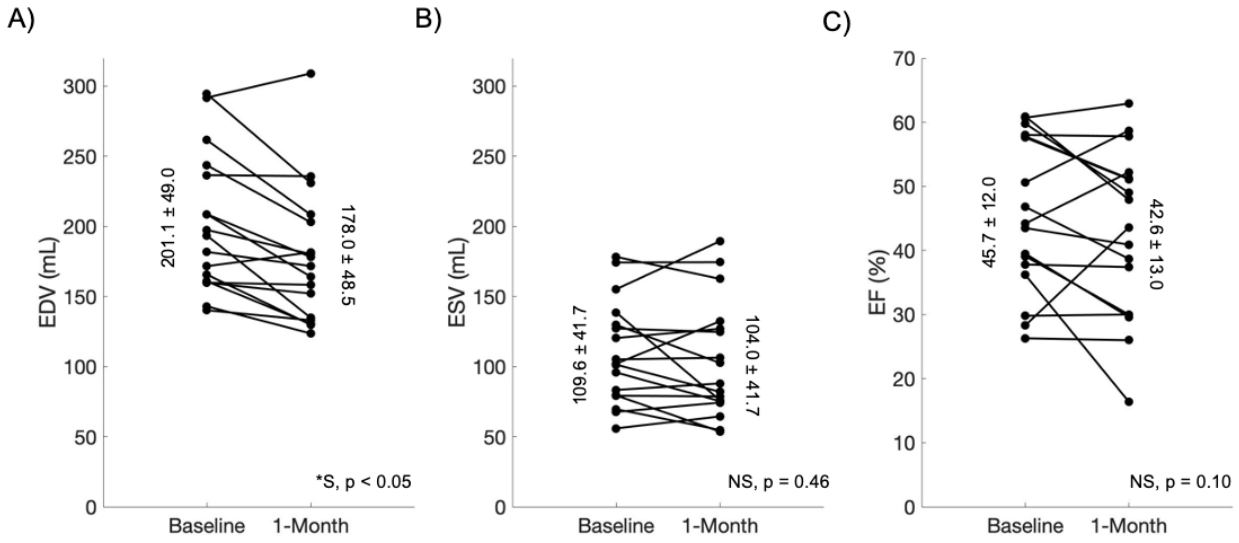

Figure 10. Changes in 4DCT-derived A) end-diastolic volumes (EDV), B) end-systolic volumes (ESV), and C) ejection fraction (%) before and 1-month after TMVI. Mean and standard deviation values are shown. Only EDV was significantly different at 1-month.

There was a wide diversity in the spatial patterns of regional function in both the pre and post TMVI hearts. Ten of the 17 subjects had 50 percent or more LV segments characterized as hypokinetic, akinetic, or dyskinetic (RS_{CT} > -0.20) at baseline. When analyzed in aggregate, the total number of segments classified as normal or kinetic tissue highly correlated with EF (R = 0.94, p<0.05) as expected (Figure 11A). Also, a decrease in EF post TMVI correlated with the percentage of segments that decreased by 1 or more functional categories (R = 0.78, p<0.05) (Figure 11B). Eight subjects showed a significant (p<0.05) positive shift in the distribution of RS_{CT} evaluated over all 90 segments using the two-sided, paired segmental Wilcoxon Signed rank test. This net positive shift of the classification of the segments corresponds to an overall decrease in LV function. Three subjects showed a significant (p<0.05) negative shift in the distribution of RS_{CT} over all 90 segments. Lastly, six subjects had a significant change in RS_{CT} (p<0.05) when looking only at the apical region (inner 18 segments of the bullseye). In some subjects, there was a clear

reduction in the magnitude, or absolute value, of RS_{CT} in the region of the EP, whereas in other subjects there was little or no change. Overall, a reduction of greater than 5 percent of normal or kinetic tissue in the LV and in the apex lead to a decrease in EF post TMVI. These are preliminary observations, however, and the small number of patients preclude analysis of trends in these data.

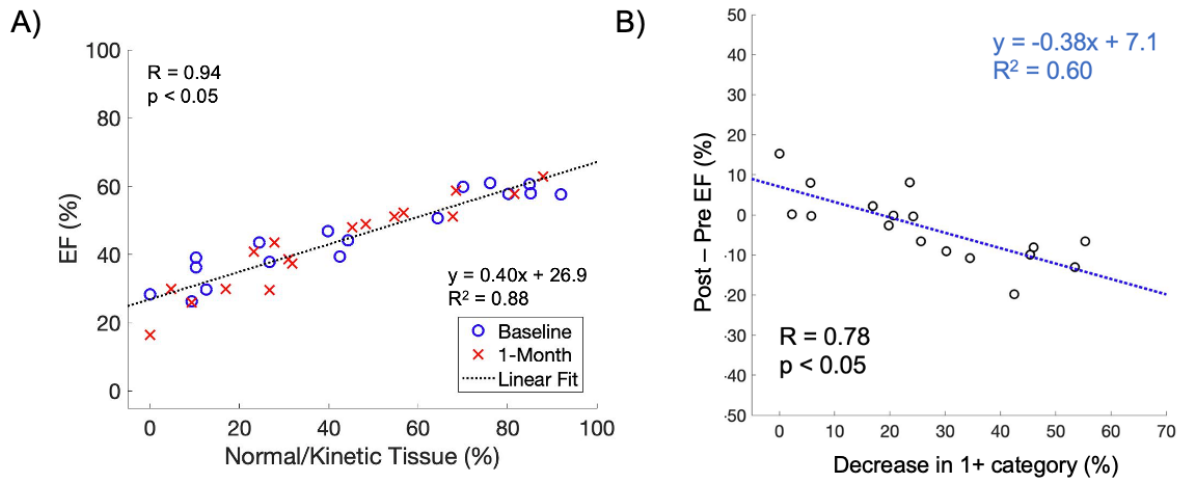

Figure 11. A) Ejection fraction (EF) is correlated with the percentage of normal/kinetic tissue in the left ventricle at baseline and 1-month after TMVI. Normal and kinetic tissue was defined any segment with $RS_{CT} \leq -0.2$. B) A change in EF is correlated with the percentage of tissue with decreases in 1 or more regional shortening categories.

2.4 Discussion

2.4.1 Main Findings

In this paper, we introduce a reproducible, high-resolution method (90 LV segments) for evaluating regional changes in LV endocardial shortening (RS_{CT}) before and 1-month after TMVI using 4DCT. These measurements of RS_{CT}, integrated with traditional clinical parameters and biomarkers, provide a more comprehensive analysis of the state of the heart and spatially detailed response to TMVI [31]. The majority of TMVI patients will undergo a contrast-enhanced 4DCT scan prior to the procedure to obtain annular measurements for device sizing [24], [25], [28]. It is recommended that for these measurements, images should be acquired across the entire cardiac cycle given the dynamic changes in the anatomical configuration of the LV, LVOT, and mitral

valve apparatus [25], [91]; therefore, our proposed analysis of regional LV function from the 4DCT images can be performed without extra radiation. In fact, large retrospective studies can be performed on existing data such as the Expanded Clinical Study of the Tendyne Mitral Valve System (NCT02321514) and Tendyne SUMMIT Clinical Trial (NCT03433274).

Despite their highly abnormal LV function and geometries, we were able to obtain high resolution estimates of RS_{CT} in all 17 subjects. The results of the reproducibility study performed on these subjects shows that the 95% confidence intervals are about 12% and 10% of the total dynamic range of RS_{CT} values observed in this patient population (about -0.39 to +0.12), respectively. Therefore, the measurement of RS_{CT} is a highly precise estimate of local LV function. It is evident from this initial proof-of-concept study that RS_{CT} patterns and the local changes in the mechanical response post implantation were extremely heterogeneous across all subjects assessed. While the majority (N=14) of subjects saw a less than 10 percent change in EF after the procedure, 11/17 (64.7%,) had a significant spatially heterogeneous changes in RS_{CT} across the entire LV, while the remaining 6/17 (41.2%) had significant changes just in the apical region. This result indicates that the functional states of these TMVI patients cannot be fully characterized with global parameters such as ED volume, ES volume, and EF. In addition, for patients with severe MR, EF may not capture the full picture of LV function because a significant proportion of the stroke volume flows retrograde into the left atrium and does not contribute to systemic perfusion [31].

Lastly, the resulting change in LV function after TMVI near the location of the epicardial pad had not yet been characterized. In this study, we were able to evaluate changes in RS_{CT} with high spatial resolution in the local region near the epicardial pad. We observed a highly variable effect of the epicardial pad on the local myocardial function in this small patient cohort; function can either decrease markedly, or even increase. The ability to resolve this kind of detail may prove useful in optimizing implantation procedures with larger patient datasets.

2.4.2 Limitations

The primary limitation of this preliminary study is the small number of patients analyzed; however, the results demonstrate that regional shortening from CT can measure both the baseline state of the endocardium, and changes in regional cardiac function with high spatial resolution and high precision without making *a priori* assumptions about LV geometry. In addition, with recent advances in CT scanners, including wide-detector technology, dual source x-ray, and high pitch acquisition platforms, ED and ES phases can now be acquired in a single heartbeat and at very low x-ray dose [29], [83]. Only one patient was excluded because of insufficient contrast between the LV blood pool and the myocardium leading to segmentation failure and, consequently, the inability to perform our analysis. Poor image quality from step artifacts can be avoided with single-beat CT technology.

2.5 Acknowledgements

Chapter 2, in part, has currently been submitted for publication of the material, Gabrielle M. Colvert, Ashish Manohar, Francisco J. Contijoch, James Yang, Jeremy Glynn, Philipp Blanke, Jonathon A. Leipsic, Elliot R. McVeigh. “Novel 4DCT method to measure regional left ventricular endocardial shortening before and after transcatheter mitral valve implantation.” The dissertation author was a primary author of this paper.

Chapter 3: Analysis of regional and global left ventricular function using 4DCT before and after cardiac resynchronization therapy

3.1 Introduction

As discussed in Chapter 1, there is currently an unmet clinical need for increasing the fraction of heart failure patients that respond to CRT. 4DCT has the potential to make a significant impact in this field because it is a robust imaging tool that can identify regions of scar [50], [78], [84], supply coronary vein morphology and location, and can be used to quantify LV dyssynchrony [45]. In this chapter, we evaluate the prognostic value of 4DCT-derived metrics of LV function, shape, and dyssynchrony for predicting both imaging- and clinically-based definitions of response to CRT.

3.2 Materials and Methods

3.2.1 Subjects

A subset of 83 patients was acquired from the "Empiric Versus Imaging-Guided Left Ventricular Lead Placement in Cardiac Resynchronization Therapy" (ImagingCRT) study [42], [50], [92]. All patients had symptomatic heart failure, (New York Heart Association [NYHA] classes II-IV despite optimal medical therapy), echo-derived LVEF ≤ 35%, electrocardiogram (ECG) QRS ≥ 120 milliseconds with left bundle-branch block (LBBB) morphology or RV paced QRS > 180 milliseconds. The patients involved in the study all received a CRT device at Aarhus University Hospital, Skejby, Denmark. The implantation procedure has been previously described in detail [42], [50], [92]. As part of this procedure, a lead was not placed in a segment of myocardium that was visually non-viable from the CT scan. Patients gave written consent prior to enrollment and the local ethics committee and the Danish Data Protection Agency approved the study.

3.2.2 Cardiac 4DCT imaging

Each patient had a retrospective, contrast-enhanced, ECG-gated 4DCT exam the day prior to implantation and 6 months after the procedure. Cardiac CT was performed using a

Somaton Definition Flash scanner (Siemens AG Healthcare, Forcheim, Germany) with a gantry rotation time of 280 milliseconds, tube voltage 80- to 120 kV, adaptive tube current with a reference of 370 mAs, and 128 x 0.6-mm collimation. Images were reconstructed in 5% intervals of the cardiac cycle (SAFIRE; Siemens AG Healthcare). An example patient's pre and post CRT 4DCT data is shown in Figure 12. Of the 83 total patients originally acquired, 44 had both pre and post procedure CT datasets which were analyzable and were therefore included in this current study.

Table 5 explains why certain patients were excluded from the 4DCT analysis.

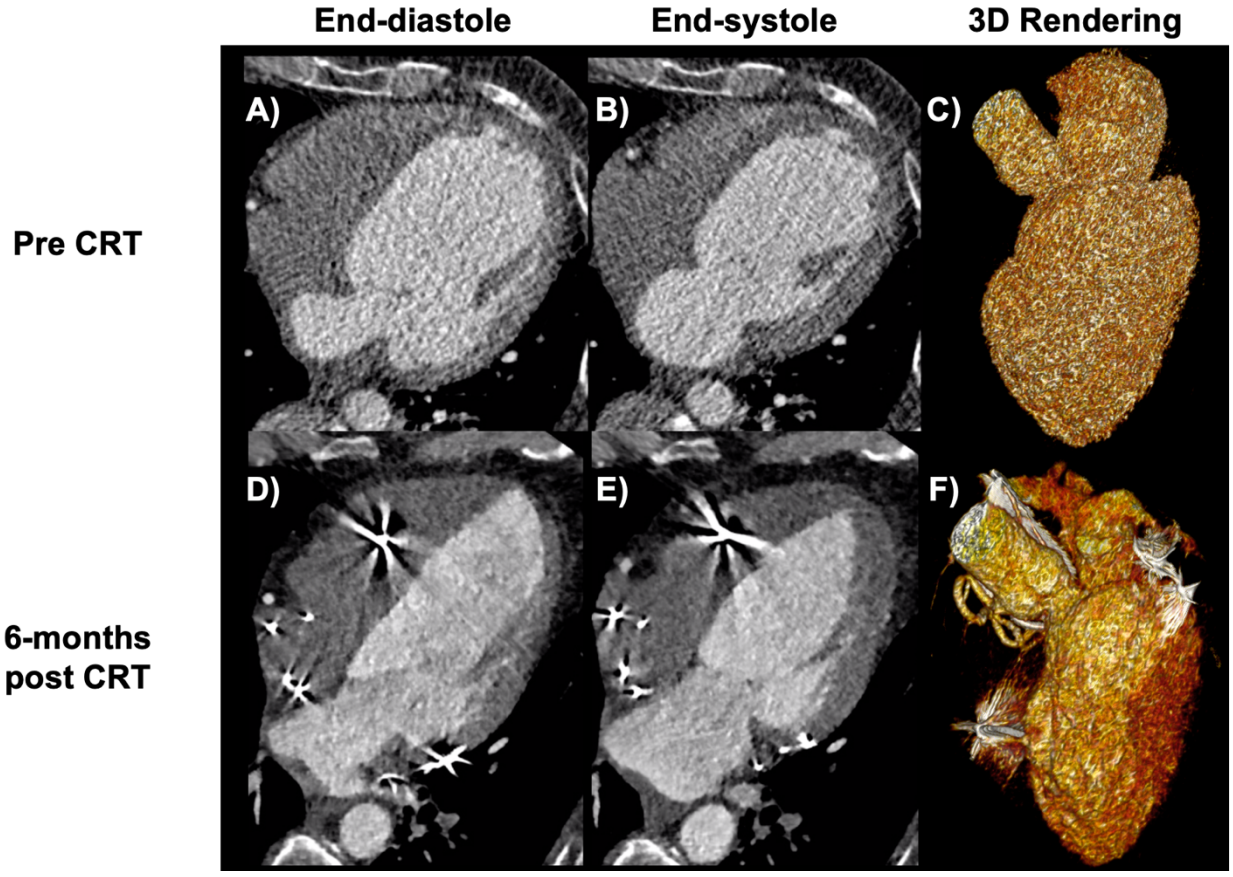

Figure 12. Patients with 4DCT exams pre and post Cardiac Resynchronization Therapy (CRT) were acquired**.** Axial images pre and post are shown for end-diastole (A,D) and end-systole (B,E). A posterior view of the 3D renderings of the end-diastolic volume pre (C) and post (F) CRT are also shown. The positions of the pacing leads are visualized precisely in both the 2D and 3D CT images.

Table 5. Forty-four out of 83 subjects with both pre and post 4DCT exams were included in this study. Thirty-nine subjects were not analyzed using 4DCT for the reasons described.

	Reason for images not analyzed	**n (%)**
Pre CRT	Helical step artifact	25/83 (30)
	Poor LV blood pool-myocardium contrast	3/83 (4)
	Lead artifact	1/83 (1)
	Part of LV blood pool cut off	2/83 (2)
Post CRT	Helical step artifact	2/83 (2)
	Poor LV blood pool-myocardium contrast	4/83 (5)
	Lead artifact	1/83 (1)
	Part of LV blood pool cut off	1/83 (1)
	Total	39/83 (47)

3.2.3 Left ventricular endocardial segmentation and identification of lead locations from 4DCT images

The LV blood pool was segmented from the contrast-enhanced 4DCT images in 3D using a region-growing algorithm in ITK-SNAP [93] as described above in section 2.2.2. Example segmentations at end-diastole pre and post CRT are shown in 2D (Figure 13A) and 3D (Figure 13B). The tips of the left and right leads were also labeled in the post CRT end-diastolic image. The tips of the leads were used to identify the position of the pacing electrodes because they were the most specific landmarks in the image. For regional metrics of cardiac function and dyssynchrony, the LV endocardial surface was divided into 90 (18 circumferential x 5 longitudinal) segments and displayed as a bullseye plot (Figure 13C). This segmentation process enabled identification of the endocardial segments closest to the tips of the leads.

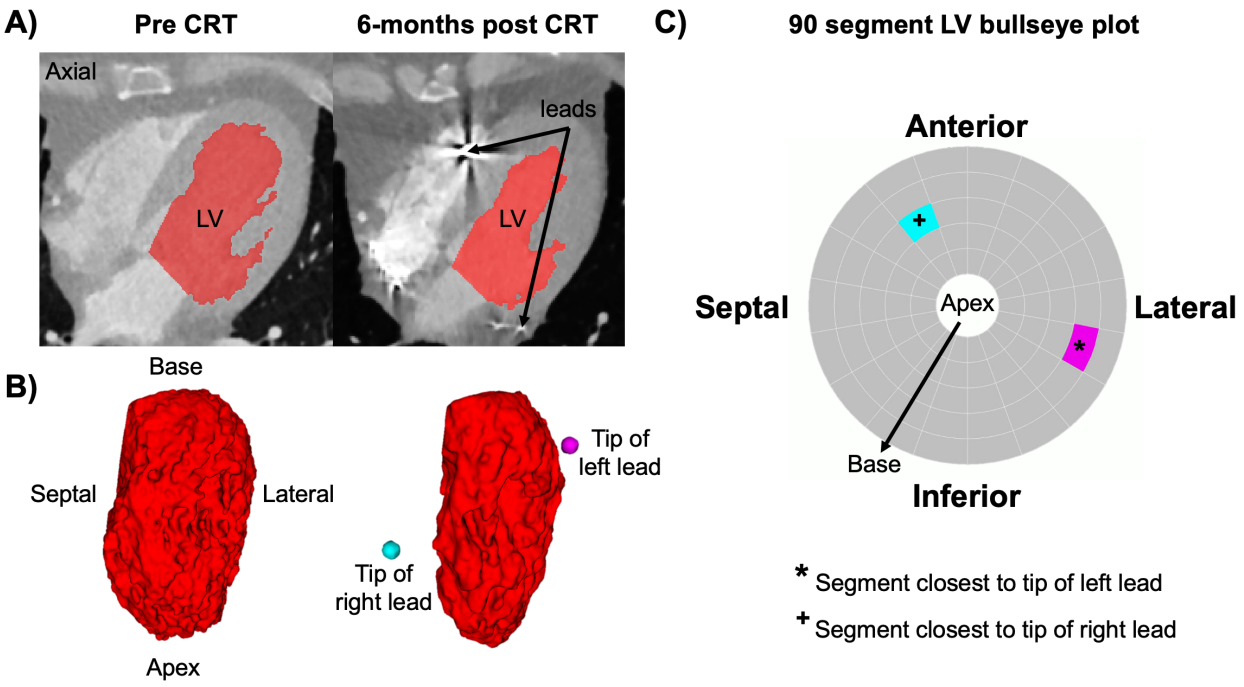

Figure 13. A) In order to quantify left ventricular (LV) volumes and analyze the shape and deformation of the endocardial surface pre and post CRT, the LV blood pool was segmented from the 4DCT images. B) The 3D renderings of these segmentation volumes are shown at end-diastole with the tip of the left and right leads labeled. C) This segmentation process allows for identification of the LV segment closest to the tip of the left and right leads in a 90 (18 circumferential x 5 longitudinal) segment bullseye plot.

3.2.4 Analysis of global and regional 4DCT-derived metrics of left ventricular shape, function, and dyssynchrony

3.2.4.1 4DCT-derived left ventricular volumes and ejection fraction

LV volumes were computed from the 4DCT images by counting the number of voxels identified as blood pool in the LV segmentation from the tip of the endocardial apex to the mitral valve plane at each timeframe across the cardiac cycle. End-diastolic volume (EDV) was measured as the LV volume at 0 milliseconds from the QRS scanner trigger. End-systolic volume (ESV) was measured at the timeframe where the minimum LV volume occurred. These volumes were obtained by counting voxels included in the LV blood pool segmentation which excluded the papillary muscles. EDV and ESV were used to calculate EF as shown in Figure 14A.

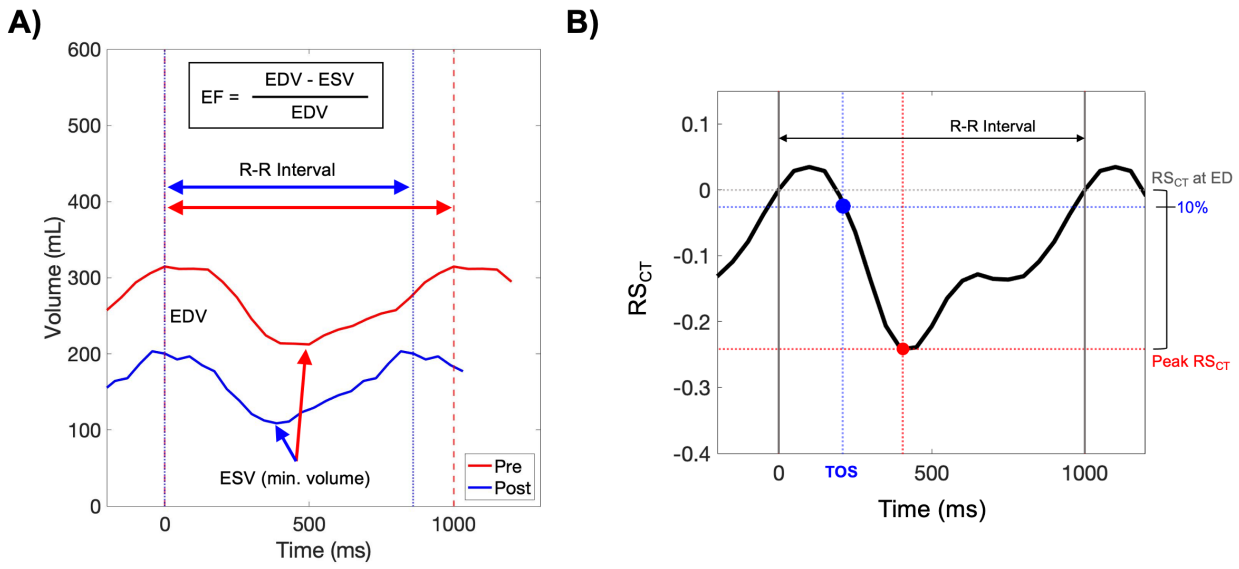

Figure 14. A) End-diastolic volume (EDV) and end-systolic volume (ESV) were derived from the 3D segmentation volumes by counting the number of pixels labeled as LV blood pool pre and post CRT. End-diastole (ED) was defined as 0% of the R-R interval, or 0 milliseconds from the QRS scanner trigger. End-systole (ES) was defined as the timeframe where the minimum LV volume occurred. Ejection fraction (EF) was also measured using EDV and ESV. B) Regional endocardial shortening (RS_{CT}) was measured pre and post CRT and plotted versus time for 90 LV segments; the curve for one segment is shown. Peak RS_{CT} was identified as the minimum point on the curve (red). The time to onset of shortening (TOS) was defined as the time where the segment reaches 10% of the dynamic range of shortening from ED to peak RS_{CT} (blue).

3.2.4.2 4DCT-derived regional left ventricular endocardial shortening

CT regional endocardial shortening (RS_{CT}) was measured pre and post CRT as previously described in section 2.2.2. RS_{CT} was plotted versus time for 90 LV segments; the curve for one segment is shown in Figure 14B. Peak RS_{CT} was identified as the minimum point on the curve (red). TOS was defined as the time where the segment reached 10% of the dynamic range of shortening from ED to peak RS_{CT} (blue). Peak RS_{CT} and TOS in the segments closest to left and right leads were recorded.

In addition to these regional metrics, global mechanical dyssynchrony was quantified using the CURE index. From the 90-segment bullseye plot at each timeframe, RS_{CT} was plotted as a function of wall position, p, in 18 uniformly spaced segments for three slices that encompassed the full ventricle below the LV outflow tract (inner 3 rings of bullseye) (s = 1, 2, 3).

These slices correspond to similar measurement locations used in both MRI and echo. The most basal slices (outer two rings of the bullseye plot) were not included in the CURE analysis to avoid discontinuities due to the LV outflow tract. As shown in Figure 15, each vector, **x**(p), at time, t, and slice, s, was subjected to Fourier Analysis using MATAB's built-in function *fft.* A function, C(s,t), was defined as

$$\mathrm{C}(\mathrm{s},\mathrm{t}) = \sqrt{\frac{|f_0|}{|f_0| + 2|f_1|}} \tag{3.1}$$

where f_0 and f_1 are the zero and first order Fourier coefficients, respectively [44]. If C(s,t) = 1, then contraction in that slice was perfectly synchronous. Dyssynchronous contraction was indicated by C(s,t) < 1. In this study, we defined two CURE indices, $CURE_{sys}$ and $CURE_{tot}$, using the values of C(s,t). To calculate $CURE_{sys}$, C(s,t) was averaged over space and time, but only from the end-diastolic timeframe +1 (t_{ed+1}) to the end-systolic timeframe (t_{es}). $CURE_{tot}$ included all timeframes from t_{ed+1} to the end of the R-R interval (t_{end}).

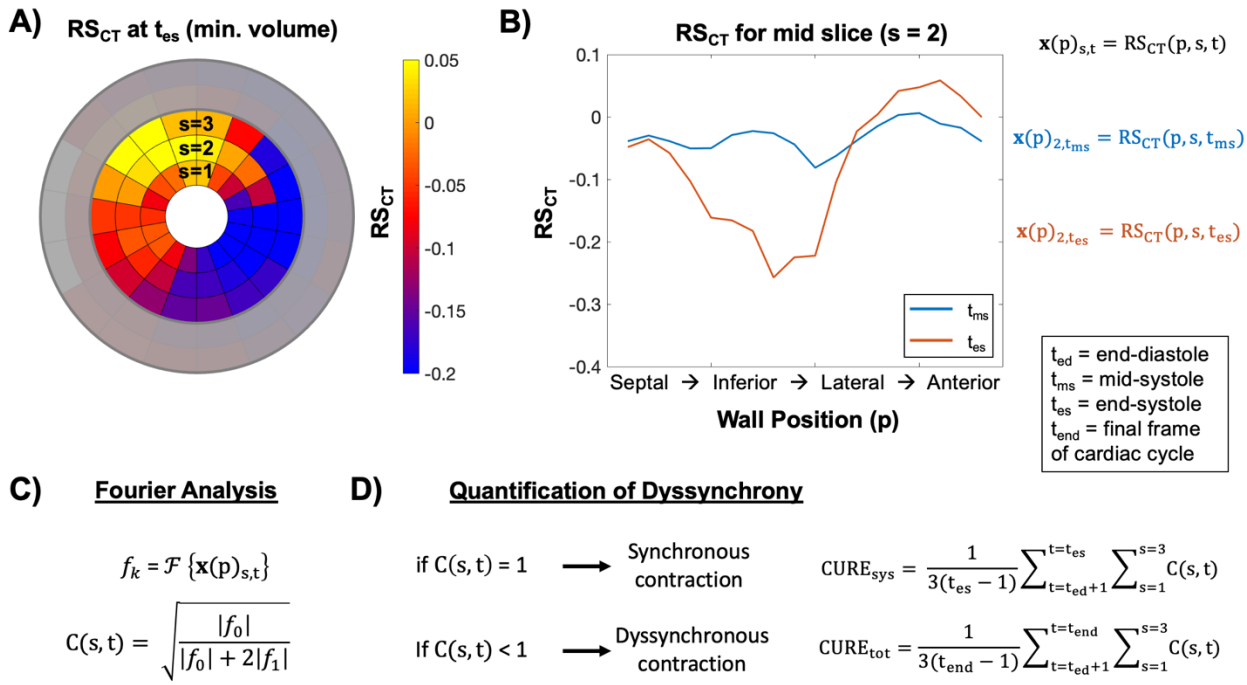

Figure 15. A) 90 segment bullseye plot of RS_{CT} at end-systole (ES). CURE is calculated for the 3 inner rings of the bullseye (s=1,2,3) to avoid discontinuities due to the location of the LV outflow tract. B) RS_{CT} is plotted for the middle slice (s=2) as a function of wall position, p, for two different timeframes: mid-systole (ms) and ES (es). C) Fourier analysis is performed on the $x(p)_{s,t}$ curves and C(s,t) is defined using the zero (f_0) and first-order (f_1) Fourier coefficients as shown. D) If C(s,t) is closer to 1, then contraction is synchronous while a C(s,t) closer to 0 indicated dyssynchronous contraction. In this study, we evaluated two CURE indices. $CURE_{sys}$ is averaged over space and time but only from t_{ed+1} to t_{es}, while $CURE_{tot}$ included all timeframes reconstructed across the R-R interval (t_{end}).

3.2.4.3 4DCT-derived left ventricular endocardial sphericity

LV sphericity (Sph) describes the relationship between the length of the long-axis to the width of the short-axis [94]–[96]. In this study, principal component analysis (PCA) was used to derive the sphericity of the endocardial surface at ED and ES. Using MATLAB's built-in *pca* function, the principal component axes, or the eigenvectors of the covariance matrix, and the associated eigenvalues were derived for the three spatial coordinates of the ED and ES point clouds with the long-axis of the LV aligned with the z-axis. Then, sphericity was defined as the ratio of the eigenvalue for third principal component (PC3) to the eigenvalue for the first principal component (PC1) [97]. This process is summarized in Figure 16 and shows two example subjects

prior to CRT; the first subject had high LV sphericity (A, closer to Sph=1) and the second had low LV sphericity (B, closer to Sph=0).

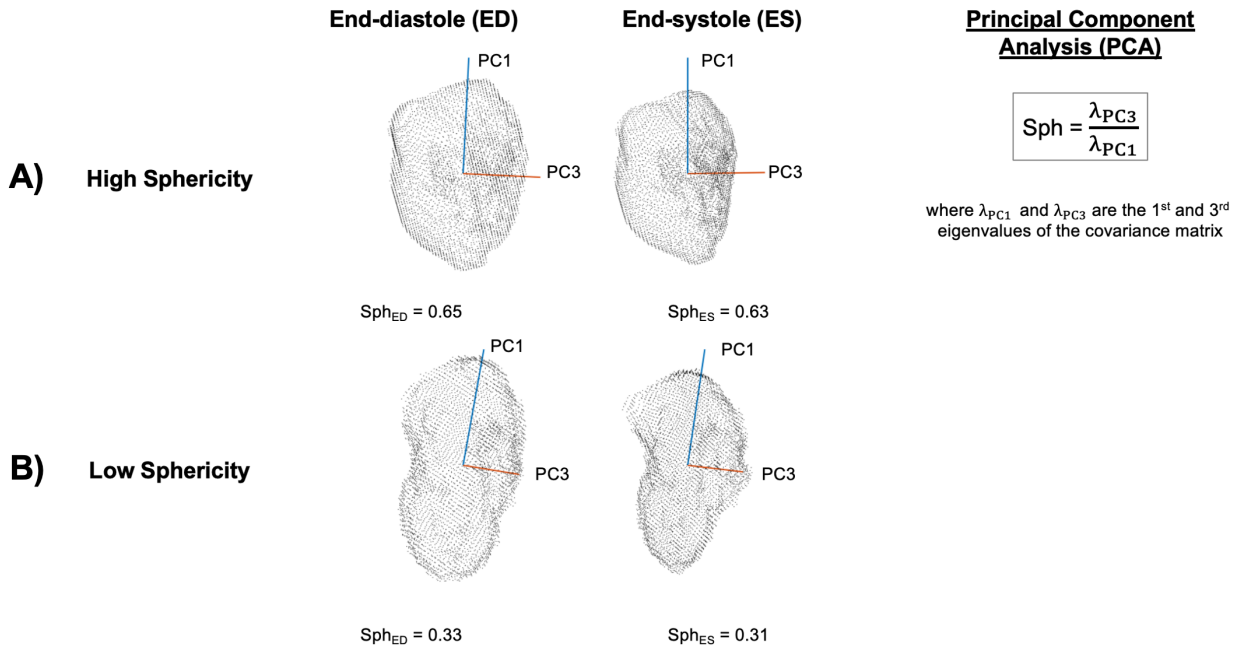

Figure 16. Principal component analysis (PCA) was used to derive the sphericity (Sph) of the endocardial surface at end-diastole and end-systole. Sphericity describes the relationship between the length of the long-axis to the width of the short-axis using the eigenvalues of the covariance matrix of the point cloud defining the endocardial surface. The first and third principal axes defined by the eigenvectors of the covariance matrix, or principal component 1 (PC1) and principal component 3 (PC3) are used. Two example subjects are shown with high sphericity (A, closer to Sph=1) and low sphericity (B, closer to Sph=0).

3.2.5 Comparison of 4DCT- and 2D echocardiography-derived left ventricular global metrics of left ventricular function

As part of the ImagingCRT study, all patients underwent echocardiographic evaluation pre and 6-months post implantation of the CRT device. Echo studies were performed on a commercially available system (Vivid E9, GE Medical Systems, Horten, Norway) and analyzed offline (EchoPac BT11-12, GE Medical Systems). ESV, EDV, and EF were estimated using Simpson's biplane method [50]. These 2D echo-derived volumes and EFs were compared to the 4DCT-derived volumes and EFs for the 44 subjects included in this study. Absolute change in EF and percent change in ESV pre and post CRT were also calculated. Classification of response to

CRT base on CT and echo definitions was compared. Correlation coefficients between the estimates from the two imaging modalities were computed using MATLAB's built-in function *corcoeff*. After this comparison was performed, only the CT-derived values were used in further analysis for imaging-based definitions of CRT response. In this study, we evaluated three different definitions that have been used previously to define response to CRT: 1) ≥5% increase in 4DCT-derived EF, 2) ≥15% decrease in 4DCT-derived ESV, and 3) clinical response defined as improvement in NYHA class and 10% increase in the 6 min walk test, or freedom from hospitalization for heart failure or death.

3.2.6 Development of the lead placement score using linear discriminant analysis

To evaluate the prognostic value of the 4DCT-derived metrics of LV shape, function, and dyssynchrony described above, linear discriminant analysis (LDA) was used to create a lead placement score (LPS) for the three different definitions of response. The 4DCT-derived input variables of EF, EDV, ESV, $CURE_{tot}$, $CURE_{sys}$, TOS near the left lead, Peak RS_{CT} near the left lead, Sph_{ED}, and Sph_{ES} were all considered for inclusion in the LPS.

MATLAB's built-in function *fitdiscr* was used to fit a LDA model to the set of input predictors given the response classifications and use of an empirical prior. 5-fold cross-validation was used to detect overfitting of the model. The intercept and linear coefficient terms were recorded for each of the 5 folds. Due to the small sample size and random splitting of training and validation cohorts, the output parameters of the model were subject to some variation. In order to obtain confidence intervals on the model coefficients and intercept, the process of model fitting was repeated for 1000 random permutations of the 5 folds. MATLAB's *kfoldpredict* function was used to obtain the predicted scores for each of the 1000 models. Then, MATLAB's *perfcurve* function was used to create the receiver operating characteristic (ROC) curves using these scores with the positive class label as 'responder.' Using linear interpolation, the ROC curves were combined

and the 5th, 50th, and 95th percentile curves were computed. These ROC curves were compared to an ROC curve which was generated using just 4DCT-derived EF as the predictor.

The model fitting was repeated for different combinations of predictors. The model with the highest median area under the curve (AUC) and highest negative predictive value (NPV) was chosen for the parameters of the LPS. From that best performing model, the median coefficients and intercept from the 5 folds and 1000 iterations were computed. These output parameters were then used to calculate an LPS for each of the 44 patients included in the study. A new ROC curve was computed using those scores and compared to the median ROC from the model fitting process. From the LPS scores, an example threshold was chosen to balance the total number of false negatives and false positives and a new non-responder rate was calculated. A LPS was computed for the two CT-based definitions of response to CRT as well as the clinical definition of response.

3.3 Results

3.3.1 Study Population

Of the original 83 patients acquired, 44 subjects had both pre and post 4DCT exams which were analyzable. Of the 39 total patients which were excluded, almost 70% (27/39) of them could not be analyzed because of a helical step artifact which distorted the endocardial surface. The second most common reason for exclusion (7/39) was inadequate contrast between the LV blood pool and the myocardium most likely due to poor timing of the contrast injection. The baseline clinical characteristics of the 44 subjects included in this study are shown in Table 6. About 90% of the subjects had LBBB, 20% had chronic right ventricular pacing, and 35% had atrial fibrillation. For the two CT-based definitions of response to CRT, 20/44 (45.5%) subjects were considered non-responders with a change in 4DCT-derived EF less than 5% and 16/44 (36.4%) subjects were classified as non-responders with a percent change in ESV less than 15%. Based on the criteria for a clinical response to CRT, 13/44 (29.5%) were considered non-responders.

Table 6. Baseline clinical characteristics of the subjects included in this study.

N	44	
Male, n (%)	36 (81.8)	
Age, y	71.2 ± 7.7	
BMI, kg/m^2	26.9 ± 4.4	
Medical history, n (%)	Hypertension	12 (27.3)
	Diabetes mellitus	13 (29.5)
	Chronic obstructive pulmonary disease	3 (6.8)
	Ischemic cardiomyopathy	26 (59.1)
	Prior myocardial infarction	19 (43.2)
	Prior coronary artery bypass grafting	10 (22.7)
NYHA class, n (%)	II	22 (50.0)
	III	20 (45.5)
	IV	2 (4.5)
Atrial fibrillation, n (%)	Paroxysmal	7 (15.9)
	Permanent	9 (20.5)
Medicine, n (%)	β-blockers	38 (86.4)
	ACEI/ARB	41 (93.2)
	Loop diuretics	26 (59.1)
	Spironolactone	18 (40.9)
QRS width, ms	175.7 ± 23.3	
Left bundle branch block, n (%)	40 (90.9)	
Chronic right ventricular pacing, n (%)	9 (20.5)	
eGFR, mL/min per 1.73m^2	67.1 ± 15.6	
Nt-ProBNP, pg/mL	2363 ± 1962	

3.3.2 Comparison of echo- and 4DCT-derived global left ventricular function

We compared 2D echo- and 4DCT-derived left ventricular ESV, EDV, and EF as shown in Figure 17. Correlation was good between the two imaging modalities for baseline EDV (R=0.73, p<0.001) and ESV (R=0.76, p<0.001) and moderate for baseline EF (R=0.58, p<0.001). There was poor correlation between 2D echo and 4DCT post ESV, EDV, and EF. Agreement between the two modalities for classification of response to CRT was moderate based on percent change

in ESV (Figure 18A) and absolute change in EF (Figure 18B). Based on the established thresholds of response for both parameters, echo classified more subjects as responders to the procedure than CT. The echo-derived volumes and EF were not used further in the analysis. All imaging-based definitions of response used the 4DCT-derived values.

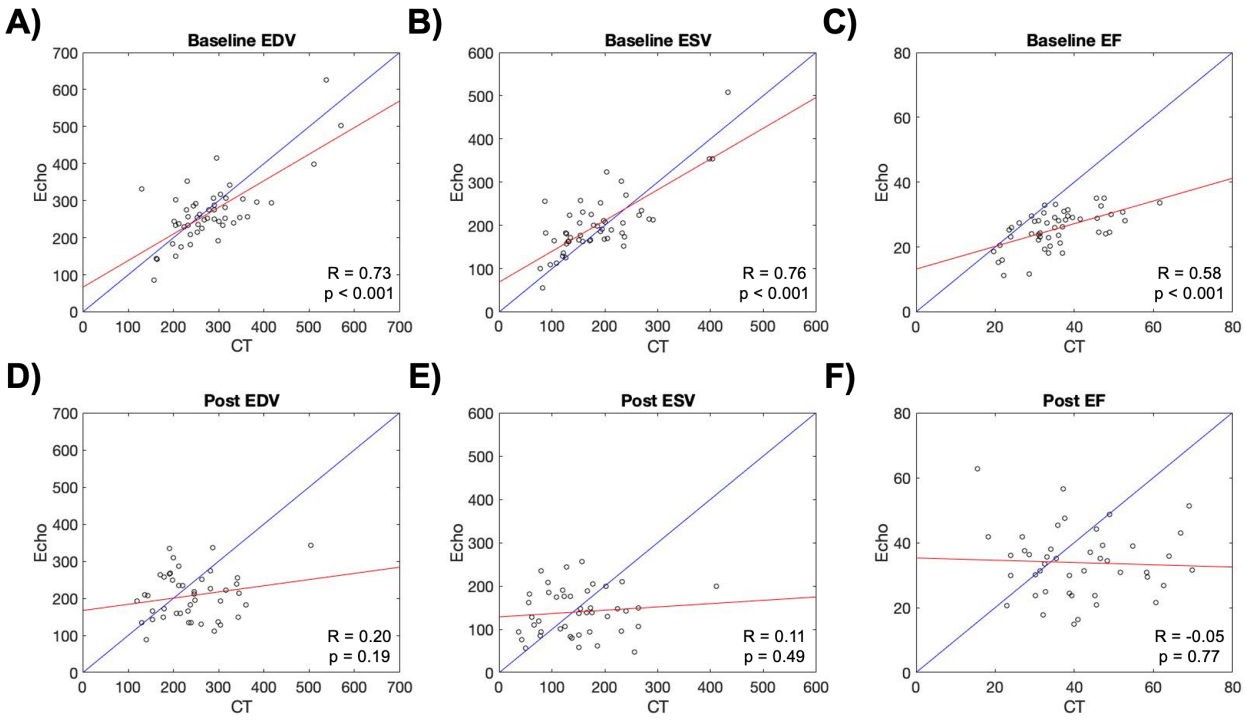

Figure 17. End-diastolic volume (EDV), end-systolic volume, (ESV), and ejection fraction (EF) were computed using both 2D echocardiography (Simpson's method) and 4DCT (from the 3D segmentation volumes) for all subject included in this study. These parameters were compared before (A, B, C) and 6-months after (D, E, F) CRT. The blue line is the line of identity and the red line is the linear fit through the points. Correlation coefficients and their corresponding p-values are also shown.

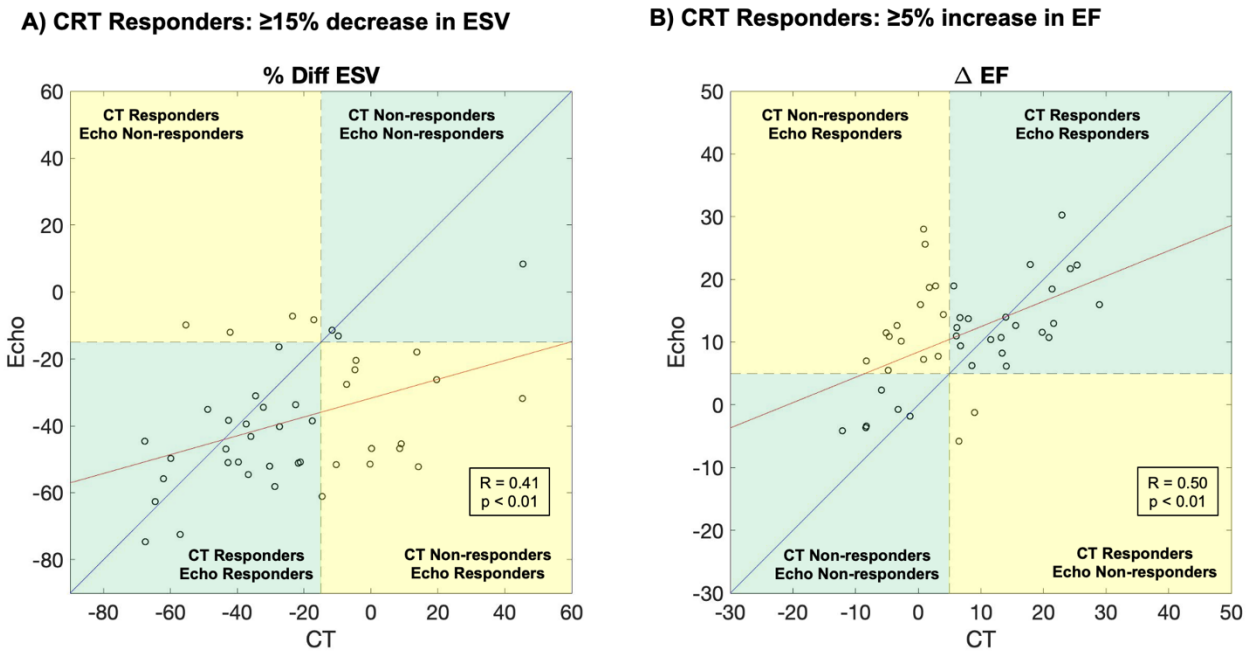

Figure 18. A) Correlation plot showing CT- and echo-derived percent changes in end-systolic volume (ESV) between baseline and 6-months post CRT. Responders for both modalities are subjects with ≥15% decrease in ESV. B) Correlation plot showing CT- and echo-derived changes in ejection fraction (EF) between baseline and 6-months post CRT. Responders for both modalities are subjects with ≥5% increase in EF. The line of identity is shown in blue and the linear fit through the points is shown in red. Correlation coefficients and their corresponding p-values are also shown. Regions where echo and CT agree on responder classification are highlighted in green and regions where the two modalities disagree are highlighted in yellow. Echo volumes were not used for further analysis in this work.

3.3.3 4DCT-based metrics of left ventricular shape, function, and dyssynchrony

The distributions of EF (Figure 19) , EDV and ESV (Figure 20), $CURE_{tot}$ and $CURE_{sys}$ (Figure 21), peak RS_{CT} and TOS (Figure 22), and Sph_{ED} and Sph_{ES} (Figure 23) in responders and non-responders prior to CRT were displayed as boxplots for all 3 definitions of response to CRT. Absolute changes pre and post CRT in $CURE_{tot}$ and $CURE_{sys}$ (Figure 24) and Sph_{ED} and Sph_{ES} (Figure 25) were also displayed as boxplots. Two-sided t-tests were performed to evaluate the differences in the distributions of all these parameters in responders and non-responders. In all figures, distributions that were significantly different are marked with an asterisk (*). This analysis was used to inform which parameters we should initially include in the fitting of the modes to create the LPS.

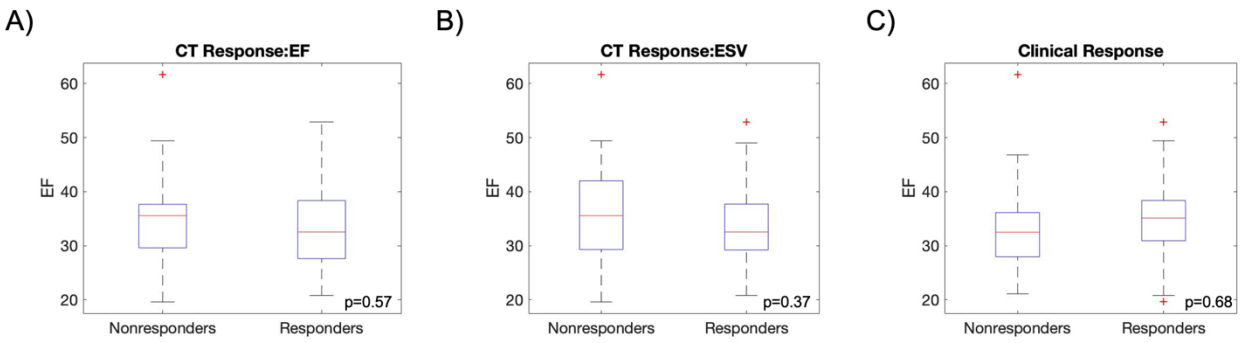

Figure 19. Boxplots displaying the distributions of 4DCT-derived ejection fraction (EF) pre-CRT in responders and non-responders for the three definitions of response to CRT: A) ≥5% increase in EF, B) ≥15% decrease in end-systolic volume (ESV), and C) clinical response defined as improvement in New York Heart Association (NYHA) class and 10% increase in the 6 min walk test, or freedom from hospitalization for heart failure or death. Two-sided t-tests were performed to evaluate differences in the distributions with a significance level set to 0.05. The resulting p-values for these tests are also shown.

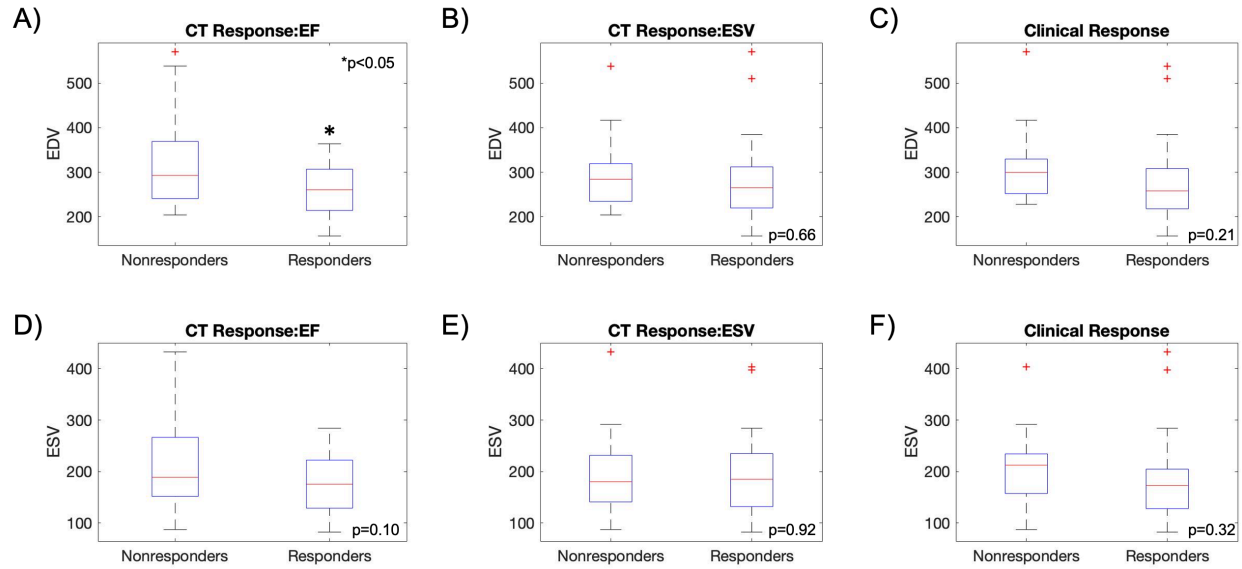

Figure 20. Boxplots displaying the distributions of 4DCT-derived end-diastolic volume (EDV) and end-systolic volume (ESV) pre CRT in responders and non-responders for the three definitions of response to CRT: (A,D) ≥5% increase in EF, (B,E) ≥15% decrease in end-systolic volume (ESV), and (C,F) clinical response defined as improvement in New York Heart Association (NYHA) class and 10% increase in the 6 min walk test, or freedom from hospitalization for heart failure or death. Two-sided t-tests were performed to evaluate differences in the distributions with a significance level set to 0.05. The resulting p-values for these tests are also shown. Significant differences are marked with an asterisk (*).

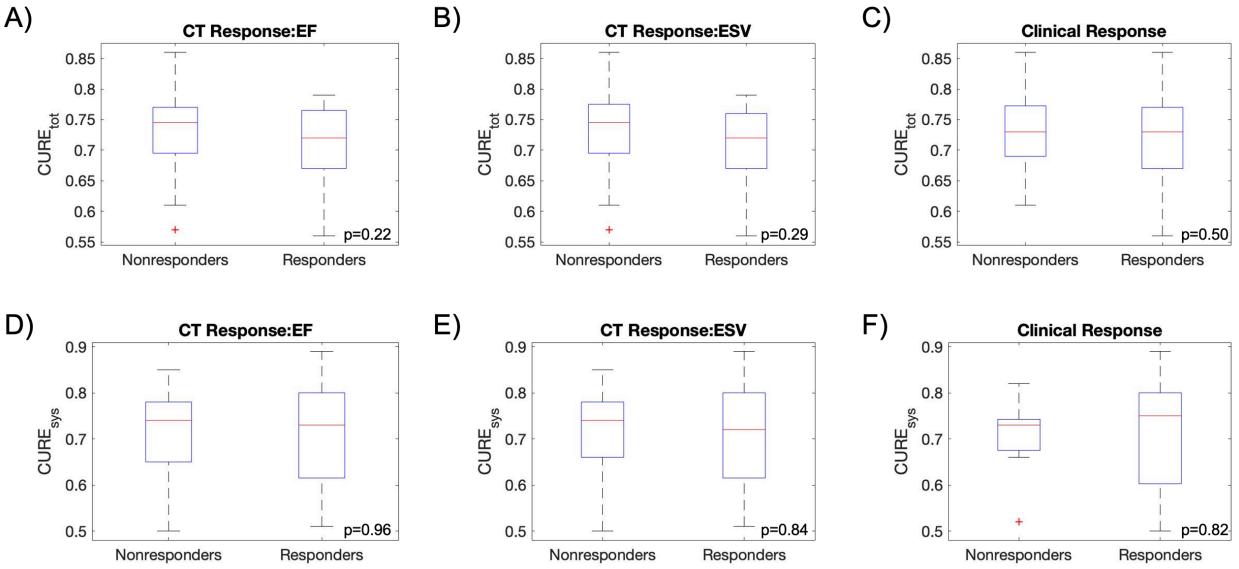

Figure 21. Boxplots displaying the distributions of 4DCT-derived $CURE_{tot}$ and $CURE_{sys}$ pre CRT in responders and non-responders for the three definitions of response to CRT: (A,D) ≥5% increase in EF, (B,E) ≥15% decrease in end-systolic volume (ESV), and (C,F) clinical response defined as improvement in New York Heart Association (NYHA) class and 10% increase in the 6 min walk test, or freedom from hospitalization for heart failure or death. Two-sided t-tests were performed to evaluate differences in the distributions with a significance level set to 0.05. The resulting p-values for these tests are also shown.

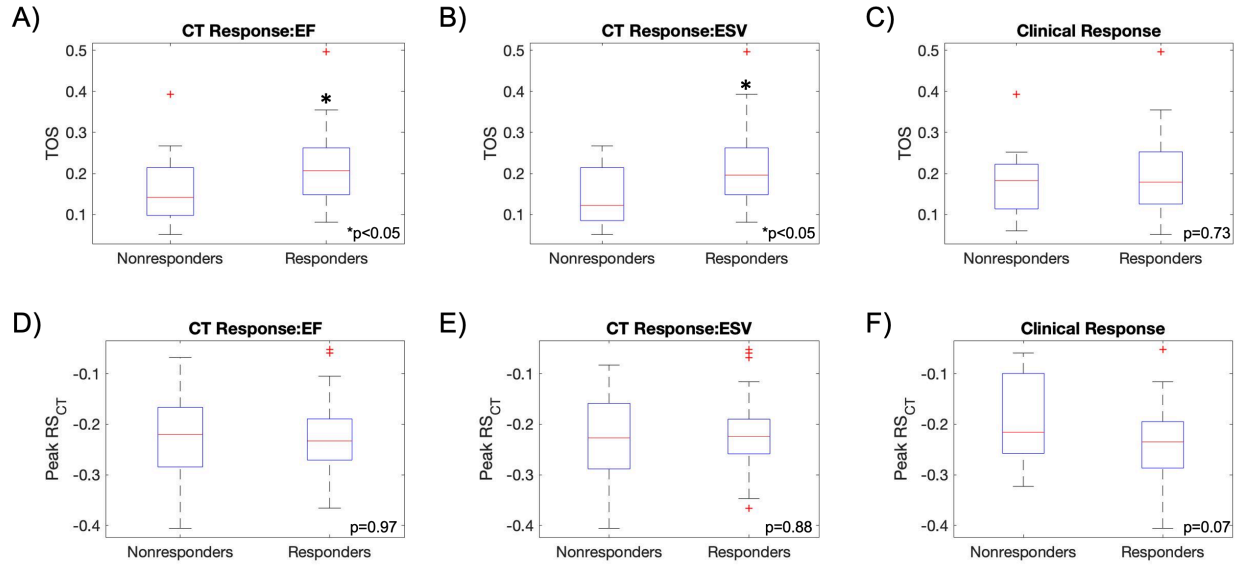

Figure 22. Boxplots displaying the distributions of 4DCT-derived time to onset of shortening (TOS) and peak RS_{CT} near the left lead pre CRT in responders and non-responders for the three definitions of response to CRT: (A,D) ≥5% increase in EF, (B,E) ≥15% decrease in end-systolic volume (ESV), and (C,F) clinical response defined as improvement in New York Heart Association (NYHA) class and 10% increase in the 6 min walk test, or freedom from hospitalization for heart failure or death. Two-sided t-tests were performed to evaluate differences in the distributions with a significance level set to 0.05. The resulting p-values for these tests are also shown. Significant differences are marked with an asterisk (*).

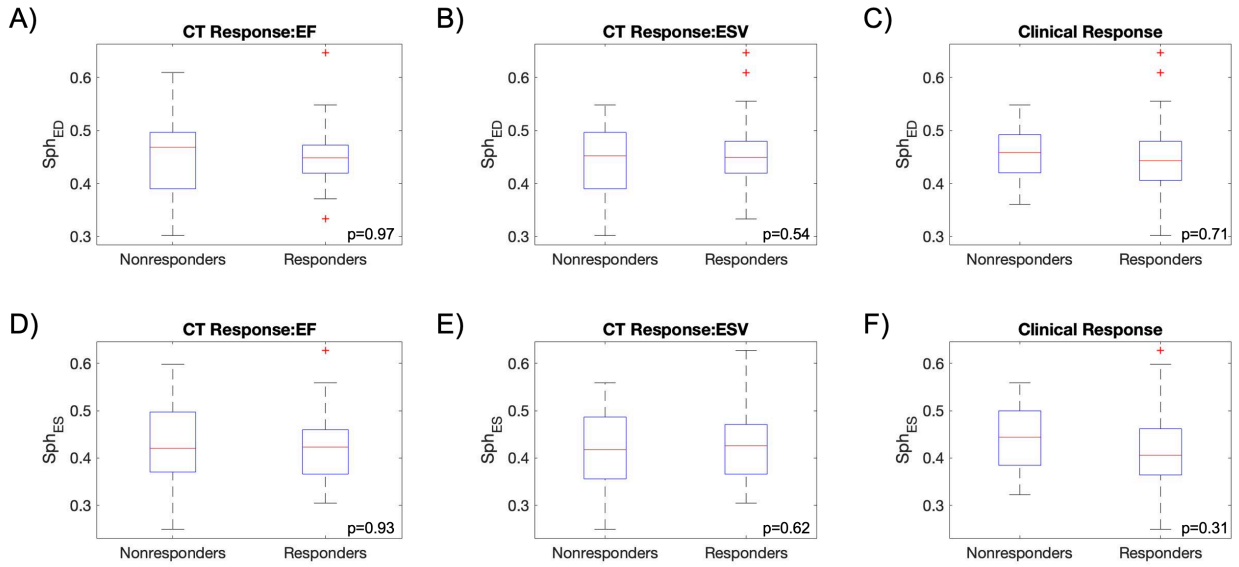

Figure 23. Boxplots displaying the distributions of 4DCT-derived endocardial sphericity at end-diastole (ED) and end-systole (ES), or Sph_{ED} and Sph_{ES}, pre CRT in responders and non-responders for the three definitions of response to CRT: (A,D) ≥5% increase in EF, (B,E) ≥15% decrease in end-systolic volume (ESV), and (C,F) clinical response defined as improvement in New York Heart Association (NYHA) class and 10% increase in the 6 min walk test, or freedom from hospitalization for heart failure or death. Two-sided t-tests were performed to evaluate differences in the distributions with a significance level set to 0.05. The resulting p-values for these tests are also shown.

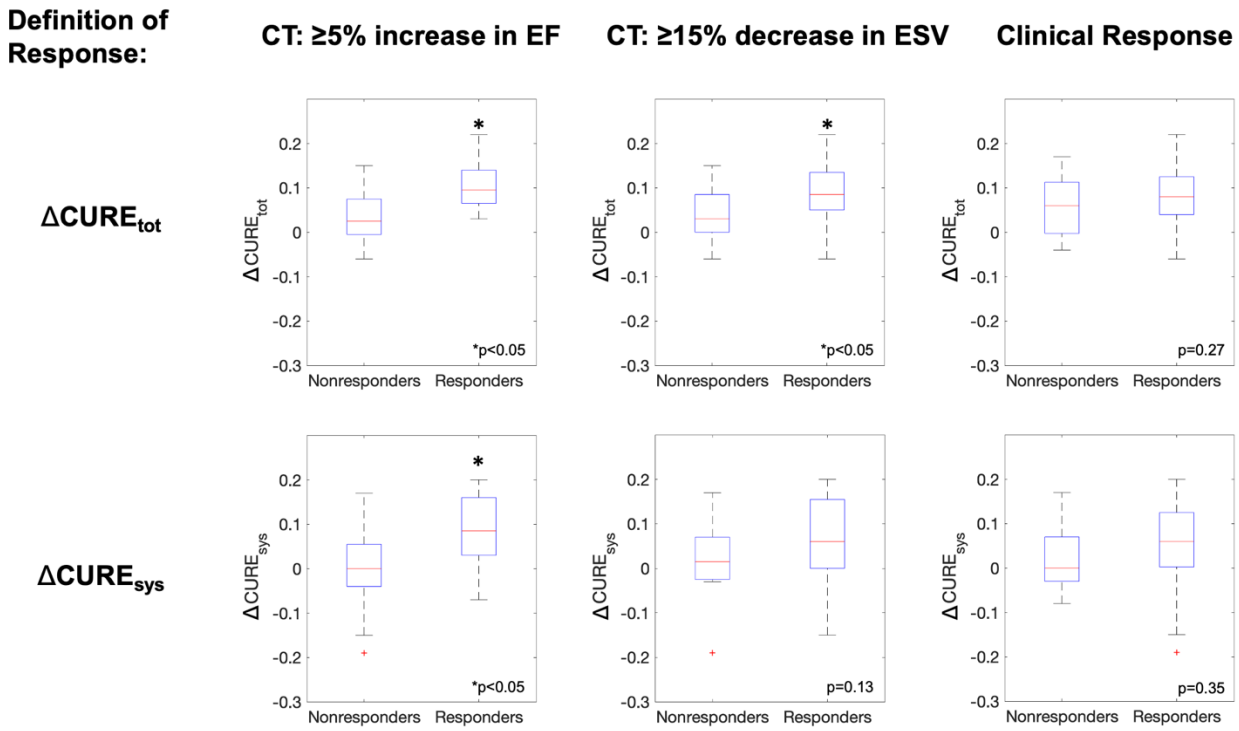

Figure 24. Changes in $CURE_{tot}$ and $CURE_{sys}$ pre and post CRT were evaluated for the three definitions of response: ≥5% increase in ejection fraction (EF), ≥15% decrease in end-systolic volume (ESV), and clinical response. Clinical response was defined as having one of the following outcomes: improvement in NYHA class and 10% increase in the 6 min walk test, or freedom from hospitalization for heart failure or death. A two-sided t-test was used to evaluate differences between the responders and non-responders with a significance level set to 0.05. Groups where a significant difference occurred are marked with an asterisk (*).

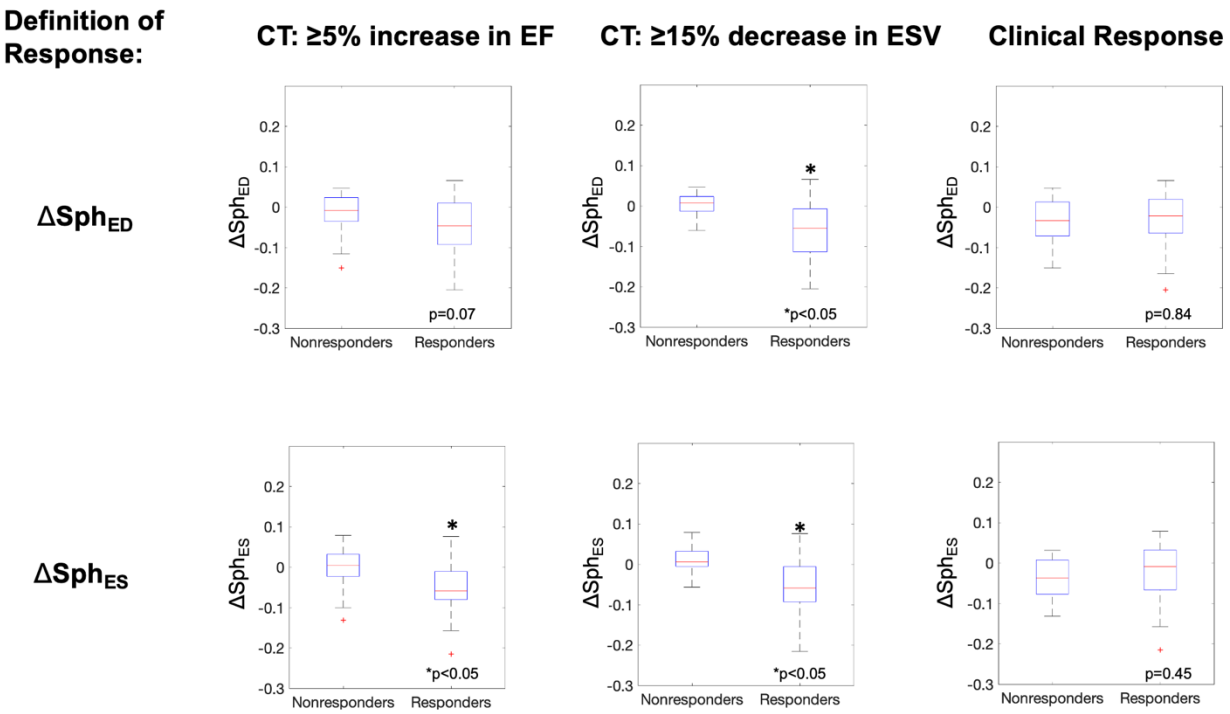

Figure 25. Changes pre and post CRT in endocardial sphericity at end-diastole (ED) and end-systole (ES), Sph_{ED} and Sph_{ES}, were evaluated for the three definitions of response: ≥5% increase in ejection fraction (EF), ≥15% decrease in end-systolic volume (ESV), and clinical response. Clinical response was defined as having one of the following outcomes: improvement in NYHA class and 10% increase in the 6 min walk test, or freedom from hospitalization for heart failure or death. A two-sided t-test was used to evaluate differences between the responders and non-responders with a significance level set to 0.05. Groups where a significant difference occurred are marked with an asterisk (*).

3.3.4 Lead placement scores for CT-based definitions of response to CRT

For both CT-based definitions of response, the 4DCT-derived predictors which produced the highest AUC and NPV were EDV, ESV, $CURE_{tot}$, $CURE_{sys}$, and TOS. The median coefficients and intercepts for both models are shown in Table 7 with the 5^{th} and 95^{th} percentile values reported as well. For the definition of response based on absolute change in EF, the median AUC from 1000 model fittings with 5-fold cross validation was 0.78 (Figure 26A). Using the median coefficients and intercept from those models, the LPS was calculated using the 44 patients and an AUC of 0.87 was achieved (Figure 26B). Using the LPS and an example threshold of 0.21, the new non-responder rate decreased from 45.5% to 17.4% (Figure 27A). Sensitivity, specificity, positive predictive value (PPV), and NPV for this given threshold are shown in Table 8.

For the definition of response based on percent change in ESV, the median AUC from 1000 model fittings with 5-fold cross validation was 0.65 (Figure 26C). Using the median coefficients and intercept from those models, the LPS generated an AUC of 0.79 (Figure 26D). Using the LPS and an example threshold of 0.20, the new non-responder rate decreased from 36.4% to 16.7% (Figure 27B). Sensitivity, specificity, PPV, and NPV for this given threshold are shown in Table 8.

Table 7. Linear discriminant analysis (LDA) with 5-fold cross validation was used to derive a lead placement score (LPS) for this cohort of 44 patients using the variables listed in the table. Models were created for both CT-based response definitions: ≥5% increase in ejection fraction (EF) and ≥15% decrease in end-systolic volume (ESV). The analysis was performed 1000 times in order to obtain confidence intervals for the coefficients and intercept. The median, 5th, and 95th percentiles of these parameters are shown for both models.

		Median Coefficient [5th, 95th percentile]	
Variable	**Units**	*CT Response: ΔEF*	*CT Response: % ΔESV*
EDV	mL	-0.057 [-0.087, -0.040]	-0.020 [-0.041, -0.003]
ESV	mL	0.052 [0.033, 0.080]	0.023 [0.003, 0.046]
$CURE_{tot}$	-	-21.2 [-41.1, -13.9]	-15.5 [-27.5, -8.18]
$CURE_{sys}$	-	12.8 [7.74, 26.5]	10.4 [5.00, 19.7]
TOS	-	7.4 [3.96, 13.6]	10.5 [7.23, 15.5]
Intercept		11.7 [7.02, 21.1]	3.96 [-0.749, 10.1]

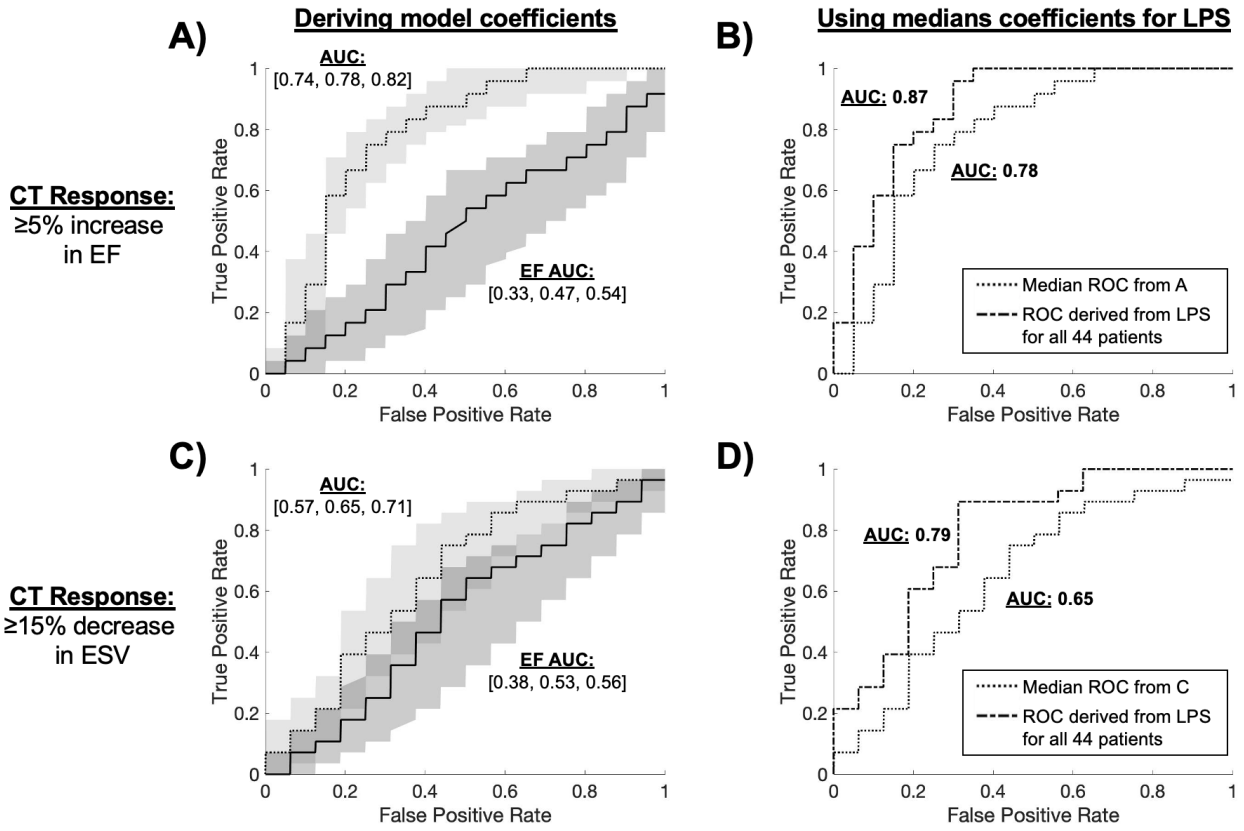

Figure 26. The median, 5th, and 95th percentile receiver operating characteristic (ROC) curves and the area under the curve (AUC) for using only ejection fraction (EF) as predictor of response are compared to the median, 5th, and 95th percentile ROC and AUC of the 1000, 5-fold cross-validated models used to derive the coefficients and intercept of the lead placement score (LPS) for predicting response. These results are shown for both CT-based definitions of response: A) ≥5% increase in ejection fraction (EF) and C) ≥15% decrease in end-systolic volume (ESV). The medians weights from A and C were used to create the LPS and evaluated in the 44 patients. These ROC curves were compared to the median ROCs shown in A and C. Performance is slightly higher for both the EF response (B) and ESV response (D) as the LPS was evaluated in the same patients used to derive the score. A separate validation cohort is needed to truly evaluate the performance of the LPS.

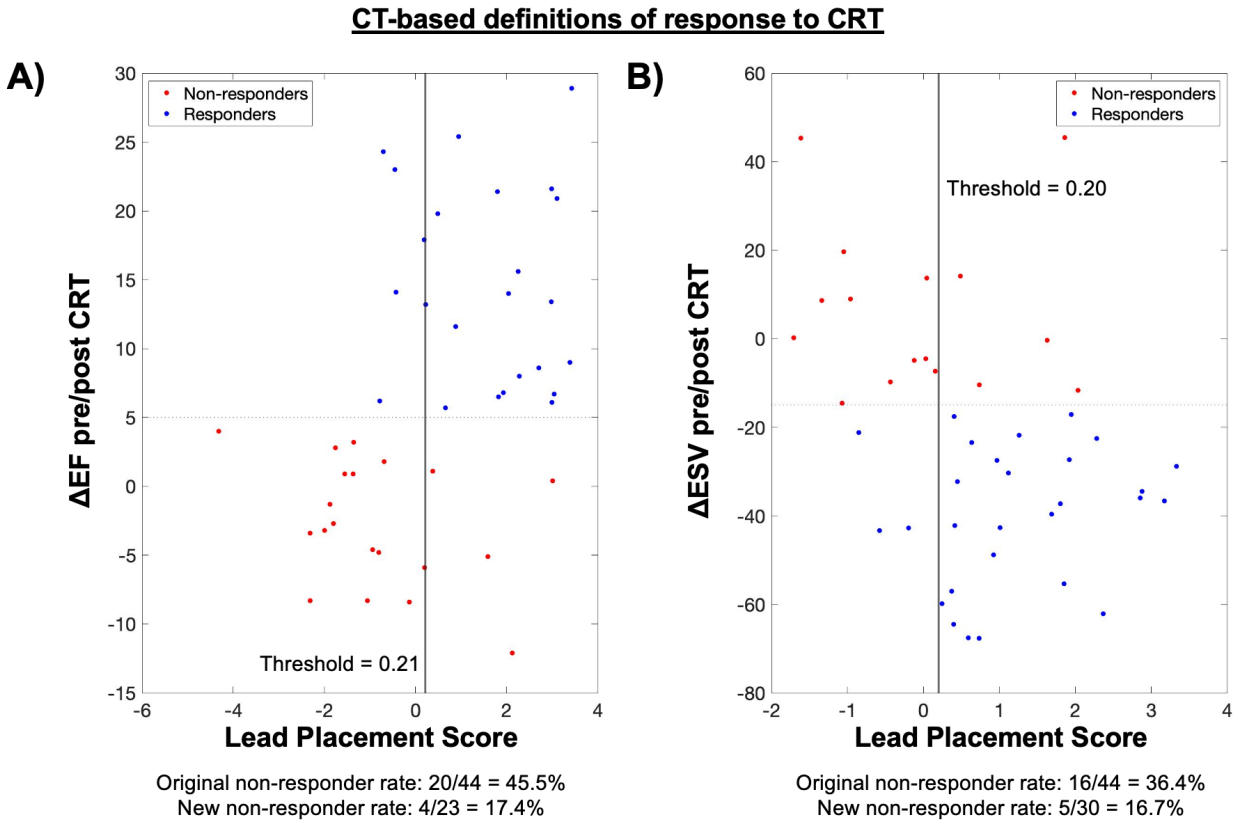

Figure 27. From the models derived using linear discriminant analysis, the median coefficients and intercept were used to create a lead placement score (LPS) for both CT-based definitions of response: A) ≥5% increase in ejection fraction (EF) and B) ≥15% decrease in end-systolic volume (ESV). LPS was then evaluated in the 44 patients and new non-responder rates were calculated. These rates were determined by the thresholds shown which determined who should undergo CRT based on the LPS.

Table 8. Prediction performance of the lead placement score (LPS) for a selected threshold for both CT-based definitions of response. The LPS, and therefore the chosen thresholds, are unitless.

	CT Response: ΔEF	***CT Response: % ΔESV***
Example Threshold for LPS	0.21	0.20
Sensitivity (%)	79.2	89.3
Specificity (%)	80.0	68.8
Positive Predictive Value (%)	82.6	86.2
Negative Predictive Value (%)	76.2	78.6

3.3.5 Lead placement score for clinical definition of response to CRT

For the clinical definition of response to CRT, the predictors which produced the highest AUC and NPV were EDV, ESV, RS_{CT}, Sph_{ED}, and Sph_{ES}. The median coefficients and intercept

for this model are shown in Table 9 with the 5th and 95th percentiles values included as well. the median AUC from 1000 model fittings with 5-fold cross validation was 0.63 (Figure 28A). Using the median coefficients and intercept from those models, the LPS was calculated using the 44 patients and an AUC of 0.79 was achieved (Figure 28B). Using the LPS and an example threshold of 0.05, the new non-responder rate decreased from 29.5% to 18.9% (Figure 28C). Sensitivity, specificity, PPV, and NPV for this given threshold are shown in Table 10.

Table 9. Linear discriminant analysis (LDA) with 5-fold cross validation was used to derive a lead placement score (LPS) for this cohort of 44 patients using the predictors listed in the table. A model was created using the clinical definition of response: improvement in NYHA class and 10% increase in the 6 min walk test, or freedom from hospitalization for heart failure or death. The analysis was performed 1000 times in order to obtain confidence intervals for the coefficients and intercept. The median, 5th, and 95th are shown for these parameters.

		Median Coefficient [5th, 95th percentile]
Variable	**Units**	*Response: Clinical*
EDV	mL	-0.044 [-0.075, -0.025]
ESV	mL	0.049 [0.026, 0.086]
RS_{CT}	-	-11.3 [-17.6, -6.63]
SphED	-	18.6 [8.69, 32.1]
SphES	-	-19.6 [-33.6, -10.6]
Intercept		1.80 [-0.965, 5.42]

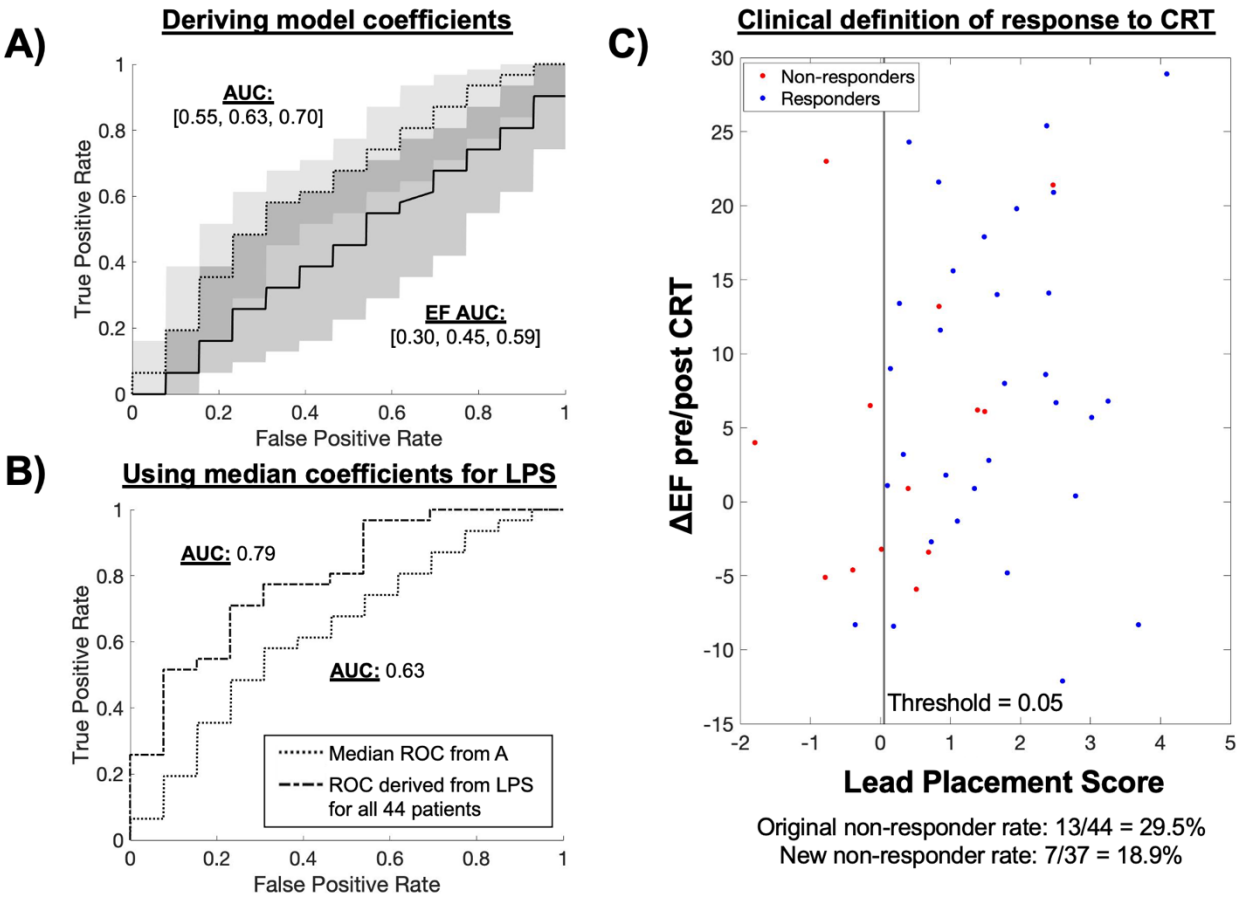

Figure 28. The median, 5th, and 95th percentile receiver operating characteristic (ROC) curves and the area under the curve (AUC) for just ejection fraction (EF) are compared to the median, 5th, and 95th percentile ROC and AUC of the 1000, 5-fold cross validated model used to derive the coefficients and intercept of the lead placement score (LPS). The results are shown for the clinical response definition: improvement in NYHA class and 10% increase in 6 min walk test, or freedom from hospitalization for heart failure or death. B) The medians weights from A were used to create the LPS and evaluated in the 44 patients. The ROC curve was compared to the median ROC shown in A. C) LPS was then evaluated in the 44 patients and a new non-responder rate was calculated. This rate was determined by the threshold shown which determined who should undergo CRT based on the LPS.

Table 10. Prediction performance of the lead placement score (LPS) for a selected threshold for the clinical definition of response to CRT.

	Clinical Response
Example Threshold for LPS	0.05
Sensitivity (%)	96.8
Specificity (%)	46.2
Positive Predictive Value (%)	81.1
Negative Predictive Value (%)	85.7

3.4 Discussion

3.4.1. Main Findings

In this chapter, we demonstrate the potential of 4DCT-derived metrics of LV shape, global and regional function, and dyssynchrony for predicting both CT- and clinically-based response to CRT through the development of the LPS. In a cohort of 44 subjects from the ImagingCRT study [42], 4DCT-derived EF, EDV, ESV, $CURE_{tot}$, $CURE_{sys}$, peak RS_{CT} near the left lead, TOS near the left lead, Sph_{ED}, and Sph_{ES} were evaluated pre and 6-months post CRT. A LPS was created for each of the three definitions of response (2 CT-based, 1 Clinical) using 5-fold cross-validated LDA. An LPS score based on a combination of LV EDV, ESV, $CURE_{tot}$, $CURE_{sys}$, and TOS measured in the pre-CRT produced the highest median AUC for predicting response based on an absolute increase in EF and precent decrease in ESV. The improvement in AUC using the LPS versus pre-EF alone was 66% for ΔEF and 23% for percent ΔESV. When the LPS was evaluated in the whole cohort using two example thresholds of 0.21 and 0.20, the original non-responder rate decreased by 62% for the ΔEF model and 54% for the percent ΔESV model. However, this decrease in the non-responder rate came with the cost of a 21% false negative rate (1-sensitivity) for ΔEF and 11% false negative rate for percent ΔESV. For the clinical definition of response, the model which included pre EDV, ESV, peak RS_{CT}, Sph_{ED}, and Sph_{ES} improved the

median AUC by 40% compared to EF alone. Using the LPS with an example threshold of 0.05, the original clinical non-responder rate decreased by 36% with a 3% false negative rate. These results are reasonably consistent with other studies that used either speckle-tracking echocardiography, cine MRI, MRI tagging, or commercially-available CT feature-tracking strain algorithms [41], [43], [45], [50], [56], [98]. Some of these studies demonstrated some benefit of quantifying LV mechanical dyssynchrony and/or scar assessment to improve CRT response; however, important differences between these studies are discussed in the next section.

3.4.2. Comparisons to other studies for image-guided LV lead placement

Results from echo-guided lead placement single- and multi-center studies have been mixed; some found poor correlation with echo-derived dyssynchrony metrics and CRT response [49], [60] while others found that echo-derived metrics provided prognostic information [41], [61]. Chung *et al.*, reported poor reproducibility in their echo-derived metrics of dyssynchrony and it is well documented that regional echo-derived measures can be highly variable [79], [99]. In our current study, we found very poor correlation between echo- and CT-derived parameters such as EDV, ESF and EF. In addition, many of the previous studies measured time to peak strain as a metric of late-activated myocardium. However, in a study by Auger *et al*., they showed using CMR cine DENSE imaging that TOS correlated better than time to peak strain with electrical activation and, in their cohort, TOS was an independent predictor of reverse LV remodeling while time to peak strain was not [43]. In this study, we used a highly reproducible method for obtaining high-resolution estimates of endocardial deformation, and subsequently TOS, for the full 3D volume of the heart across the entire cardiac cycle. Aalen *et al*., were able to obtain estimates of myocardial work using pressure-strain curves created by speckle-tracking echocardiography-derived longitudinal strain. They found that the difference in septal and lateral wall work combined with CMR late gadolinium enhancement (LGE) imaging was predictive of LV reverse remodeling (AUC=0.88) [41]. However, this method requires insertion of a catheter with a pressure gauge

into the LV. Because we do not have invasive pressure recordings for the patients involved in our study, we are not able to compare estimates of myocardial work. It is feasible that these pressure measurements could be made during device implantation and retrospectively matched with 4DCT, or invasive pressure could be made *during* the CT scan if heroic engineering development in interventional CT were to take place.

Several single-center studies have shown that CMR cine DENSE-derived CURE and TOS in combination with other parameters such as QLV, absence of scar as determined by late gadolinium enhancement (LGE) , and the Seattle Heart Failure Model SHFM-D) are associated with both an echo-based definition of response (≥15% decrease in LVESV at 6-months) and a clinical response to CRT (freedom form death, heart transplant, LV assist device, or appropriate ICD therapies) [43], [58], [59]. QLV interval is measured from the onset of the QRS wave in a surface ECG to the first major deflection recorded from an electrode stimulating the LV [100], [101]. While these results are very promising, the difficulty in obtaining high quality DENSE MR images, and the lack of open source or commercially available DENSE analysis software currently prohibits widespread clinical adoption [102]. In addition, these studies did not report results for patients with chronic RV pacing, which accounted for 21% of the patients in our study. For patients with RV pacing or an ICD system in place, CMR may be unsuitable because of significant image degradation due to metal artifacts, or the devices are not MRI-compatible. As demonstrated in our study, 4DCT can obtain estimates of LV function and dyssynchrony in these patients. In fact, 4DCT has the potential to become the robust and widely available imaging method that this field needs to assess all patients considered for CRT. 4DCT requires only a single heartbeat to acquire truly 4D images and our highly reproducible extraction and analysis of the endocardial surface does not require a skilled user to contour the myocardium, which can lead to highly variable results as seen with echo, MRI, and other CT analysis methods. With the introduction of deep learning

segmentation, our method for obtaining estimates of endocardial shape, function, and dyssynchrony will likely not require any user invention [103].

Recently, a few single-center studies have attempted to use CT for planning CRT lead placement with mixed success. Truong *et al.* showed that their CT metrics of dyssynchrony were associated with 2-year major adverse cardiac events (MACE), but not with 6-month CRT response based on their clinical composite score [57]. However, the dyssynchrony metrics reported in this study were all based on time to maximum wall thickness or inward wall motion, not time to onset. In a small, proof-of-concept, prospective study of 18 patients, Gould *et al.,* also used time to peak contraction (derived from CT endocardial contours) combined with late iodine enhancement for CT scar imaging to target the latest mechanically activated AHA segment that was free from scar. Using this method, they found that dP/dt_{max} was superior in target vs. non-target segments but still had a non-response rate of 28%. Similar results in acute response to CRT were found by Behar *et al.* [98].

The majority of previous studies discussed in this chapter evaluated the prognostic value of individual predictors or combined 2 to 3 of them. In our study, we use LDA, one of the simplest forms of machine learning, to create the LPS which best separates responders and non-responders for the given predictors. For both the clinical and CT-based definitions of response, 5 parameters in total contributed to the predictive power of the models. Yet, to reiterate, the three LPS developed in this chapter will need to be validated in a separate cohort. Thresholds for the validated LPS can then be chosen to achieve the desired sensitivity, specificity, PPV, and NPV. In this chapter we have demonstrated the choice of example LPS thresholds in our cohort, to provide new non-responder rates which were lower than the rates reported in most of the studies mentioned in this chapter, with the caveat that false negative cases were also found with that threshold. Conversely, the LPS might be able to identify patients for whom CRT is contraindicated by the prior guidelines who may actually benefit from the procedure. The trade-off between the

false negative and false positive rates will need to be evaluated by the patient and physician community. These results are very promising for 4DCT-guided LV lead placement to decrease the non-response rate of CRT.

Lastly, most of the CMR and CT studies discussed above used 2D echo-derived volumes to define a patient's response to CRT; in this study we chose to use our 4DCT-derived volumes because they were more reproducible. The original non-responder rates in the 44 patients were slightly higher for both imaging-based definitions of response (4DCT-EF: 45.5%, 4DCT-ESV: 36.4%) than the clinical definition (29.5%). This result is the opposite of what was seen in a larger subset of 155 patients from the ImagingCRT study by Fyenbo *et al.* most likely because their imaging-based definition of response was a ≥5% increase in 2D echo-derived EF [50]. In this study, we used 4DCT-derived values of EF and ESV when defining imaging-based response to CRT because of the reported poor reproducibility and underestimation of non-contrast 2D echo-derived volumes using Simpson's biplane method [104], [105]. Our method for obtaining LV volumes from 4DCT by voxel counting is contour-free, derived from the full 3D volume (potentially in a single heartbeat), and does not make assumptions about LV shape or geometry. Our 4DCT method of measuring chamber volumes is a precise estimate of the LV blood volume; whereas the echocardiography method relies on user contours of the endocardial surface and is likely an estimate of "an endocardial shell", not the precise LV blood volume. The difference between these two methods (4DCT and echo) for measuring LV function through LV volumes indicates the need for further investigation.

3.4.3. Limitations

One limitation of this study is the cohort size. Thirty-nine of 83 patients were excluded from the initial analysis because either the pre or post 4DCT scan was not analyzable. However, almost 70% of these patients were excluded because of helical step-artifacts and 18% because of poor LV blood pool-myocardium contrast. In future studies, these issues leading to poor image

quality can be avoided with single heart beat CT technology and improved protocols for timing of contrast injection [29]. In addition, while the initial results of this study indicate that these 4DCT-derived parameters have prognostic value, the example thresholds for the LPS were derived using the same cohort upon which the models were trained. Although we utilized cross-validation and the reported confidence intervals suggest stable fitting of the models, larger studies with an independent validation cohort will need to be performed to verify these results. Lastly, patient selection for the procedure can vary center-to-center and the 4DCT exams and the CRT implantation procedures in this study were performed at a single center. The success rate of the CRT procedure will be affected by the skill level and experience of each center; AUH has deep experience with CRT; therefore, leads were not placed in a "blinded" fashion. The physicians at AUH had access to both the pre-CRT 4DCT and echo studies - they explicitly avoided placing leads in areas of low myocardial function which likely significantly moved the patient cohort away from the non-responder category.

Lastly, our current method for evaluating regional endocardial shortening (RS_{CT}) does not allow for measurement of transmural deformation. Some segments with abnormally low RS_{CT} prior to CRT, which is usually associated with myocardial scar [84], saw a surprising increase in function post CRT. It is difficult to imagine any imaging method to predict this unexpected recovery; perhaps myocardial viability with FDG PET could help [106]. In future studies, combining RS_{CT} with precise measurements of ED wall thickness could improve the ability of our 4DCT methods to assess myocardial viability and prediction of response to CRT. The use of ED wall thickness was used by the AUH physicians as an indicator of the existence of infarct, but we did not include it in our LPS metric.

3.5 Acknowledgements

Chapter 3, in part, is currently being prepared for submission for publication of the material, Gabrielle M. Colvert, Ashish Manohar, Brendan T. Colvert, Zhennong Chen, Chansu Kim, James

Yang, Andrew Schluchter, Maria Ledesma-Carbayo, Anders S. Knudsen, Jens C. Nielsen, Elliot R. McVeigh. “Predicting 6-month post CRT outcomes using 4DCT-derived metrics of left ventricular shape, function, and dyssynchrony.” The dissertation author was a primary author of this paper.

Chapter 4: Novel methods for evaluation of left ventricular torsion and regional strain from 4DCT images

4.1 Introduction

4.1.1 Building on the foundations of CT SQUEEZ

We demonstrated in Chapters 2 and 3 of this work that SQUEEZ can be used to characterize the baseline state of the endocardium and subsequent changes in LV function after TMVI and CRT. However, while SQUEEZ behaves like a strain, it is not a classical myocardial strain. Therefore, we built upon the foundations of SQUEEZ to evaluate LV endocardial deformation (regional longitudinal strain, regional circumferential strain, rotation, and torsion) in the standard coordinate system of the heart which are well understood in the field of biomechanics. Being able to measure these well-characterized parameters will allow for validation of our method against the gold standard MRI tagging.

A key step in the analysis pipeline is the segmentation of the LV. Previously for SQUEEZ, this was performed on reformatted and user-cropped short axis slices. We have implemented a new segmentation process using a region-growing algorithm [85] to identify the endocardial surface which is performed in the native resolution of scanner and axial orientation. This allows us to maintain the point spread function (PSF) of the scanner and extract the most accurate representation of the endocardial surface. We also added an additional feature to the segmentation process which uses Otsu's method [86] to derive mathematically and deterministically the threshold used for segmentation. This removes user-variability in selecting this parameter and allows for the same high-resolution endocardial surface to be extracted every time.

In addition, the SQUEEZ algorithm relied on low aspect ratio and low skewness mesh faces to obtain physiologic measurements; this required downsampling and smoothing of the data. These processes did not affect the accuracy of SQUEEZ in initial studies because the

endocardium of the animal hearts was smooth with large features. However, a human LV has significantly more trabeculation yielding a very complex endocardial surface with smaller features. This complex texture provides a high density of fiducial markers which permit and have the potential to enhance the accuracy of nonrigid registration. Our new algorithms for measuring standard strains do not rely on individual mesh faces but on the “cloud” of endocardial points alone, allowing higher resolution analysis. Analysis of LV strain has often been restricted to a global value, such as GLS, or values depicted in the relatively low resolution AHA 17 segment model [107]. This limitation exists because other modalities have significantly lower spatial resolution than 4DCT. Performing our analysis on high resolution point clouds permits quantification of regional strain with variable patch sizes which will be crucial for analyzing human LVs with abnormal geometry and function, such as dyssynchrony and wall motion abnormalities, as seen in patients with mitral regurgitation.

4.1.2 Limitations of other methods for measuring LV strain using CT

Although other methods exist to measure myocardial strains from 4DCT, they are based on image registration techniques that rely on *a priori* mechanical models to guide the registration or feature tracking algorithms within the myocardium where fiducial markers are sparse [108]–[110]. Although our method does not currently permit measurement of transmural deformation, our approach takes advantage of the region of the CT volume where the greatest contrast and quantity of fiducial markers exists: the boundary between the endocardium and the contrast-enhanced blood pool. Extraction of the blood pool boundary from 4DCT and the computation of endocardial deformation from points on that boundary have been shown to be highly reproducible [77], [90]. In addition, by segmenting all timeframes and using the registration method to solve for point-to-point correspondence, we detach our metrics from model-based analysis which may be inadequate when identifying and characterizing severely abnormal cardiac shape and function. Our newly developed algorithms for measuring standard metrics of cardiac function from 4DCT

volumes can analyze the deformation of the LV with no assumptions made about function or geometry.

4.2 Materials and Methods

4.2.1 Obtaining 3D endocardial displacement fields from 4DCT images

In order to measure endocardial deformation, the LV blood pool was segmented from all timeframes through the RR interval in 3D using a region-growing algorithm in ITK-snap (ver. 3.6.2) [85]. The segmentation threshold was derived from a region-of-interest within a mid-axial slice containing the blood pool and the myocardium at end-diastole (ED) using Otsu's method [86]. From the surface of the LV blood pool segmentation volume, a point cloud was extracted using MATLAB's built-in function *isosurface* (2018b, Mathworks, Natick, MA). Then, a nonrigid registration algorithm called Coherent Point Drift (CPD) [89] was used to solve for the 3D displacement fields between ED and each later timeframe within the cardiac cycle. The complete pipeline for obtaining these displacement fields from 4DCT data is summarized in Figure 29. These methods have been utilized, validated, and optimized previously to obtain 3D endocardial deformation fields for evaluating regional and global cardiac function [77], [78], [84], [111], [112].

Once registration was complete, the point clouds were rotated from the axial position so that the z-axis aligned with the long axis (LAX) of the LV. The user identified the LAX by selecting the apex and base of the LV in the ED volume. After this rotation, standard metrics of LV endocardial function, namely apical rotation, basal rotation, torsion, regional longitudinal strain, and regional circumferential strain, were derived from the 3D displacement fields.

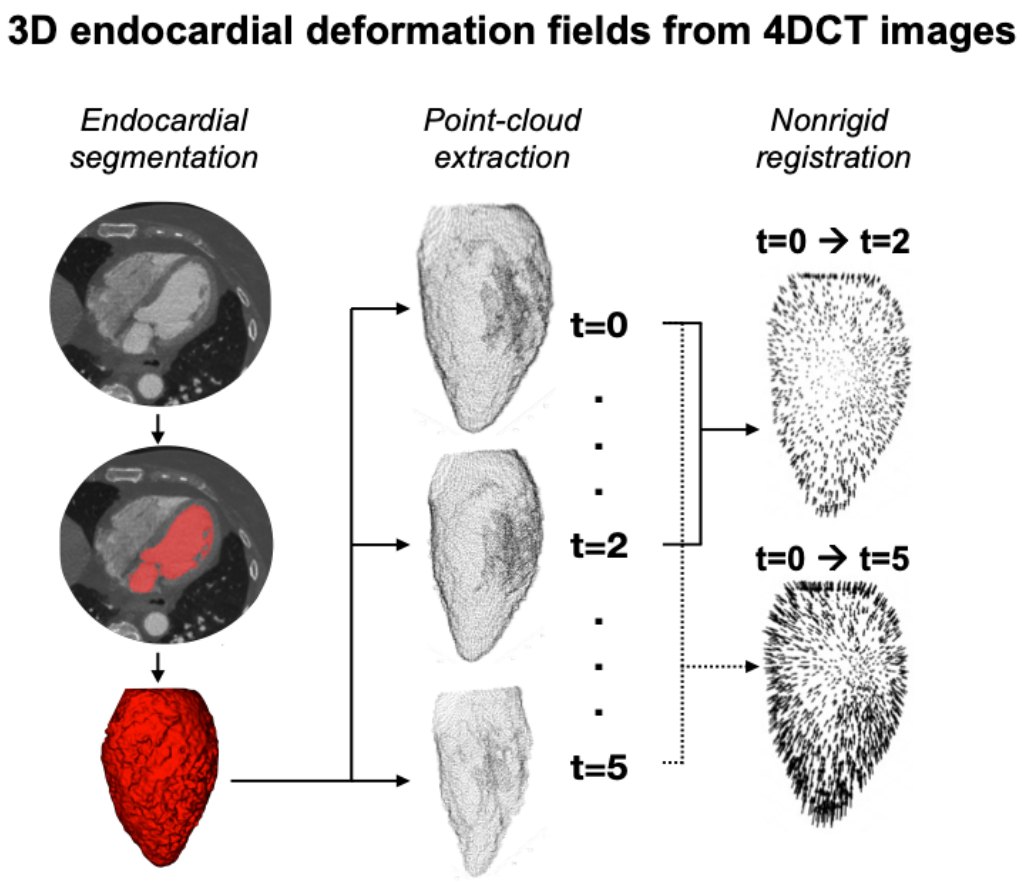

Figure 29. 3D displacement fields are derived from 4DCT images in 3 steps: 1) left ventricular blood pool segmentation in 3D, 2) point-cloud extraction of the endocardial surface, and 3) nonrigid registration of that surface over the R-R interval.

4.2.2 Endocardial rotation and torsion from 4DCT-derived displacement fields

Endocardial rotation and torsion about the long axis of the LV were measured from the registered point clouds in Cartesian coordinates [87], [112]. The template point cloud, or reference timeframe, was divided into 1-millimeter thick 2D short axis slices based on the z-position of the points. Corresponding slices were found at all other timeframes using the registered point clouds containing point-to-point correspondences with the template. Maximum likelihood (ML) estimation was used to solve for the rotation angle of each 2D slice, s, by modeling the motion of the points within that slice as an affine transformation as follows.

The set of reference points was denoted $\mathbf{X} \in \mathbb{R}^{2xn}$, where n is the number of points in the 2D slice. The reference timeframe was always chosen to be ED. The motion of $\mathbf{X}$ was modeled as the affine transformation

$$\boldsymbol{\mathcal{Y}} = \mathbf{AX} + \mathbf{b} + \boldsymbol{\mathcal{R}}, \tag{4.1}$$

where $\mathbf{A} \in \mathbb{R}^{2x2}$ is the transformation matrix, $\mathbf{b} \in \mathbb{R}^2$ is the translation vector, $\boldsymbol{\mathcal{R}} \in \mathbb{R}^2$ is the residual, and $\boldsymbol{\mathcal{Y}} \in \mathbb{R}^{2xn}$ is the result of the motion. The components of $\mathbf{A}$ and $\mathbf{b}$ were defined as

$$\mathbf{A} = \begin{bmatrix} a_{11} & a_{12} \\ a_{21} & a_{22} \end{bmatrix} \text{ and } \mathbf{b} = \begin{bmatrix} b_1 \\ b_2 \end{bmatrix}. \tag{4.2}$$

It was assumed that the residual is a normally distributed random variable with zero mean and isotropic variance

$$p_{\boldsymbol{\mathcal{R}}}(\boldsymbol{r}) = \frac{1}{\sqrt{(2\pi)^2|\Sigma|}} \exp\left(-\frac{1}{2}\boldsymbol{r}^T\boldsymbol{\Sigma}^{-1}\boldsymbol{r}\right), \tag{4.3}$$

where $\boldsymbol{\Sigma}$ is the covariance matrix and defined as

$$\boldsymbol{\Sigma} = \sigma\mathbf{I} = \begin{bmatrix} \sigma & 0 \\ 0 & \sigma \end{bmatrix}. \tag{4.4}$$

The random variable $\boldsymbol{\mathcal{Y}}$ followed the same distribution function with a shifted mean $\boldsymbol{\mu} = \mathbf{AX} + \mathbf{b}$, therefore

$$p_{\boldsymbol{\mathcal{Y}}}(\boldsymbol{y}) = \frac{1}{\sqrt{(2\pi)^2|\Sigma|}} \exp\left(-\frac{1}{2}(\mathbf{y} - \mathbf{Ax} - \mathbf{b})^T\boldsymbol{\Sigma}^{-1}(\mathbf{y} - \mathbf{Ax} - \mathbf{b})\right). \tag{4.5}$$

A parameter vector was defined as $\boldsymbol{\eta} = [a_{11}\ a_{12}\ a_{21}\ a_{22}\ b_1\ \ b_2\ \sigma]^{\mathrm{T}}$. The likelihood function for a given data point $\{\mathbf{x}_n, \mathbf{y}_n\}$ is called $\mathcal{L}(\eta|\{\mathbf{x}_n, \mathbf{y}_n\})$ and was found by evaluating the distribution at that data point

$$\mathcal{L}(\boldsymbol{\eta}|\{\mathbf{x}_n, \mathbf{y}_n\}) = p(\mathbf{x}_n, \mathbf{y}_n|\boldsymbol{\eta}). \tag{4.6}$$

The likelihood function for the entire 2D slice was given by

$$\mathcal{L} = \prod_{n} \mathcal{L}_n \,. \tag{4.7}$$

The negative log likelihood was then defined as

$$NLL = -\log(\mathcal{L}) = -\sum_{n} \log(\mathcal{L}_n) \,. \tag{4.8}$$

In order to find the maximum likelihood estimate η^*, NLL was minimized

$$\boldsymbol{\eta}^* = \underset{\boldsymbol{\eta}}{\operatorname{argmin}}\, NLL(\boldsymbol{\eta}) \,. \tag{4.9}$$

The minimization of *NLL* in order to find the maximum likelihood estimate for $\boldsymbol{\eta}$ was performed using MATLAB's built-in nonlinear solver *fmincon.* The initial conditions for each of the parameters were

$$\boldsymbol{A}_0 = \begin{bmatrix} 1 & 0 \\ 0 & 1 \end{bmatrix}, \boldsymbol{b}_0 = \begin{bmatrix} 0 \\ 0 \end{bmatrix}, \text{and } \sigma_0 = 1000, \tag{4.10}$$

which assumed zero scaling, shear, rotation, and translation. Because of this, σ_0 was initialized to a large enough value to account for the variability in point position within the slice. Lastly, an additional constraint was added to ensure σ was non-negative.

Once ML estimation was used to solve for unknown parameters $\mathbf{A}$, $\mathbf{b}$, and σ for slice s, $\mathbf{A} = \mathbf{RU}$ was decomposed into a stretch tensor $\mathbf{U}$ and rotation matrix

$$\mathbf{R} = \begin{bmatrix} \mathrm{R}_{11} & \mathrm{R}_{12} \\ \mathrm{R}_{21} & \mathrm{R}_{22} \end{bmatrix}. \tag{4.11}$$

The rotation angle was then defined as

$$\theta^{(s)} = \tan^{-1}\left(\frac{\mathrm{R}_{12}}{\mathrm{R}_{11}}\right) \tag{4.12}$$

as shown in Figure 30A. This definition of the rotation angle for a single slice follows the clinical convention that the counterclockwise rotation (as viewed from the apex toward the base) is a

positive angle while the clockwise rotation is negative [113]. In normal hearts, the apex rotates counterclockwise during systole, and the base has a net clockwise rotation. In a normalized coordinate system aligned with the long axis, the apical and basal slices were defined as percentages of the LV, where the apical tip of the endocardium is 0% and the mitral valve plane is 100%. LV twist was derived by subtracting the rotation of the apical slice from the rotation of the basal slice and LV torsion was defined as LV twist divided by the distance between the apical and basal slices.

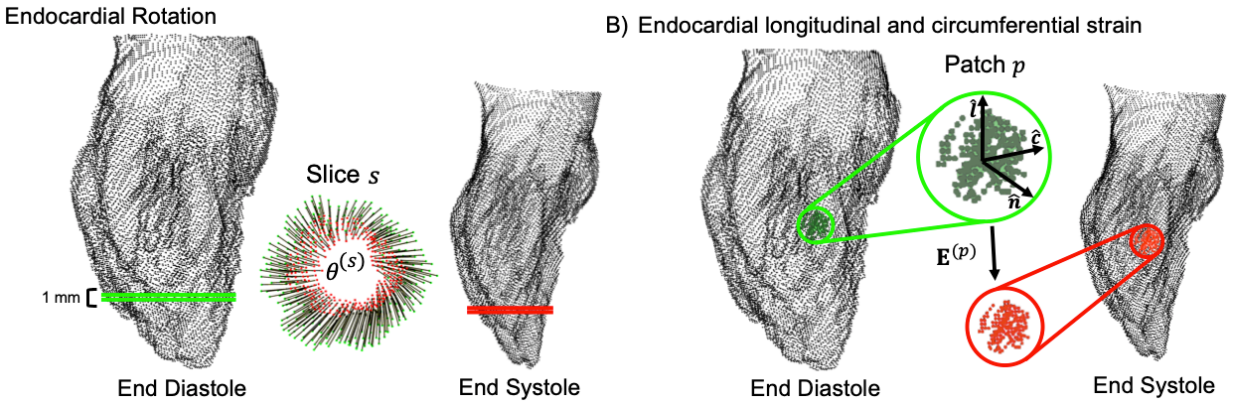

Figure 30. A) An example slice, s, near the apex of the left ventricle which shows the displacement between end diastole (ED) and end systole (ES) from which the rotation angle, θ_s, was derived. B) An example patch at ED and ES from which the strain tensor was derived. The standard cardiac coordinate system was calculated based on the normal vector, $\hat{n}$, which defines the plane tangent to the patch at ED.

4.2.3 Regional endocardial strain from 4DCT-derived displacement fields

In order to measure regional endocardial strain, 15% of points within the template point cloud (ED) were randomly sampled to be centers of a set of circular patches covering the LV. All points within a given radius of the center point were extracted. A connectivity matrix was computed for the template point cloud using the faces computed by *isosurface*. To eliminate points from the patch that were on surfaces adjacent to the endocardium, such as the papillary muscles, a graph was created. This allowed distances to be computed *along the surface* of the ventricle instead of 3D Euclidean distances. Points were excluded from the patch if their "graph distance" indicated they did not lie on the endocardial surface. An associated set of deformed patches was computed

at all other timeframes using the point-to-point correspondences determined by registration. Then, similar to the algorithm described in 4.2.2, an affine transformation was fit to the 3D motion of all points within patch, p, using ML estimation to solve for the unknown parameters $\mathbf{A}$, $\mathbf{b}$, and σ. However, for this analysis, the motion model involved a 3x3 affine transformation matrix to describe the deformation. The Green strain tensor for each patch was derived from the affine transformation matrix and defined as

$$\mathbf{E} = \frac{1}{2}(\boldsymbol{A}'\boldsymbol{A} - \mathbf{I}) \tag{4.13}$$

To assess longitudinal and circumferential strain, $\mathbf{E}$ was rotated into the standard coordinate system of the heart. Because the analysis involves a 2D surface in 3D space, radial strain cannot be computed with the current method. Using the same center points as for the strain calculation, a patch with a 15 mm radius was used to define the local surface topography. This larger radius was chosen to obtain a more stable estimate of the tangent plane to the surface due to the natural roughness of the endocardial surface. MATLAB's *pca* function was used to compute the normal vector which defined the tangent plane. The circumferential vector was found as that vector that is perpendicular to the normal vector and has zero z-component. The longitudinal vector was defined as the unit vector orthogonal to the normal and circumferential vectors and was computed by taking their cross product. The strain tensor was rotated into the standard orientation by applying the 3D transformation defined by the computed unit vectors yielding longitudinal, $\mathrm{E}_{ll}^{\mathrm{CT}}$, and circumferential, $\mathrm{E}_{cc}^{\mathrm{CT}}$, strain as principal strains for each patch as shown in Figure 30B.

The computed strains were assigned to the point at the patch center. These sampled strains were interpolated to all points in the original point cloud using MATLAB's built-in *scatteredInterpolant* function and smoothed with a Gaussian filter with a width of the same size

as the original patch radius. This was done to obtain strain maps on the endocardial surface with a resolution consistent with the original patch size used to estimate the regional deformation.

4.3 Acknowledgments

Chapter 4, in part, is a reprint of the material as it is published in: Gabrielle M. Colvert, Juan E. Ortuño, W. Patricia Bandettini, Marcus Y. Chen, Maria J. Ledesma-Carbay, Elliot R. McVeigh. “4DCT-derived Endocardial Left Ventricular Torsion Correlated with CMR Tagging-derived Torsion in the Same Subjects.” in JACC: Cardiovascular Imaging (2020). The dissertation author was a primary author of this paper.

Chapter 4, in part, is a reprint of the material as it is published in: Gabrielle M. Colvert, Ashish Manohar, Brendan T. Colvert, Andrew Schluchter, Francisco J. Contijoch, Elliot R. McVeigh. “Novel measurement of LV twist using 4DCT: quantifying accuracy as a function of image noise.” in Proc. SPIE 10953, Medical Imaging 2019: Biomedical Applications in Molecular, Structural, and Functional Imaging. The dissertation author was a primary author of this paper.

Chapter 4, in part, has currently been submitted for publication of the material, Gabrielle M. Colvert, Ashish Manohar, Brendan T. Colvert, Juan E. Ortuño, Zhennong Chen, James Yang, W. Patricia Bandettini, Marcus Y. Chen, Maria J. Ledesma-Carbayo, Elliot R. McVeigh. “Regional left ventricular endocardial strain from 3D deformations fields derived from 4DCT images.” The dissertation author was a primary author of this paper.

Chapter 5: Evaluating accuracy and precision of novel 4DCT-derived metrics of left ventricular function with phantom experiments

5.1 Introduction

Herein, we conducted phantom experiments to validate the novel methods proposed in chapter 4 for measuring endocardial LV rotation, torsion, and standard cardiac strains (longitudinal E_{ll}^{CT} and circumferential E_{cc}^{CT}) from 4DCT using point cloud registration and ML estimation. First, the accuracy of these methods is evaluated in a simulated clinical setting using a 3D-printed human LV endocardial phantom. The phantom is imaged under different conditions to test the performance of the algorithm with varying levels of image quality. Then, the precision and reproducibility of the proposed algorithm is estimated by imaging the phantom multiple times under the same scanning condition.

5.2 Materials and Methods

5.2.1 Left ventricular endocardial phantom with known physiologic displacements

In order to evaluate the accuracy and precision of the proposed methods, we used an analytical phantom with known physiologic displacements. This phantom was previously developed by Manohar *et al*. to optimize the non-rigid registration method we use to obtain the displacement field of the endocardial surface of a human LV [114]. This *in silico* phantom was created from the end-diastolic phase of a clinical 4DCT scan of a healthy heart with normal cardiac function [114]. The LV blood pool was first segmented using the region-growing algorithm in ITK-snap [85]. Then, the segmentation was resampled to an isotropic resolution of 0.5 mm^3 voxels and rotated such that the LV long axis coincided with the z axis. A point cloud representing the endocardial surface was extracted from the binary segmentation and displacements were applied to the points based on literature-derived values of endocardial longitudinal and circumferential strain and rotation [115]–[117]. These deformations resulted in an end-systolic pose of the LV with an ejection fraction of 70% which was consistent with CT-based EFs measured in normal

human hearts [77]. The programmed ground truth values for LV rotation, longitudinal strain, and circumferential strain are shown in Figure 31.

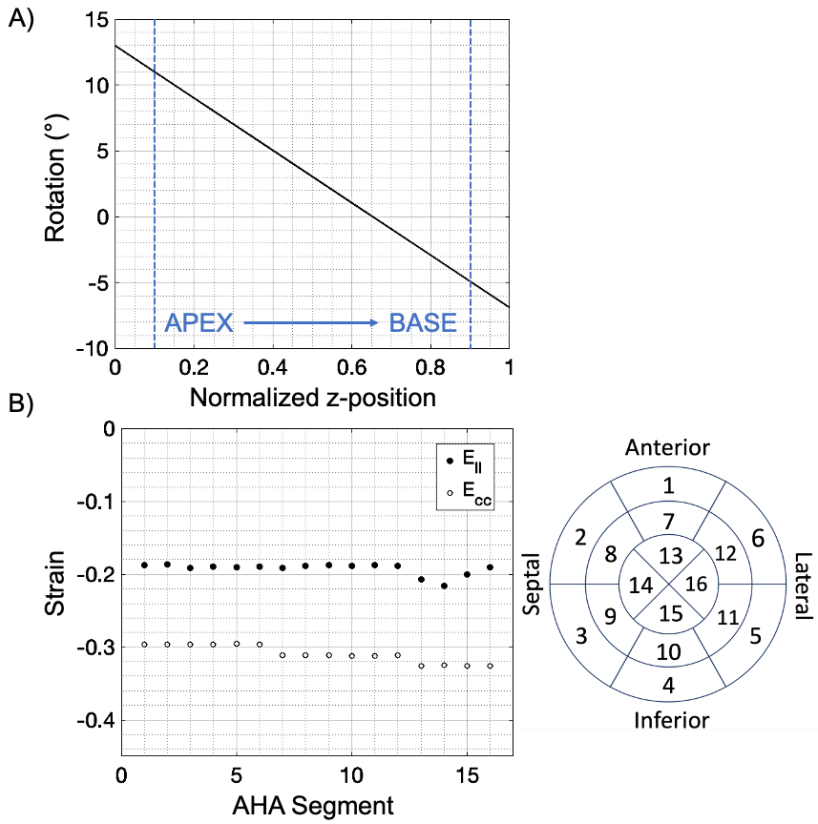

Figure 31. A) The rotation angle as a function of normalized position along the long axis of the left ventricle from the apex (z = 0.1) to the base (z = 0.9). B) Regional longitudinal (E_{ll}) and circumferential (E_{cc}) strain for the 16 American Heart Association (AHA) segments where the outermost ring is composed of the basal segments and the innermost of the apical segments [107].

5.2.2 Imaging 3D-printed endocardial phantom to evaluate accuracy and precision

The end-diastolic (ED) and end-systolic (ES) phases of the analytical phantom were 3D-printed to test the accuracy and precision of measuring endocardial rotation, E_{ll}^{CT}, and E_{cc}^{CT} from CT images in the presence of image noise and spatial resolution generated by clinical cardiac CTA protocols and image reconstruction. The phantoms were printed using a Form 2 stereolithography system with a clear photopolymer resin (Formlabs Inc., Somerville, MA). A stand was also 3D-printed so that both ED and ES could be locked into place and ensure the two phases were in the correct orientation while the phantoms were being scanned.

The segmentation of the contrast-enhanced blood pool and subsequent extraction of the endocardial surface with features required for accurate point cloud registration is dependent on the contrast between the LV blood pool and the myocardium. Therefore, the ED and ES phases of the phantom were imaged with decreasing x-ray tube current levels and a tissue equivalent "extension ring" (Extension-Ring-Tissue (L, H200), QRM GmbH, Moehrendorf, Germany). The extension ring mimics the abdominal tissue in order to decrease the detected x-ray fluence, increase image noise, and reduce the contrast-to-noise (CNR) ratio between these two regions. The two 3D-printed phantoms and the stand inside the extension ring are shown in Figure 32. All images were obtained on a Revolution CT scanner (GE Medical Systems, Wisconsin) using a small focal spot, cardiac field-of-view (20 cm), pixel spacing of 0.39 mm x 0.39 mm x 0.625 mm, and a tube voltage of 100 kVp. To quantify image noise, CNR was computed as

$$\mathrm{CNR} = \frac{\mu_{LV} - \mu_{myo}}{\sigma_{myo}} \tag{5.1}$$

where μ_{LV} is the mean signal in Hounsfield Units within the LV, μ_{myo} is the mean signal within the "myocardium" (which is actually polymer resin), and σ_{myo} is the standard deviation of the signal within the "myocardium". To demonstrate the effect of the reconstruction protocol on the spatial resolution of the images, σ_{myo} was also reported.

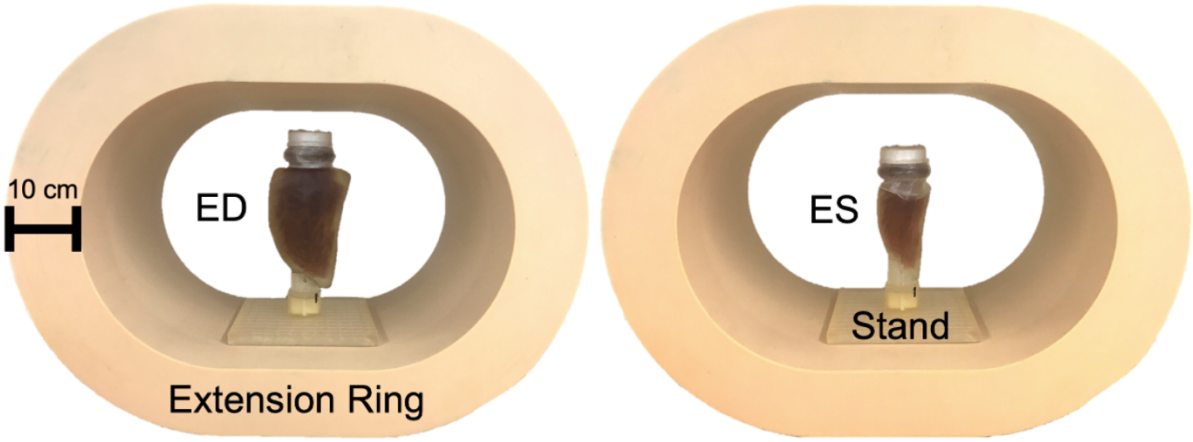

Figure 32. The end-diastolic (ED) and end-systolic (ES) 3D-printed phantoms are shown inside the tissue equivalent “extension ring” which is 10 cm thick. Both phases of the phantom are locked into the correct orientation with the stand. The inside chamber of the phantom is filled with 10%, 5%, and 2.5% iodine contrast in water to represent the LV blood pool. Red dye was added for visualization of the water-iodine mixture inside the phantom.

5.2.3 Quantifying accuracy of proposed 4DCT algorithms with 3D-printed phantom

To quantify the accuracy of the proposed algorithms, we evaluated their performance under 7 different scanning conditions which resulted in a wide range of noise levels and spatial resolutions. The standard clinical reconstruction parameters were used for all 7 experiments with ASIRV = 50% and the “Standard” filter kernel. For the first 5 scans, the chamber was filled with x-ray contrast agent (Visipaque (iodixanol) 320mg Iodine/mL) diluted to 10% in water to mimic typical LV enhancement seen in clinical scans. The two phases of the 3D-printed phantom were first scanned at 450 mA with no extension ring to obtain the highest CNR image. This represented an optimal imaging scenario with minimal amount of noise. All other experiments (#’s 2-7) included the extension ring. The mA was decreased by about 50% after each experiment in order to observe degradation of image quality. In order to further lower CNR values, the contrast agent was diluted to 5 and 2.5% in water for experiments 6 and 7, respectively. The scanning parameters for each experiment are summarized in the first column of Table 11.

Table 11. Seven different experiments were conducted to evaluate the accuracy of the proposed 4DCT methods as a function of image quality. The standard clinical CTA protocol was used for reconstruction of the images ("Standard" reconstruction kernel & ASIRV=50%). An extension ring was also used to increase the attenuation of x-rays and simulate the body cavity. Lastly, three different concentrations of the contrast agent in water were used, 10%, 5%, and 2.5%, where 10% is the typical concentration used in a clinical 4DCT scan. The contrast-to-noise ratio (CNR) between the LV blood pool and the myocardium (photopolymer resin of the phantom) was computed for the 7 different scanning scenarios.

	Scanning and Reconstruction Parameters	**Image Quality**	
	Standard Clinical Reconstruction (ASIRV=50%, Standard Kernel)	LV-myo CNR	σ_{myo} (HU)
1	450 mA, no Ext. Ring, 10% Iodine	70.1	10.7
2	450 mA, with Ext. Ring, 10% Iodine	40.1	17.3
3	225 mA, with Ext. Ring, 10% Iodine	27.7	25.2
4	110 mA, with Ext. Ring, 10% Iodine	22.1	31.6
5	50 mA, with Ext. Ring, 10% Iodine	18.7	36.5
6	50 mA, with Ext. Ring, 5% Iodine	8.6	39.7
7	50 mA, with Ext. Ring, 2.5% Iodine	2.7	41.4

The proposed 4DCT algorithms were used to calculate endocardial rotation, LV twist and torsion, $\mathrm{E}_{ll}^{\mathrm{CT}}$, $\mathrm{E}_{cc}^{\mathrm{CT}}$, global circumferential strain (GLS), and global circumferential strain (GCS) under variable CNR and spatial resolution conditions provided by the different imaging protocols. For rotation, in a normalized coordinate system aligned with the long axis, the apical and basal slices were defined at 10% and 90% of the LV, respectively. These positions were chosen based on initial results from these phantom experiments which indicated lower accuracy in rotation measurement at the extreme ends of the ventricle. For strain, a patch size with radius of 5 mm was used. The absolute error for all metrics was defined as

$$\Delta x = x^{meas} - x^{GT} \tag{5.2}$$

where x^{meas} is the measured parameter and x^{GT} is the ground truth value. For strain, an average value was computed for each of the 16 American Heart Association (AHA) segments [107] and compared to the ground truth values for those segments. Global strains were obtained by computing the average strain for the 16 segments.

5.2.4 Quantifying precision of proposed 4DCT algorithms with 3D-printed phantom

To estimate the precision of the proposed algorithms, the 3D-printed ED and ES phases were imaged 10 times each using the same scanning parameters as experiment 6 in section 5.2.3. The 2 phantoms were scanned multiple times to achieve independent noise for all 20 volumes acquired. The set of scanning parameters were chosen because they were at the lower limits of CNR, and spatial resolution seen in clinical datasets acquired at our institution for monitoring chemotherapy patients. Endocardial rotation, LV twist and torsion, $\mathrm{E}_{ll}^{\mathrm{CT}}$, $\mathrm{E}_{cc}^{\mathrm{CT}}$, GLS, and GCS were all measured from the 10 datasets as described previously and a mean and standard deviation were calculated for each of the parameters and compared to the ground truth.

5.3 Results

The ED and ES phases of the 3D-printed phantom were scanned and reconstructed for the 7 different image quality conditions. The CNRs were calculated for each of the experiments and are listed in Table 1. Overall, the CNR decreased as the x-ray fluence decreased; however, at the lower x-ray tube currents under the standard clinical reconstruction protocols, the reduction in CNR does not decrease as the square root of mA. This phenomenon is likely due to proprietary adaptive “low signal conditioning” of the raw data and the iterative reconstruction method with the ASIRV = 50%. The smoothing effect of the low tube-current on the spatial resolution can be observed through the plateau in σ_{myo} vs decreasing CNR in experiments 4-7 in Table 1. The lowest CNR achieved was 2.7 at 50 mA with the extension ring, and 2.5% iodine in water. After these parameters were computed, endocardial rotation, longitudinal, and circumferential strain were measured using the proposed algorithms.

5.3.1 Accuracy of proposed algorithms under various scanning conditions

After the 3D-printed phantoms were scanned and the images reconstructed, endocardial rotation was measured for each short axis slice according to the algorithm described in 4.2.2. Figure 33 shows the measured vs. ground truth rotation values per slice for 3 of the 7 experiments

representing the highest (450 mA, ext. ring, 10% iodine CNR = 40.1), average (50 mA, ext. ring, 5% iodine, CNR = 8.6), and lowest (50 mA, ext. ring, 2.5% iodine, CNR = 2.7) CNR values seen clinically. Overall, the algorithm was able to capture the programmed rotation of the phantom for all image quality conditions. Table 12 summarizes the absolute errors for LV twist and torsion. For reference, the ground truth LV twist from the apex to the base was 15.8° and torsion was -2.26°/cm. For LV twist, the errors for all cases were less than 2.1°, except for the lowest CNR condition where the error was higher at 3.28°. For torsion, all errors were less than 0.28°/cm.

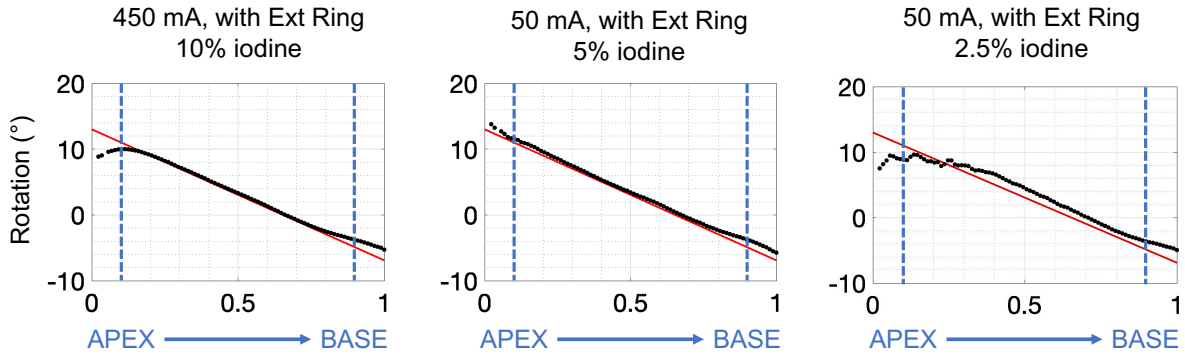

Figure 33. Measured rotation angle and the ground truth values as a function of slice position for 3 of the 7 3D-printed phantom experiments reconstructed with the “Standard” kernel. The blue lines represent the apex (10% of the LV) and the base (90% of the LV). 450 mA with the extension ring (left) had the highest clinically-relevant CNR (40.1), 50 mA with the extension ring and 5% iodine (middle) resulted in a CNR (8.6) similar to the average of clinical scans, and 50 mA with the extension ring and 2.5% iodine (right) had a CNR (2.7) lower than most clinical scans.

Table 12. Absolute errors are shown for both LV twist and LV torsion. For reference, ground truth LV twist is 15.8° and torsion is -2.26° /cm. Absolute error between measured and ground truth strain for the global longitudinal strain (GLS) and global circumferential strain (GCS) is also shown. The ground truth values for GLS and GCS are -0.192 and -0.309, respectively. The maximum error for the regional strains is displayed as well. *no extension ring

	Parameters		**Absolute Error (Measured-Ground Truth)**					
	mA	% Iodine	LV twist Error (°)	LV torsion Error (°/cm)	GLS Error	$\boldsymbol{E_{ll}^{CT}}$ Max Error	GCS Error	$\boldsymbol{E_{cc}^{CT}}$ Max Error
1	450 mA*	10	0.30	0.07	-0.003	-0.035	0.007	0.016
2	450 mA	10	-2.06	-0.11	-0.004	-0.019	0.007	0.026
3	225 mA	10	-1.00	-0.27	-0.005	-0.060	0.007	0.026
4	110 mA	10	-1.64	-0.20	-0.001	-0.023	0.007	0.036
5	50 mA	10	-1.09	-0.07	-0.002	-0.021	0.008	0.026
6	50 mA	5	-0.62	-0.03	0.002	-0.036	0.005	0.043
7	50 mA	2.5	-3.38	-0.27	0.001	0.078	-0.004	0.036

E_{ll}^{CT} and E_{cc}^{CT} were also measured for the 7 different image quality conditions and compared to the ground truth values for the 16 AHA segments. Figure 34 shows the results for the same 3 of the 7 experiments shown in Figure 33. This figure indicates that the proposed algorithm for measuring endocardial longitudinal and circumferential strain was able to accurately capture the programmed ground truth deformation of the 3D-printed phantom. For the first 6 cases, the absolute errors were less than 0.06 (6% strain) for all 16 segments. For the lowest CNR condition (experiment #7), the absolute errors were all less than 0.08 (8% strain). The absolute errors from the measurement of GLS, GCS, E_{ll}^{CT} and, E_{cc}^{CT} for all CNR conditions are summarized in Table 12. For reference, the ground truth values for GLS and GCS were -0.192 and -0.309, respectively.

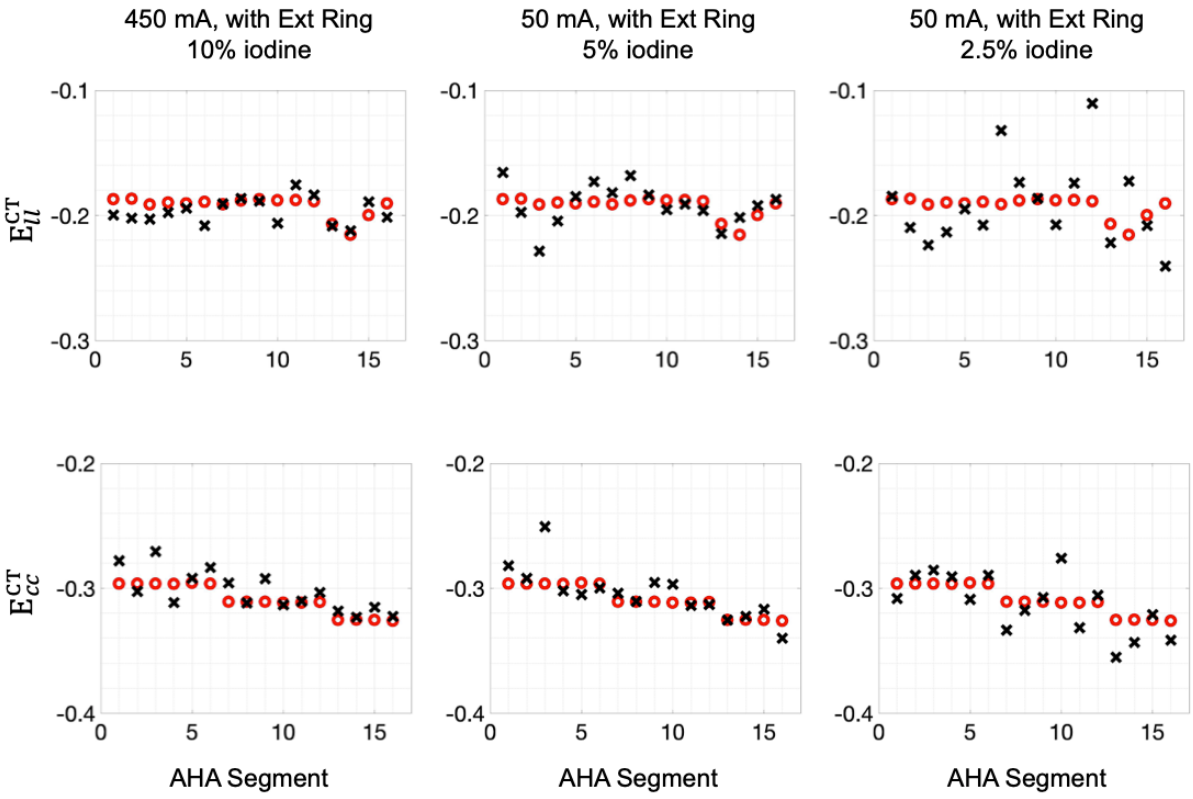

Figure 34. E_{ll}^{CT} (top) and E_{cc}^{CT} (bottom) as a function of AHA segment number with ground truth strain shown in black and measured strain in red for 3 of the 7 experiments. 450 mA with the extension ring (left) had the highest clinically-relevant CNR (40.1), 50 mA with the extension ring and 5% iodine (middle) resulted in a CNR (8.6) similar to the average of clinical scans, and 50 mA with the extension ring and 2.5% iodine (right) had a CNR (2.7) lower than most clinical scans.

5.3.2 Estimating precision of the proposed algorithms

The precision of the proposed methods was evaluated at the lower limits of image quality achieved using standard clinical reconstruction protocols. For the global parameters of LV twist, torsion, GLS, and GCS the absolute errors and the variation of those errors were low as shown in Table 13. The regional variation across the 10 independent experiments for slice-by-slice rotation, $\mathrm{E}_{ll}^{\mathrm{CT}}$, and $\mathrm{E}_{cc}^{\mathrm{CT}}$ is shown in Figure 35.

Table 13. The mean and standard deviation of absolute error is shown for the 10 independent measurements of LV twist, torsion, GLS, and GCS.

Parameters			**Absolute Error (Measured-Ground Truth)**			
mA	% Iodine	LV-myo CNR	LV twist Error (°)	LV torsion Error (°/cm)	GLS Error	GCS Error
50 mA	5	8.7 ± 0.2	-1.4 ± 1.3	0.1 ± 0.01	0.002 ± 0.003	0.004 ± 0.001

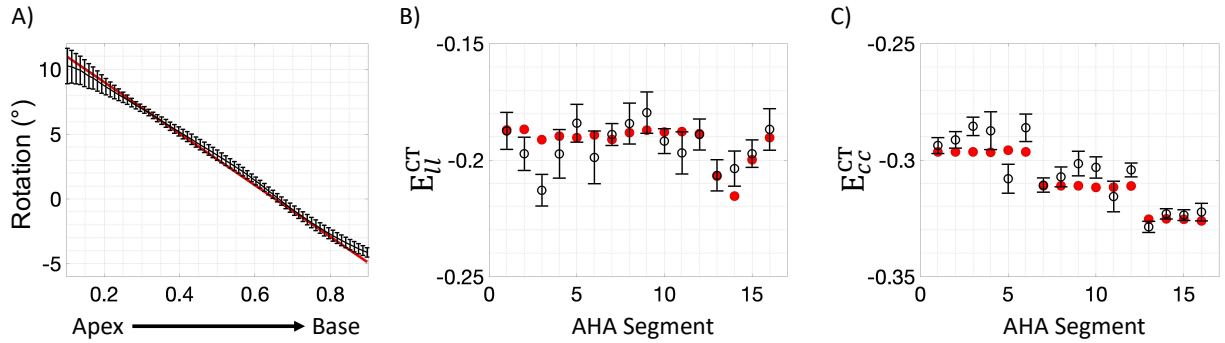

Figure 35. A) Shown in the red is the ground truth rotation function from the apex to the base and in the black the mean and standard deviation of the slice-by-slice rotation estimates from 10 independent scans at 50 mA with 5% iodine in water. B) Ground truth longitudinal strain for the 16 AHA segments shown in red and the mean and standard deviation of the measured strains shown in black for the 10 scans. C) Ground truth circumferential strain shown in black with measured mean and standard deviation in black for the 10 scans.

5.4 Discussion

5.4.1 Main Findings

In this chapter, we use phantom experiments to validate novel algorithms for measuring endocardial rotation and standard cardiac strains from 3D deformation fields derived from 4DCT images. The displacement fields are obtained using point cloud registration on the high-resolution and feature-dense endocardial surface obtained by segmenting the LV blood pool in 3D and in the native scanner coordinates. A local affine motion model is then fit to the registered displacement of the vertices using ML estimation. Slice-by-slice rotation, LV twist, LV torsion, E_{ll}^{CT} and, E_{cc}^{CT} are all derived from the affine transformation matrix for either a 2D slice (for rotation) or 3D patch of points (for local strains).

The accuracy and precision of the proposed methods were evaluated as a function of image quality using a 3D-printed phantom with known physiologic displacements as the ground-truth. Image noise was quantified using a CNR (range: 70.1 to 2.7). Across this range of image quality, the absolute errors in rotation and strain were low between the measured rotation and strain parameters and the ground truth values. It is evident in Figure 33 that there were larger errors toward the extreme ends of the ventricle. Toward the apical cap, there are fewer points in a slice and therefore the estimate of rotation is not as accurate. Toward the mitral valve plane, CPD registration is difficult because of the lack of fiducial markers in this region. To avoid these inaccuracies, the apex was defined as 10% of the ventricle and the base as 90% to avoid these regions with larger errors when calculating LV twist and torsion. The results from the 10 independent analyses demonstrate the high precision and reproducibility of these novel methods for measuring both global and regional LV deformation.

5.4.2 Clinical Relevance

Numerous studies have demonstrated that a change in LV rotation and strain can be used to diagnose various cardiac diseases, evaluate a patient's prognosis, and predict outcomes of interventions. For example, Charbonnel *et al.* showed that GLS increased from -19.1% to -17.3% in patients after they received a cumulative dose of 150 mg/m^2 of anthracyclines as treatment for cancer [118]. Initial results from Jolly *et al.* demonstrate that GCS could also be an important parameter for evaluating subclinical dysfunction in chemotherapy patients. In this study, they saw a 1.23% increase in GCS [119]. Mornos and Petrescu also showed the importance of evaluating GLS and LV twist in patients receiving anthracyclines for earlier detection of cardiotoxicity. In this study, they introduced a new parameter where they multiplied GLS and LV twist, which increased in patients who developed cardiotoxicity after 6 weeks of anthracycline treatment [120]. In this chapter, we demonstrated that our proposed algorithms were able to measure these parameters accurately and precisely from 4DCT images with varying image quality and therefore could be a

robust tool to evaluate cardiac function in this patient population. Given these results, and the studies mentioned above, we hypothesize that these 4DCT-derived metrics of function would be useful in detecting disease and predicting outcomes.

2D Speckle-tracking echocardiography has also been used for measuring regional strain because of its high temporal resolution and widespread availability, however, both the image acquisition and analysis processes yield results that have well documented user and vendor variability [99], [121]. During acquisition, the operator prospectively chooses the imaging plane based on the available acoustic window. Definition of the apical plane, which significantly affects the measurement of LV twist, is especially difficult due to lack of anatomical landmarks for standardization [122]. In addition, foreshortening in the long axis, tilting of the beam in the short axis, and through-plane motion can also lead to errors in measurements [32]. The analysis requires the user to draw epicardial and endocardial contours to define the myocardium in the 2D slice and the segmental strain varies depending on which wall layers are incorporated by the user [32]. The proposed methods for measuring endocardial rotation and strain from 4DCT images address some of these limitations by conducting the analysis using the full 3D volume. In addition, the endocardial surface is determined reproducibly using Otsu's method. This removes the need for drawing subjective contours in defining the endocardial surface which dramatically increases the reproducibility of the technique. With advances in machine learning for cardiac segmentation, this process could become fully automated in the next few years [123]–[125].

5.4.3 Limitations

While simply decreasing the x-ray tube current did not affect the image quality as drastically as expected due to the noise-reducing influence of iterative reconstruction algorithms, a wide range of CNR values were achieved to evaluate the accuracy of the proposed algorithms. Yet, at the lower limits of image quality tested, the algorithm still performed quite well. This is most likely due to the iterative reconstruction algorithms and point cloud registration technique within

the image reconstruction and analysis pipeline which are nonlinear processes that inherently smooth the data. Because of this, extremely noisy measurements were not achieved. Instead, as shown in the figures, the errors along the length of the ventricle have spatial coherence. However, over the whole range of noise instances tested which cover those seen in clinical scans, the absolute errors are low and the precision for a clinically relevant CNR is high.

5.5 Acknowledgments

Chapter 5, in part, is a reprint of the material as it is published in: Gabrielle M. Colvert, Juan E. Ortuño, W. Patricia Bandettini, Marcus Y. Chen, Maria J. Ledesma-Carbay, Elliot R. McVeigh. “4DCT-derived Endocardial Left Ventricular Torsion Correlated with CMR Tagging-derived Torsion in the Same Subjects.” in JACC: Cardiovascular Imaging (2020). The dissertation author was a primary author of this paper.

Chapter 5, in part, is a reprint of the material as it is published in: Gabrielle M. Colvert, Ashish Manohar, Brendan T. Colvert, Andrew Schluchter, Francisco J. Contijoch, Elliot R. McVeigh. “Novel measurement of LV twist using 4DCT: quantifying accuracy as a function of image noise.” in Proc. SPIE 10953, Medical Imaging 2019: Biomedical Applications in Molecular, Structural, and Functional Imaging. The dissertation author was a primary author of this paper.

Chapter 6: 4DCT-derived regional left ventricular endocardial strain evaluated in human subjects

6.1 Introduction

In this chapter, we demonstrate that our novel method for measuring LV regional endocardial strain from 4DCT images can be performed on standard clinical images. First, we compare the results of this method in the same human subjects to CMR-derived strains as the reference standard. We also derive the normal range of values for 4DCT-derived regional longitudinal and circumferential strains in a cohort of subjects with normal LV function. Lastly, we demonstrate that the proposed method is able to identify regional abnormalities in subjects with previous myocardial infarction (MI) with high precision.

6.2 Materials and Methods

6.2.1 Comparison of 4DCT- and CMR tagging-derived regional strain

6.2.1.1 Subjects

Twenty-five consecutive subjects with retrospectively-gated CT Angiography (CTA) and CMR tagging exams on the same day were acquired (Table 14). The average time between the CMR and CT exams was 4.1 $\pm$ 1.5 hours. All subjects were scanned under IRB approved protocols at the U.S. National Institutes of Health (NIH), Bethesda, Maryland. Subjects were in a study evaluating coronary artery disease (CAD) from CTA and valve and aortic disease using CMR. An example subject is shown in Figure 36. To compare strain estimates from the two modalities, the locations of the 2D CMR planes were registered in the CT volumes as shown in Figure 36B. The normalized position of the mid slice, F_m, was computed at end-systole (ES) and averaged for 3 LAX CMR views. For the CT estimates, the z-axis of the registered point cloud at ES was normalized and the slice closest to F_m was identified. An average of strain in surrounding slices was taken to match the slice thickness of the CMR data. The walls in both the CT and CMR

data were divided into 8 segments: anterior, anteroseptal, septal, inferoseptal, inferior, inferolateral, lateral, and anterolateral.

Table 14. Basic characteristics of subjects for 4DCT- and CMR-derived strain comparison

N	25
Age (years)	55 ± 14
Men (%)	16 (64)
Body Mass Index (kg/m^2)	27.9 ± 4.3
4DCT-derived Ejection Fraction (%)	68.8 ± 7.6
Time between CMR and CT (hours)	4.1 ± 1.5
Obstructive Coronary Artery Disease (%)	1 (4)
Mild/Moderate Aortic Stenosis (%)	5 (2)
Bioprosthetic Aortic Valve (%)	3 (12)
Known Myocardial Infarction (%)	0 (0)
Diabetes (%)	1 (4)
Congestive Heart Failure (%)	0 (0)
Smoker (%)	7 (28)
Hyperlipidemia (%)	16 (64)

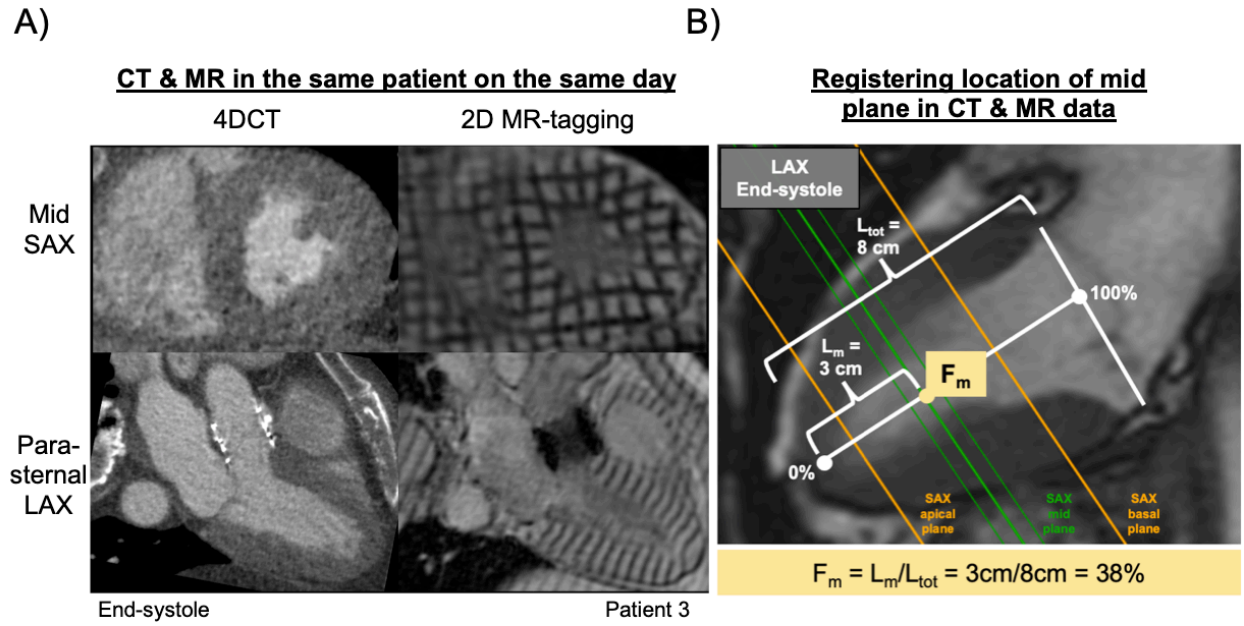

Figure 36. A) On the left is a mid-short-axis (SAX) view and below it a parasternal long-axis (LAX) view from a subject's 4DCT exam at end-systole. On the right are the same views for the same subject from the 2D MR-tagging exam. B) To register the location of the mid plane in the CT and CMR data, its normalized position, F_m, was measured in 3 LAX MR views at end-systole and averaged. The corresponding location was found in the CT data.

6.2.1.2 4D Computed Tomography Imaging

Single-heartbeat, retrospectively-gated CTA exams were obtained during an inspiratory breath-hold on a 320 detector row Aquilion ONE (Canon Medical Systems) scanner with a gantry rotation time of 275 ms. All studies were dose modulated with the x-ray tube current (mA) at maximum only during diastasis and 20% of the maximum at all other time points. Datasets were reconstructed to have at least 10 timeframes across the cardiac cycle, 0.5 mm slice thickness, and pixel spacing of 0.4 x 0.4 mm. The mean dose length product (DLP) was 198.4 mGy*cm ± 134.6 mGy*cm and the mean contrast-to-noise ratio (CNR) between the LV blood pool and the myocardium was 10.1 ± 3.1.

6.2.1.3 2D Cardiac Magnetic Resonance Tagging Imaging

CMR tagging exams were conducted on a 1.5-T scanner (MAGNETOM Aera, Siemens Medical Solutions). Three LAX planes (2- and 4-chamber and parasternal) and three evenly

spaced SAX planes (apex, mid, and base) were acquired with an ECG-triggered, segmented k-space, grid tagged gradient-echo imaging protocol. The slice thickness varied from 6-8 mm.

6.2.1.4 Global and regional left ventricular function evaluated using 4DCT

E_{ll}^{CT} and E_{cc}^{CT} were measured in all 25 subjects using the methods described in 4.2.3 and summarized again in Figure 37. A patch size of radius 7.5 mm was used to evaluate regional deformation in these subjects. This patch size was chosen based on a previous study we performed where we derived the spatial resolution limit for which we can detect regional abnormalities in endocardial deformation using CPD and the algorithm for nonrigid registration of the point clouds [126].

4DCT-dervied global parameters of function, such as EF and Global longitudinal strain (GLS), were also computed. GLS was derived from the CT images; contours were drawn through the LV myocardium in the dicom viewer Horos (v3.1.2, Nimble Co LLC, Annapolis, MD) in two orthogonal long-axis views (4-chamber and 2-chamber views) at the ES and ED time frames. GLS was defined as:

$$\mathrm{GLS} = \frac{C_{ES} - C_{ED}}{C_{ED}} \tag{6.1}$$

where C_{ES} is the length of the contour at ES and C_{ED} is the length at ED. An average was taken of GLS calculated from the two orthogonal views. LV volumes were computed from the 4DCT scans by counting the number of voxels identified as blood pool in the LV segmentation from the tip of the endocardial apex to the mitral valve plane. These volumes excluded the papillary muscles and were used to calculate EF.

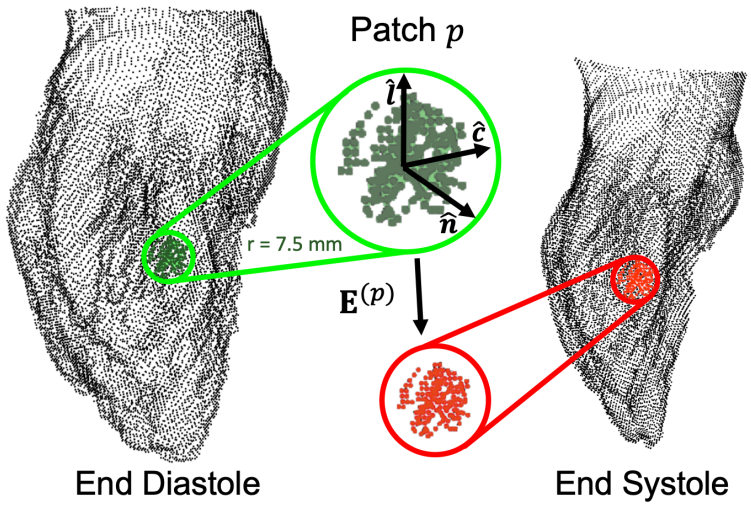

$$\text{Affine Transformation:} \quad \boldsymbol{y} = \boldsymbol{A}^{(p)}\boldsymbol{x} + \boldsymbol{b}^{(p)} + \boldsymbol{\epsilon}\left(\sigma^{(p)}\right) \quad (1)$$

$$\text{Endocardial Strain:} \quad \mathbf{E}^{(p)} = \frac{1}{2}\left(\mathbf{A}^{(p)\prime}\mathbf{A}^{(p)} - \mathbf{I}\right) \quad (2)$$

Figure 37. Regional endocardial strain is measured from the displacement fields by sampling the surface patches of radius 7.5mm. Their deformation is modeled as an affine transformation and maximum likelihood estimation is used to fit the motion model to each patch, p. The affine transformation matrix, $\mathbf{A}^{(p)}$, is used to calculate the strain tensor, $\mathbf{E}^{(p)}$, which is rotated into cardiac coordinates to obtain regional longitudinal, E_{ll}^{CT}, and circumferential, E_{cc}^{CT}, strain.

6.2.1.5 Regional endocardial strain from CMR Tagging

Due to the limited spatial resolution of the images, the fading of tags at ES, and the interference of the orthogonal tag patterns, the quality of the tagged CMR data was variable and limited automatic quantification in the majority of subjects. Therefore, three trained cardiovascular imaging experts with ≥5 years of experience manually computed and averaged strain in high quality image regions in the endocardium. In 6 subjects with good image quality, the manual strain measurements were validated with automatically-derived strain.

Manual measurements were performed using the distance measurement tool in the DICOM viewer Horos (v3.1.2, Nimble Co LLC, Annapolis, MD). Regional circumferential strain was measured from mid-LV SAX images (Figure 38A) and longitudinal strain from 2- and 4-chamber LAX images (Figure 38B,C) and defined as

$$\mathrm{E}_{ll/cc}^{MR'} = \frac{L_{ES} - L_{ED}}{L_{ED}} \tag{6.2}$$

where $\mathrm{E}_{ll/cc}^{MR'}$ is the engineering strain, L_{ES} is the length of the segment between tag minima at ES, and L_{ED} is the length of the segment at ED, assumed to be the initial tag spacing of 8 mm. The ES tag spacing was measured between the minima of one or two tags and sufficiently close to the endocardium for comparison to the CT strains. SAX segments were excluded if the displacement of the tags was not in the circumferential direction or an orthogonal tag interfered with the measurement. For longitudinal strain, segments were excluded if the LAX plane did not pass through the center of the blood pool or if the parallel tagging stripes were not perpendicular to the LAX. To ensure the CT and CMR methods were measuring the same type of strain, engineering strain was converted to Green strain, $\mathrm{E}_{ll/cc}^{MR}$, by

$$\mathrm{E}_{ll/cc}^{MR} = \mathrm{E}_{ll/cc}^{MR'} + \frac{1}{2}\left(\mathrm{E}_{ll/cc}^{MR'}\right)^2 \tag{6.3}.$$

Bland-Altman plots were constructed to quantify the agreement between the CT- and CMR-derived estimates of regional strain across the 25 subjects. A F-test was also performed to compare the variance in strain estimates between the two modalities with a significance level set to 0.05.

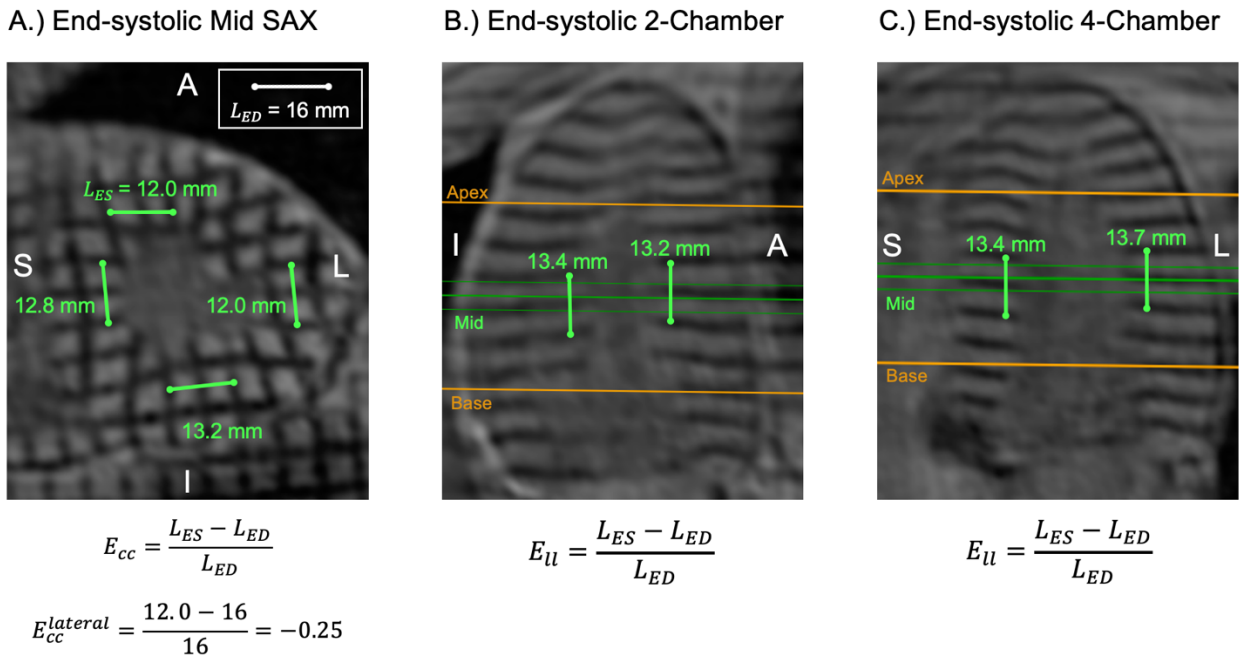

Figure 38. A) Circumferential engineering strain was measured from the mid short-axis (SAX) slice of the CMR-tagged data. 3 expert observers measured the distance between the minima of one or two tags at end-systole (ES), L_{ES}. An example calculation is shown for the lateral wall. Longitudinal engineering strain was measured for the mid slice from the 2-chamber (B) and 4-chamber (C) long-axis (LAX) views. The distance at end-diastole (ED), L_{ED}, was set by the tag spacing (8mm) and was the same for SAX and LAX.

6.2.1.6 Validation of manually derived CMR strains with automatically derived strains in subjects with good image quality.

Automatic analysis of the CMR tagging data could not be performed in all subjects due to suboptimal image quality. However, a total of 6 SAX and 7 LAX tagged CMR sequences from 6 subjects were automatically analyzed. This previously validated automatic method utilized nonrigid image registration, with knot spacing of 8 mm and a regularization term of 1.2, to estimate the deformation of the tagging grid [127]. These automatic estimates were compared to the manual measurements in the same subjects by constructing Correlation and Bland-Altman plots.

6.2.2 Regional longitudinal and circumferential strain in subjects with normal left ventricular function

$\mathrm{E}_{ll}^{\mathrm{CT}}$ and $\mathrm{E}_{cc}^{\mathrm{CT}}$ were computed in 23 subjects (Table 15) with normal LV systolic function to establish a range of normal values for these 4DCT-derived regional strains. All subjects had a CTA or Cardiac Morphology exam under IRB approved protocols at the University of California San Diego (UCSD) and were selected chronologically from January 2018-April 2020. The radiologist noted that the subjects had normal LV function with no wall motion abnormalities. Subjects were excluded if they had severe aortic stenosis, pacemaker, nitroglycerin administered prior to the CT, atrial fibrillation, severe coronary artery disease, stents, or LV hypertrophy or dilation. Exams were single-heartbeat and retrospectively-gated and performed on a Revolution CT scanner (GE Medical Systems, Wisconsin) with pixel spacing of 0.39 mm x 0.39 mm and slice thickness of 0.625 mm. $\mathrm{E}_{ll}^{\mathrm{CT}}$ and $\mathrm{E}_{cc}^{\mathrm{CT}}$ were computed for the 16 American Heart Association (AHA) segments (excluding the apical cap) [107] and averaged across the subjects to obtain mean and standard deviation curves versus R-R interval percentage for each segment.

Table 15. Basic characteristics of subjects with normal LV function. *LVEF = Left ventricular ejection fraction, **GLS = Global longitudinal strain

N	23
Age	60 ± 12
Male (%)	12 (52.2)
4DCT-derived LVEF* (%)	70.0 ± 4.7
4DCT-derived GLS (%)**	20.9 ± 2.1

6.2.3 Demonstration of abnormal strain in subjects with previous myocardial infarction

To demonstrate the ability of the proposed 4DCT algorithm to capture abnormalities in regional LV function, $\mathrm{E}_{ll}^{\mathrm{CT}}$ and $\mathrm{E}_{cc}^{\mathrm{CT}}$ were measured in two subjects with previous MI reported in their clinical history. Both subjects were analyzed under an IRB approved protocol at UCSD. They underwent single-heartbeat, retrospectively-gated 4DCT exams on a Revolution CT scanner (GE

Medical Systems, Wisconsin) with pixel spacing of 0.39 mm x 0.39 mm and slice thickness of 0.625 mm. The studies were evaluated by a clinical radiologist who confirmed the size and location of the local wall motion abnormality (WMA) associated with the previous MI. The first subject had a large apical WMA, and the second subject had a smaller WMA on the inferior/inferolateral wall. For both subjects, $\mathrm{E}_{ll}^{\mathrm{CT}}$ and $\mathrm{E}_{cc}^{\mathrm{CT}}$ vs. R-R interval percentage and peak strain were computed for 16 AHA segments and compared to the normal values. Peak strain was defined as the minimum point on the strain vs. % R-R curves. A segment was considered abnormal if peak strain was two standard deviations outside of the normal range as determined in 6.2.2.

A reproducibility study was also performed on these two subjects. Observer 1 re-segmented ED and ES frames for both subjects. A second observer independently segmented ED and ES timeframes, twice. There was a minimum of 24 hours between the first and second segmentation for a single subject for both observers. End-systolic strain was computed for the 16 AHA segments and compared between segmentations for a single observer and between the two observers. Bland-Altman plots were constructed to quantify inter- and intra-observer variability. Correlation coefficients were also computed using MATLAB's *corcoeff* with a significance level set to 0.05.

6.3 Results

6.3.1 Comparison of CT- and CMR-derived strains

4DCT-derived $\mathrm{E}_{ll}^{\mathrm{CT}}$ and $\mathrm{E}_{cc}^{\mathrm{CT}}$ were compared to CMR tagging-derived strains. Across the 25 subjects, 61 segments were compared for circumferential strain and 50 segments for longitudinal strain. Figure 39 shows the results of this comparison. The mean difference between the CT and CMR-derived circumferential strains was -0.05 ± 0.07 and -0.03 ± 0.04 for the longitudinal strains. While the Bland-Altman analyses revealed a bias between the two modalities, the F-test showed no statistically significant difference between the variances in strain values.

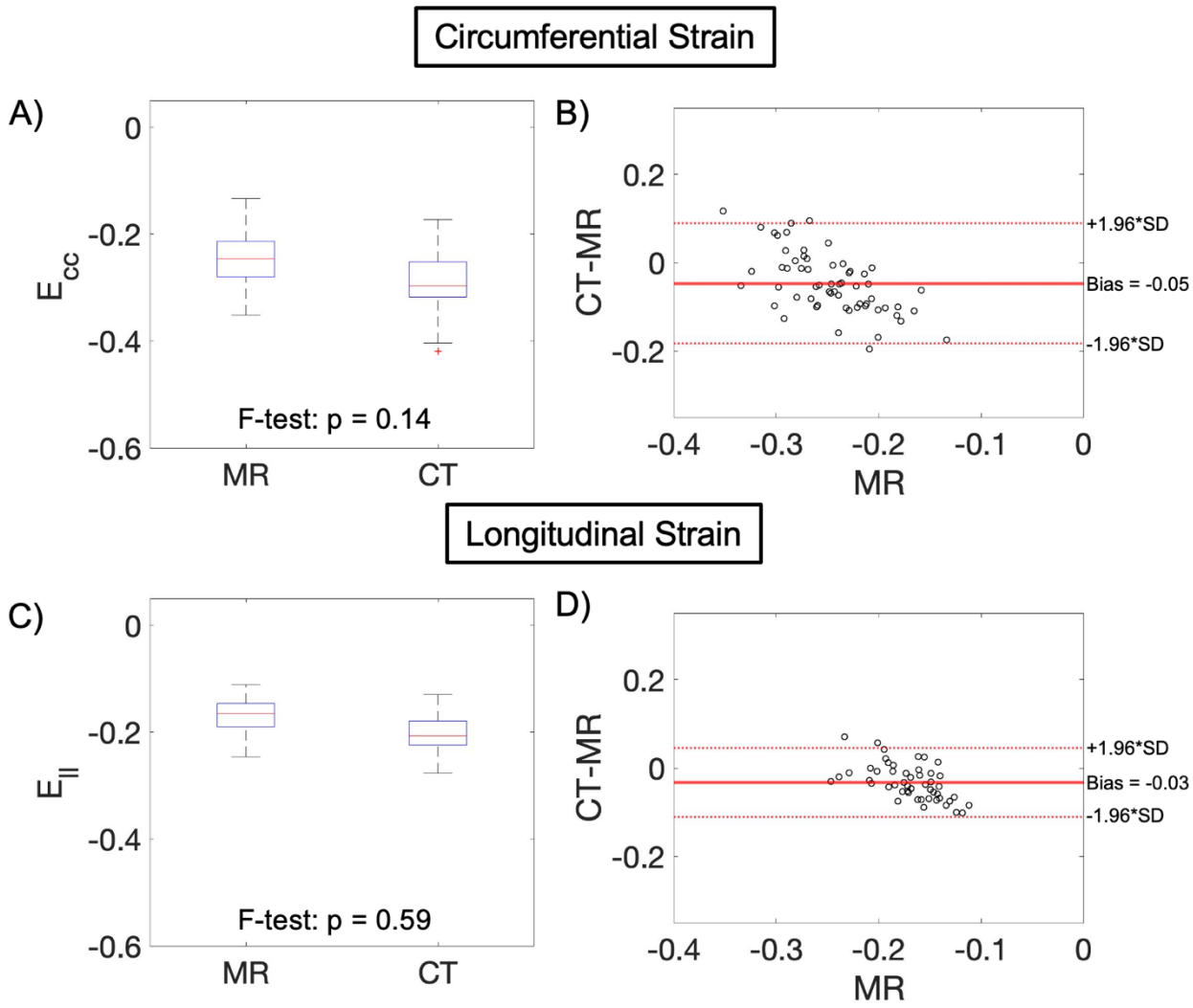

Figure 39. Boxplots and Bland-Altman plots are shown for the comparison of CT- and CMR-derived circumferential (A) and longitudinal strain (B) and indicate good agreement between the methods. There was a bias towards greater magnitude strain values from CT images in both cases. F-tests were also performed and show similar variances in strain estimates for both modalities.

6.3.2 Regional longitudinal and circumferential strain in subjects with normal left ventricular function

E_{ll}^{CT} and E_{cc}^{CT} were measured in a cohort of 23 subjects with normal LV function to determine the range of normal strain values. Across all subjects and segments, global peak E_{ll}^{CT} was -0.19 ± 0.04 and global peak E_{cc}^{CT} was -0.29 ± 0.04. Figure 40 shows the mean and ±1 standard deviation of E_{ll}^{CT} and E_{cc}^{CT} for the 16 AHA segments across the full R-R interval.

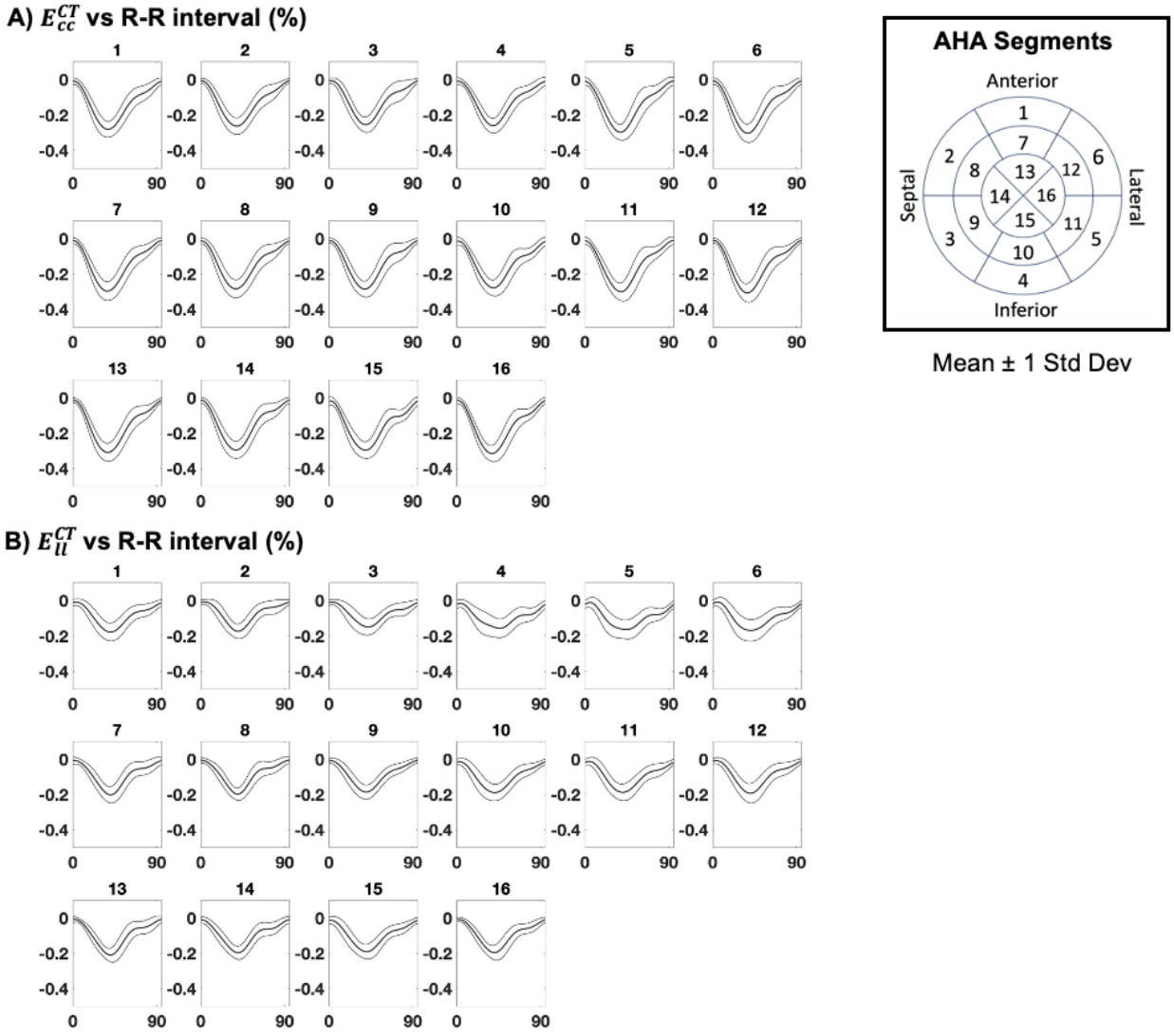

Figure 40. Strain vs. R-R interval percentage for E_{cc}^{CT} (A) and E_{ll}^{CT}(B) for 16 American Heart Association (AHA) segments. The thicker middle line is the mean strain across all subjects and the thinner outer lines show 1 standard deviation from the mean.

6.3.3 Regional longitudinal and circumferential strain in subjects with abnormal left ventricular function

$\mathrm{E}_{ll}^{\mathrm{CT}}$ and $\mathrm{E}_{cc}^{\mathrm{CT}}$ were evaluated in two subjects with previous MI to demonstrate the ability of the proposed 4DCT algorithm to detect regional WMAs. Figure 41 shows the $\mathrm{E}_{ll}^{\mathrm{CT}}$ and $\mathrm{E}_{cc}^{\mathrm{CT}}$ vs. R-R interval percentage curves for abnormal subject #1. The abnormal curves are shown on top of the normal curves with mean ±1 standard deviation. As shown in the figure and marked with an

asterisk, all apical and mid segments, and a few basal segments for peak E_{ll}^{CT} and E_{cc}^{CT} were greater than two standard deviations above the mean from normal. Subject 1 had a 4DCT-derived EF of 40% and 4DCT-derived global longitudinal strain (GLS) of 11.2%. Subject #2 had a smaller WMA, 4DCT-derived EF of 57%, and 4DCT-derived GLS of 19.8%. For circumferential strain, segments on the inferior/lateral wall were abnormal (segments 4, 5, 10, 11, 12, and 15 in Figure 42). No segments had abnormal longitudinal strain.

Figure 43 shows the results of the reproducibility study performed on these two subjects. Correlation was high between segmentations from one observer (Figure 43A; R=0.86 and R=0.91) and between two observers (Figure 43B; R=0.73 and R=0.83) for both E_{ll}^{CT} and E_{cc}^{CT}. The standard deviations for inter-observer variability (±0.07 and ±0.05) and intra-observer variability (±0.05 and ±0.04) were also similar for both strains.

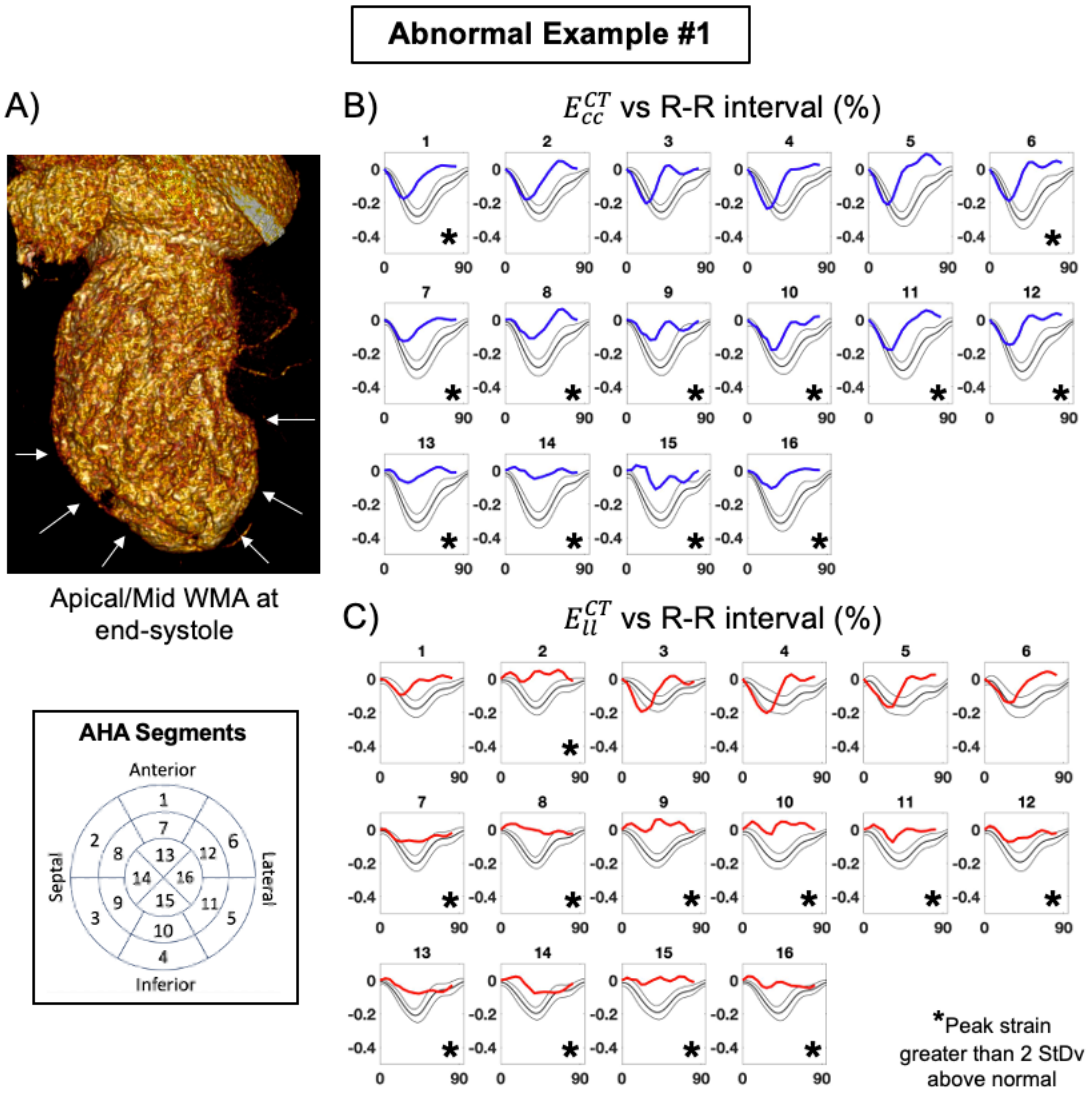

Figure 41. A) 3D rendering at end-systole of the LV blood pool from a subject with a large apical/mid wall motional abnormality (WMA). E_{cc}^{CT} (B) and E_{ll}^{CT}(C) vs. R-R interval percentage for 16 American Heart Association (AHA) segments for this subject are shown superimposed on top of the normal curves with 1 standard deviation from the mean. Peak strain values that were 2 standard deviations above normal are marked with an asterisk (*).

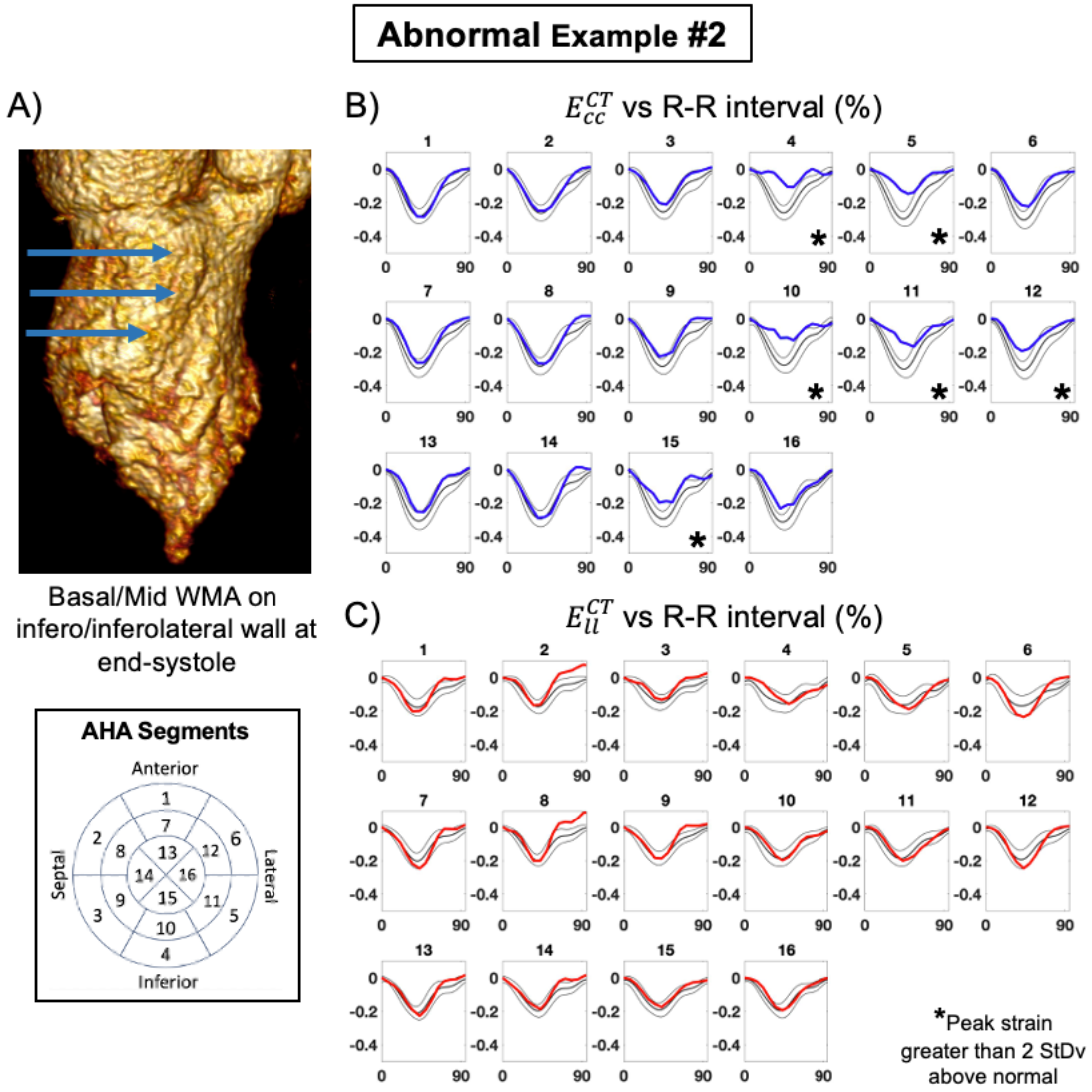

Figure 42. A) 3D rendering at end-systole of a subject with a small basal/mid wall motion abnormality (WMA) on the inferior/lateral wall. E_{cc}^{CT} (B) and E_{ll}^{CT}(C) vs. R-R interval percentage for 16 American Heart Association (AHA) segments for this subject are shown superimposed on top of the normal curves with 1 standard deviation from the mean. Peak strain values that were 2 standard deviations above normal are marked with an asterisk (*).

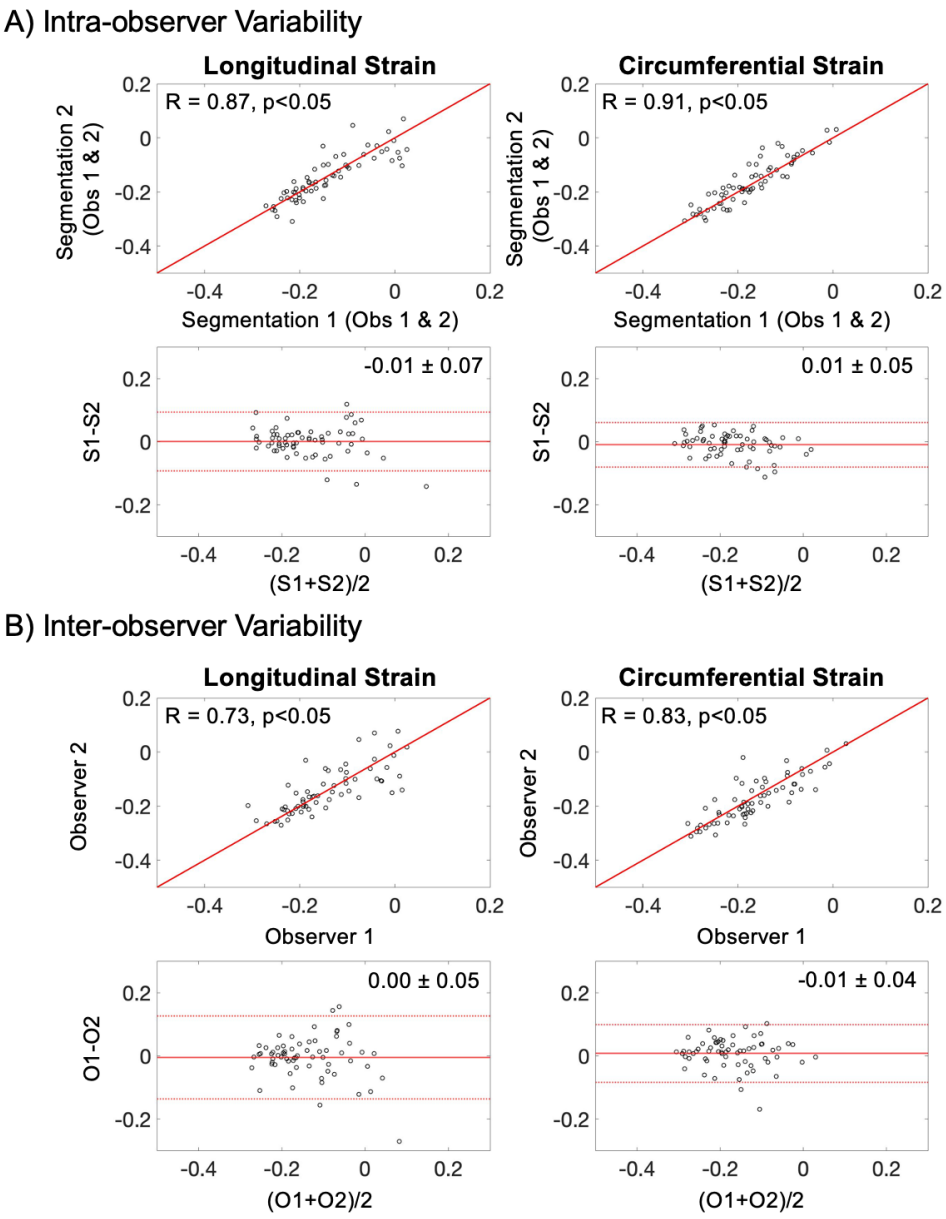

Figure 43. A) Correlation and Bland-Altman plots showing intra-observer variability for both E_{cc}^{CT} and E_{ll}^{CT}. Differences in strain for independent segmentations (S1 and S2) performed at least 24 hours apart for both observers (Obs 1 & 2) are quantified. **B**) Correlation and Bland-Altman plots showing inter-observer variability for both $\mathrm{E}_{\mathrm{cc}}^{\mathrm{CT}}$ and $\mathrm{E}_{\mathrm{ll}}^{\mathrm{CT}}$. Differences in strain for the two observers (O1 and O2) for both segmentations are quantified.

6.3.4 Comparison of automatic and manual strain from CMR tagging

Differences between the automatic and manual CMR strains were computed relative to the mean manual green strain and resulted in an absolute difference of 0.03 ± 0.02 for the SAX and an absolute difference of 0.02 ± 0.02 for the LAX. Correlation analysis resulted in a R=0.82

(p-value < 0.001) for the SAX and R=0.77 (p-value< 0.005) for the LAX, showing good agreement between the manual and automatic strain results. In the same cases and segments for the manual measurements, the interobserver absolute differences were 0.02 ± 0.02 for the SAX analysis and 0.03 ± 0.02 LAX analysis. Therefore, errors between the automatically and manually derived strain estimates were similar to the variability between observers for the manual measurements. In addition, the inter-observer variability shows that the 3 observers were within a quarter of a pixel length in their manual measurements.

6.4 Discussion

6.4.1 Main Findings

In this chapter, we compared circumferential and longitudinal endocardial strain in humans from 4DCT to CMR tagging-derived strain in the same subjects. Our analysis revealed good agreement between the modalities with a slight bias towards larger magnitude CT-derived strain for both longitudinal and circumferential strain. The CT estimates are derived from the endocardial surface where strain is higher than in the midwall or epicardium [117]. While CMR measurements were made as close to the endocardium as possible, they were still within the myocardium and subject to the position of the tagging grid. Despite this bias, the F-tests revealed that the two methods had similar variances for both strain measurements. There was a wider limit of agreement for circumferential strain mostly likely due to the larger dynamic range of those estimates compared to longitudinal strain.

Analysis of $\mathrm{E}_{ll}^{\mathrm{CT}}$ and $\mathrm{E}_{cc}^{\mathrm{CT}}$ in subjects with normal LV function allowed us to establish normal regional strain curves for the full cardiac cycle. For both strain values, the variability in the peak strain values across all 23 subjects and for all AHA segments was low, indicating the high precision and reproducibility of the proposed 4DCT method.

In addition to comparing strain from CT and CMR images in the same cohort of human subjects, we demonstrated the ability of 4DCT-derived regional strain to detect abnormalities in

LV function in regions affected by a previous MI with high precision. Example subject #1 had a very large apical/mid WMA that affected both $\mathrm{E}_{ll}^{\mathrm{CT}}$ and $\mathrm{E}_{cc}^{\mathrm{CT}}$. The drop in regional function was consistent with low global function parameters. Peak strains in most basal segments were unaffected; however, in the majority of all segments, diastolic relaxation occurred much earlier than in the normal cohort, demonstrating sensitivity to temporal changes in contraction. Example subject #2 had a more localized WMA in the basal/mid region on the inferior/lateral wall where $\mathrm{E}_{cc}^{\mathrm{CT}}$ segments were lower, and the EF was lower than identified in the normal cohort. Interestingly, GLS was within the normal range and no $\mathrm{E}_{ll}^{\mathrm{CT}}$ segments were considered abnormal in this subject. These results show that abnormalities in $\mathrm{E}_{ll}^{\mathrm{CT}}$ and $\mathrm{E}_{cc}^{\mathrm{CT}}$ can be quantified independently using our proposed algorithm.

6.4.2 Clinical Relevance

These results are crucial because recent studies have shown longitudinal and circumferential strain do not always have the same prognostic value. For example, reduced GLS, as measured with speckle-tracking echocardiography, was associated with treatment-requiring cardiac allograft rejection [128]. Circumferential and radial strain were not associated with an increase risk. Another study showed using 2D CMR tagging that circumferential strain, but not longitudinal strain, correlated with improved dyssynchrony in patients after cardiac resynchronization therapy with enhanced systolic function [129]. Given the good agreement between the 4DCT- and CMR-derived regional strains, the high precision of $\mathrm{E}_{ll}^{\mathrm{CT}}$ and $\mathrm{E}_{cc}^{\mathrm{CT}}$ in normals, and the ability to identify abnormal segments accurately and reproducibly in patients with MI, the proposed method has the potential to provide important prognostic information about LV function in addition to high quality anatomical data.

6.4.3 Limitations

The comparisons between imaging modalities have limitations. The CT-based strains are measured on the endocardial surface, while the MR strains are a few millimeters within the

myocardium. Finding corresponding locations in the 2D CMR and 3D CT volumes was subject to some uncertainty. The CTA was acquired within one heartbeat whereas the CMR images were averaged over several heartbeats. Also, the CMR data was acquired at end-expiration while the CTA data was acquired at end-inspiration and while the exams were conducted on the same day, there was a short delay between them which could have led to differences in cardiovascular loading conditions. Because of these factors, perfect agreement between the two modalities is not expected.

Due to radiation dose concerns, a cohort of healthy controls is difficult to image with CT; therefore, subjects with normal LV function were assembled retrospectively based on information in the radiology report and 4DCT-derived GLS and EF. The standard deviations measured over the 23 subjects for $\mathrm{E}_{ll}^{\mathrm{CT}}$ and $\mathrm{E}_{cc}^{\mathrm{CT}}$ were tight and therefore the estimates are stable and valuable. The peak strain measured in this cohort represent what we can anticipate from the subjects commonly scanned at our institution who have normal LV function. In addition, while analysis on two example subjects with previous MI demonstrated the ability of the method to detect regional visually evident WMA, larger studies need to be undertaken to validate these methods using back-to-back imaging as shown in the CT/MR comparison.

6.5 Acknowledgments

Chapter 6, in part, has currently been submitted for publication of the material, Gabrielle M. Colvert, Ashish Manohar, Brendan T.Colvert, Juan E. Ortuño, Zhennong Chen, James Yang, W. Patricia Bandettini, Marcus Y. Chen, Maria J. Ledesma-Carbayo, Elliot R. McVeigh. “Regional left ventricular endocardial strain from 3D deformations fields derived from 4DCT images.” The dissertation author was a primary author of this paper.

Chapter 7: 4DCT-derived left ventricular rotation and torsion evaluated in human subjects

7.1 Introduction

In this chapter, we demonstrate that the proposed novel algorithm for measuring endocardial LV rotation and torsion from 4DCT images can be performed on standard clinical images and we compare the results of this method in humans to CMR tagging as the reference standard. To the best of our knowledge, this is the first study to directly compare CT and CMR tagging-derived measures of LV rotation and torsion in human subjects. We also derive normal values of LV rotation and torsion and evaluated the reproducibility of these metrics in a cohort of subjects with normal LV function.

7.2 Materials and Methods

7.2.1 Comparison of 4DCT- and CMR tagging-derived rotation and torsion

7.2.1.1 Subjects

We assessed twenty-five consecutive subjects who had retrospectively-gated CT Angiography (CTA) and CMR tagging exams on the same day. Sixteen of these subjects satisfied the following criteria: 1) an EF measured from 4DCT of less than 75 percent and 2) a LV blood pool-myocardium contrast-to-noise ratio (CNR) greater than 8 in the CT images. These criteria were set to ensure that the endocardial surface could be segmented using images of the LV blood pool. If the EF is too high, the LV blood pool will be too small at the time of peak deformation leading to the loss of fiducial markers required for motion-tracking. In addition, when the contrast between the blood pool and the myocardium is too low, the segmentation does not accurately represent the endocardial surface and can lead to errors in measurement. Phantom studies were performed to determine an appropriate CNR threshold for accurate measurement of 4DCT-derived torsion [87].

The characteristics of the 16 subjects included in this study are summarized in Table 16. All subjects were scanned under IRB approved protocols at the U.S. National Institutes of Health (NIH), Bethesda, Maryland with an average time between the MR and CT exams of 3.9 ± 1.7 hours. Subjects were in a study evaluating coronary artery disease (CAD) from CTA and valve and aortic disease using CMR. No subjects had obstructive CAD. Four subjects had cardiovascular abnormalities: One had an aortic valve replacement, one had mild aortic stenosis (AS), one had moderate AS, and one had mild AS with a small myocardial infarction and pacemaker.

Table 16. Basic characteristics of the 16 subjects included in the study.

N	16
Age (years)	51.3 ± 12.2
Men (%)	9 (56)
Body Mass Index (kg/m^2)	26.7 ± 3.4
4DCT-derived Ejection Fraction (%)	66.6 ± 4.9
Time between CMR and CT (hours)	3.9 ± 1.7
Diabetes (%)	0 (0)
Coronary Artery Disease (%)	0 (0)
Valvular Disease (%)	1 (6)
Known Myocardial Infarction (%)	0 (0)
Congestive Heart Failure (%)	0 (0)
Smoker (%)	3 (19)
Hyperlipidemia (%)	7 (44)
Hypertension (%)	6 (38)

7.2.1.2 4D computed tomography imaging

All CTA exams were retrospectively-gated and performed in a single heartbeat during an inspiratory breath-hold on a 320 detector row Aquilion ONE (Canon Medical Systems) scanner with a gantry rotation time of 275 milliseconds. For the acquisition, 55 ml of iodine contrast was injected followed by a 30 ml saline flush. All studies were dose modulated with the x-ray tube

current (mA) at maximum only during diastolic time frames, with 20% mA for all other time points. Images were reconstructed to have at least 10 timeframes across the cardiac cycle. Images were reconstructed on a 512 x 512 pixel matrix in the axial plane with 0.5 mm slice thickness and pixel spacing of 0.4 x 0.4 mm. Other scanning parameters are summarized in Table 17 for the 16 subjects included in this study. The signal-to-noise ratio (SNR) was measured in a mid-axial slice within the contrast-enhanced blood pool as

$$\mathrm{SNR} = \frac{\mu_{LV}}{\sigma_{LV}} \tag{7.1}$$

where μ_{LV} is the mean signal within the LV blood pool and σ_{LV} is the standard deviation of that signal. The CNR was calculated as

$$\mathrm{CNR} = \frac{\mu_{LV} - \mu_{myo}}{\sigma_{LV}} \tag{7.2}$$

where μ_{myo} is the mean signal within the myocardium surrounding the blood pool. Dose- length-product (DLP) was variable among the subjects; 12 had DLP 60-150mGy*cm and 4 had DLP 170-451mGy*cm.

Table 17. The acquisition parameters for the 4DCT exams are summarized as well as image quality statistics such as the signal-to-noise ratio (SNR) and contrast-to-noise ratio (CNR).

kVp	100 (N=15), 120 (N=1)
CTDIvol (mGy)	12.0 ± 8.2
DLP (mGy*cm)	147.7 ± 96.6
Dose (mSv) [range]	2.1 ± 1.4 [0.85, 6.3]
LV Blood Pool SNR	11.9 ± 2.7
LV Blood pool-myocardium CNR	10.9 ± 2.6
LV Blood Pool (HU)	617 ±110
Heart Rate during CTA (bpm)	60.1 ± 9.4

7.2.1.3 2D cardiac magnetic resonance tagging imaging

All CMR tagging exams were conducted on a 1.5-T scanner (MAGNETOM Aera, Siemens Medical Solutions). Scout images were obtained to identify the cardiac axes. Three long-axis planes (traditional 2- and 4-chamber and parasternal views) and three evenly spaced short-axis planes (apex, mid, and base) were acquired with an ECG-triggered, segmented k-space, grid tagged gradient-echo imaging protocol. The first of the three short-axis slices, the basal slice, was chosen so that at ES the LV myocardium was circular and below the membranous portion of the interventricular septum. The slice thickness varied by subject from 6 to 8 mm. Table 18 shows the average distance between the apical and basal planes as well as their location at ES as a percentage of the length of the LV from the endocardial apex (0%) to the mitral valve plane (100%). These percentages were calculated as shown in Figure 44 in three long-axis views and an average was computed for each subject. These locations were used to find the corresponding apical and basal regions of the LV in the 3D CT analysis to enable a comparison between the two modalities.

Table 18. The CMR tagging acquisition parameters are summarized as well as the location of the apical and basal planes as a percent of the left ventricle (from the apex, 0%, to the mitral valve plane, 100%).

Slice thickness (mm)	6 (N=4), 8 (N = 12)
Distance between apical and basal planes (mm)	40.7 ± 2.5
Apical Plane (% of LV)	16.9 ± 8.1
Basal Plane (% of LV)	76.6 ± 7.8

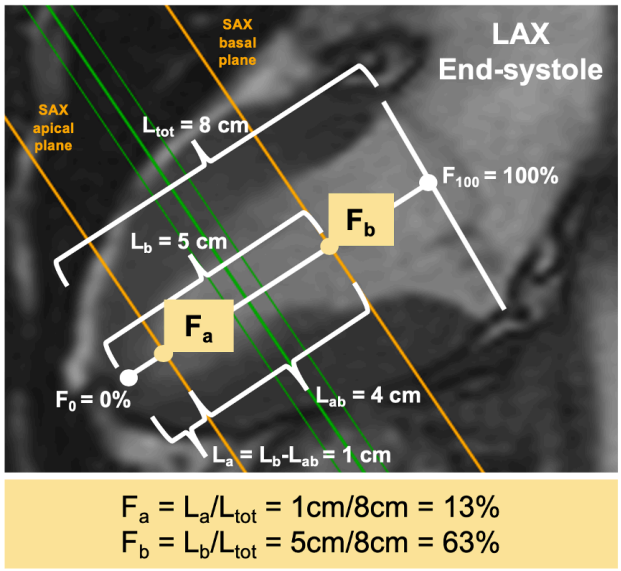

Figure 44. In three long-axis (LAX) CMR views, the normalized positions of the apex, F_a, and base, F_b, were computed at end-systole as shown here. The values from the three LAX views were averaged together to find corresponding regions in the CT data at the apex and base.

7.2.1.4 4DCT-derived left ventricular rotation and torsion

4DCT-derived LV rotation and torsion were measured as described in 4.2.2. In order to compare apical and basal rotation angles and LV torsion derived from the two different imaging modalities, the normalized position of each z-slice of the registered point cloud at ES was computed. In this normalized coordinate system, the middle slices of the apical and basal planes for the CT measurement were those closest to the locations in the CMR data of F_a and F_b, respectively. Then, an average of the surrounding slices was taken in both locations depending on the slice thickness of the CMR data. For subjects with 6 mm slice thickness, three slices on either side of the middle slice were included in the average and for 8 mm, four slices were included as shown in Figure 45. LV torsion was then defined as (apical rotation – basal rotation)/(distance between the two planes).

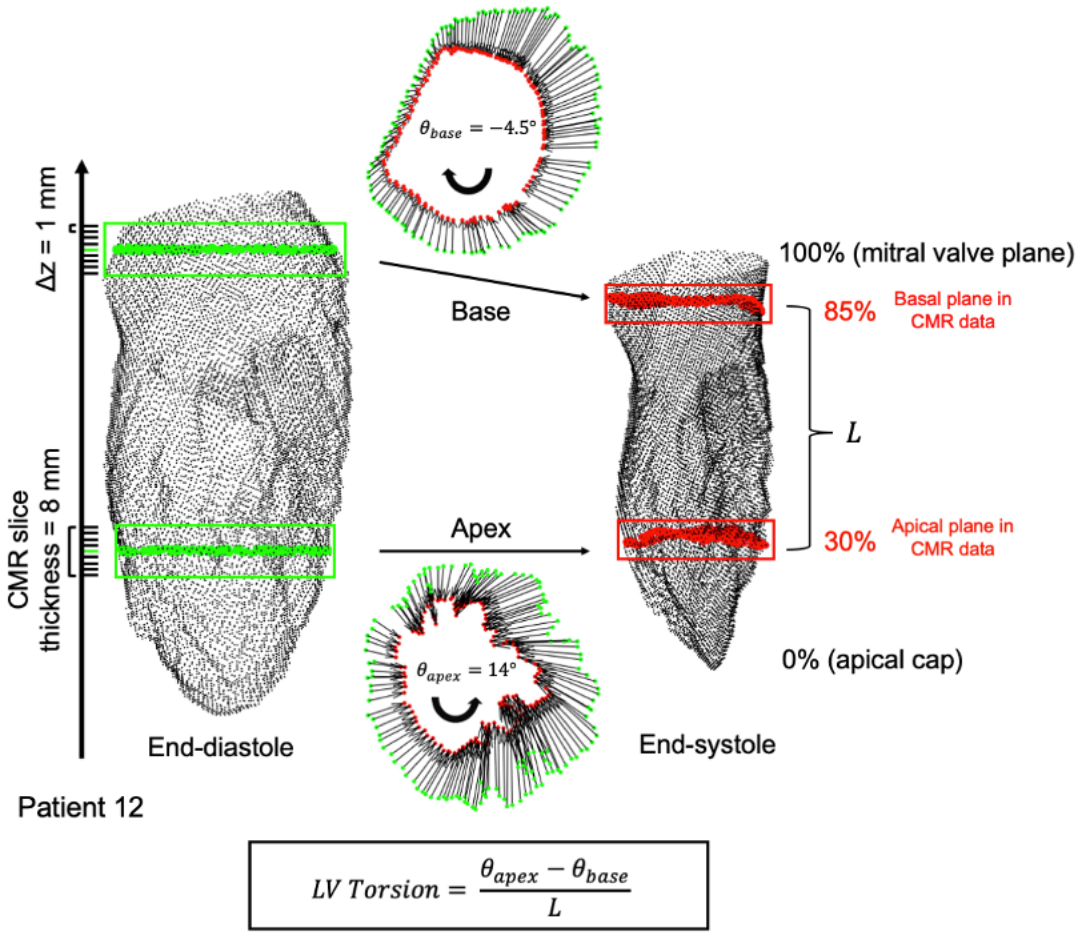

Figure 45. In red are apical and basal slices from the 4DCT data matching the CMR-derived locations at end-systole. Corresponding slices are in green at end-diastole. Rotation angles of adjacent slices are averaged together to match the thickness of the CMR data.

7.2.1.5 CMR tagging-derived left ventricular rotation and torsion

The 2D myocardial displacement field between ED and ES was derived automatically from the CMR images using methods previously described which utilize nonrigid image registration to estimate the deformation of the tagging grid [127]. Figure 46A shows the motion of the tracked pixels (represented as colored dots) for an apical slice for a single subject. Figure 46B shows the 2D displacement field for those pixels. In order to calculate endocardial rotation, the innermost points were selected (Figure 46C). To calculate a rotation angle for this 2D set of points, the same method for the CT data was used. An affine transformation was fit to the deformation of the

innermost points of the myocardium using ML estimation in order to obtain a single rotation angle for both the apical and basal planes. LV torsion was then calculated as (apical rotation – basal rotation)/(distance between the apical and basal planes).

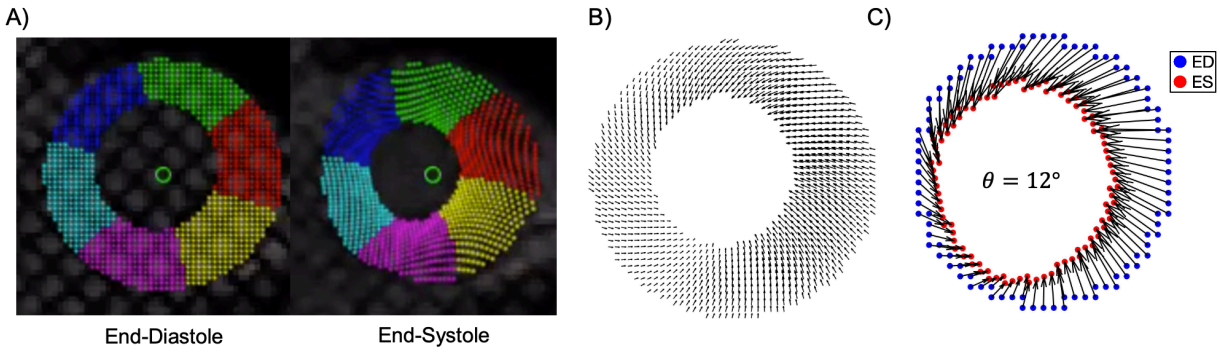

Figure 46. A) Tagged CMR images of an apical slice at end-diastole (ED) and end-systole (ES) with the pixels which were tracked through nonrigid image registration [127] overlaid with colored dots. B) The output 2D displacement field from ED to ES. C) The displacement field for the innermost layer of points used to represent the endocardium. An affine transformation was fit to this displacement field using Maximum Likelihood (ML) estimation and a rotation angle of 12° was measured.

7.2.1.6 Statistical Analysis

In order to perform a comparison between the CMR and CT-derived rotation and torsion measurements, correlation and Bland-Altman plots were constructed. Correlation coefficients were also computed for apical rotation, basal rotation, and LV torsion using the built-in function *corrcoef* in MATLAB. Lastly, a two-sided t-test was also performed in MATLAB using the built-in function *ttest2* to determine if there was a significant difference between CMR and CT-derived estimates of rotation and torsion.

7.2.2 4DCT-derived LV rotation and torsion in subjects with normal LV function

LV apical and basal rotation, twist, and torsion were computed in 13 subjects with normal LV systolic function to establish a range of normal values for these 4DCT-dervied metrics. All subjects had a CTA or Cardiac Morphology exam under IRB approved protocols at the University of California San Diego and were selected chronologically from January 2018-April 2020. These patients were a subset of the group used in 6.2.2 to establish normal ranges of regional

endocardial strain. Because we have shown in the previous studies that the measurement of LV torsion is much more sensitive to image quality and blood pool size compared to estimates of regional strain, subjects from that initial cohort were not analyzed if they had an EF >75%, end-systolic volume <25 mL, or blood pool-myocardium contrast-to-noise ratio <8 as in section 7.2.1 for the CT vs MR comparison study. The basic characteristics of the subjects included in this study are shown in Table 19. End-systolic Apical rotation was defined at 15% of the LV, basal rotation at 75% of the LV, LV twist as apical-basal rotation, and LV torsion as LV twist normalized to the length between the apical and basal planes in centimeters. Mean and standard deviations across the 13 patients for these parameters were computed. Intra- and inter-observer variability were also evaluated in half the patients (selected randomly) using 2 separate observers.

Table 19. Basic characteristics of subjects with normal LV function used to determine normal ranges of left ventricular rotation and torsion.

N	13
Male (%)	4 (31)
Age	57.6 ± 14.8
Blood pool-myocardium Contrast-to-noise ratio (CNR)	11.0 ± 2.3
4DCT-derived Ejection Fraction (%)	69.0 ± 2.6
4DCT-derived Global Longitudinal Strain (GLS)	20.7 ± 2.0

7.3 Results

7.3.1 Comparison of CT and MR-derived LV rotation and torsion

The proposed method for measuring endocardial LV rotation and torsion derived from standard clinical 4DCT images was used to successfully analyze 15 of 16 subjects included in this study. One subject, shown with an asterisk (*) in Figure 47 and Figure 48, had aberrant LV morphology leading to point-cloud registration failure of the endocardial surface and non-physiologic rotation and torsion values. This subject was determined to be an outlier and was

excluded from the statistical analyses performed as the results reported below. As evident in Figure 47A, there was good agreement between the rotation measurements with CMR tagging and CT. Using the two-tailed t-test with an alpha of 0.05, it was determined that there was no significant difference between the apical rotation values for the two modalities ($p = 0.11$), but the basal estimates were significantly different ($p < 0.05$). As shown in the Bland-Altman plot in Figure 47B, there was a small bias of 3.3° with the CT-derived rotation angles being higher than the CMR-derived estimates. The precision of the measurement of rotation angle by CT can be characterized by the standard deviation of the Bland-Altman plot which was ± 3.4º across these measurements.

Despite the systematic difference in rotation values at the base, there was still moderate correlation ($R = 0.48$, $p = 0.07$) between the CMR and CT-derived measurements of LV torsion as shown in Figure 48A. The Bland-Altman plot in Figure 48B indicated that there was a very small bias of 0.65°/cm with the CMR estimates being slightly higher than the CT measurements. The two-sided t-test with an alpha of 0.05 revealed that there was no significant difference ($p = 0.14$) between the torsion estimates from the two different imaging modalities. The precision of the measurement of torsion with CT given CMR as the reference standard was ± 1.2º/cm.

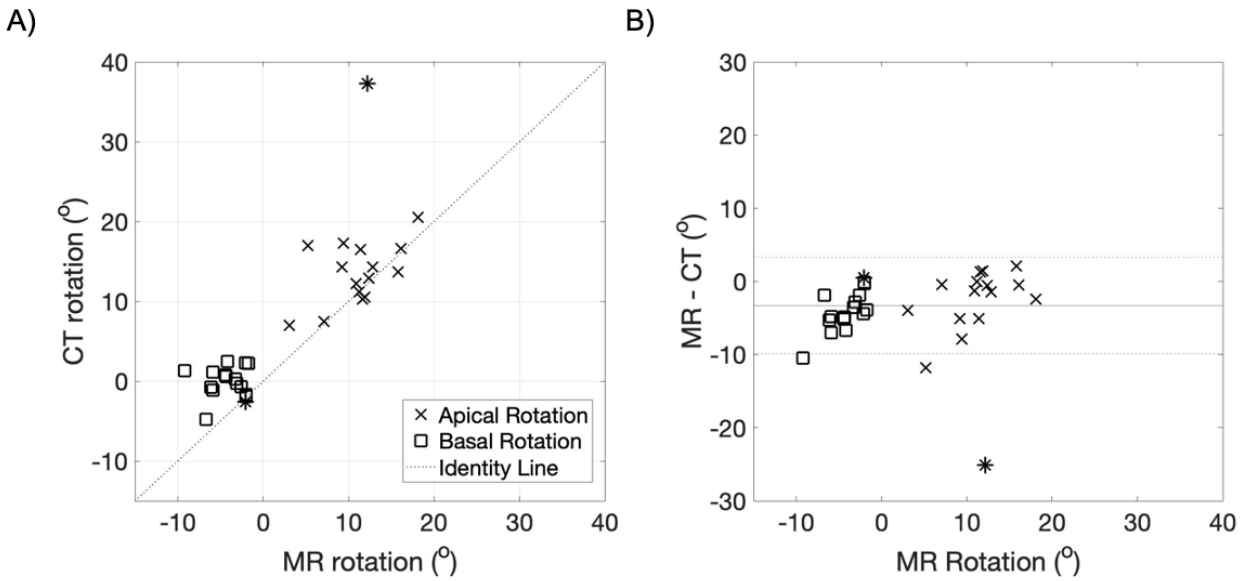

Figure 47. A) A plot comparing CMR-derived rotation on the x-axis and CT-derived rotation on the y-axis for two locations in each subject. The dashed line shows the identity line. B) Bland-Altman plot with the CMR rotation angle on the x-axis and the difference between the CMR and CT rotation angle on the y-axis. The mean difference (bias) is displayed as a solid horizontal line and ± 1.96*Standard Deviation of the difference are shown as horizonal dashed lines. Apical rotation is displayed as an 'x' and basal rotation is plotted as a square. The subject determined to be an outlier due to aberrant LV morphology leading to point-cloud registration failure is marked with an asterisk (*).

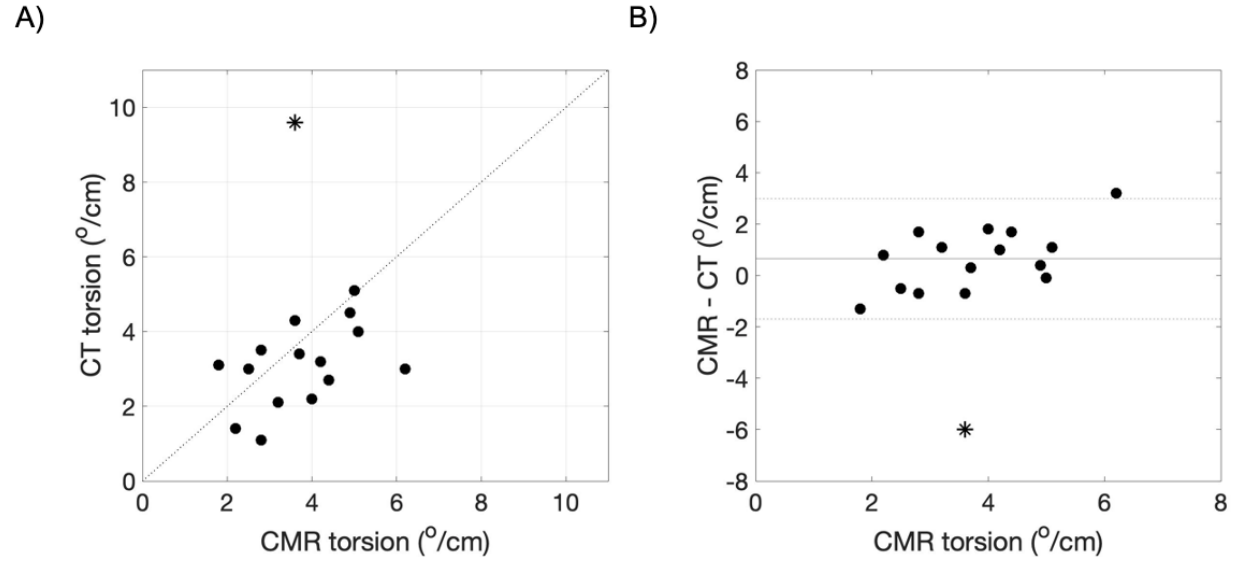

Figure 48. A) Correlation plot with CMR-derived torsion on the x-axis and CT-derived torsion on the y-axis. The identity line is shown as a dashed line. B) Bland-Altman plot with CMR-derived torsion on the x-axis and the difference between MR and CT-derived torsion on the y-axis. The mean difference (bias) is shown as a solid horizontal line and ± 1.96*Standard Deviation of the difference are shown as horizonal dashed lines. The subject identified as an outlier due to aberrant LV morphology leading to registration failure is shown as an asterisk (*).

7.3.2 Normal ranges of 4DCT-derived LV rotation and torsion

End-systolic LV apical rotation, basal rotation, twist, and torsion were evaluated in the subjects with normal systolic function. The normal ranges for these parameters across the 13 subjects are shown in Table 20. The reproducibility of LV torsion was also evaluated in half the subjects. Intra- and inter-observer variability for estimates of LV torsion were low as shown in Figure 49.

Table 20. Normal ranges for 4DCT-derived left ventricular rotation and torsion evaluated in 13 subjects with normal systolic function.

Apical rotation (°)	16.2 ± 7.6
Basal rotation (°)	-1.5 ± 3.6
Left ventricular twist (°)	17.7 ± 7.5
Left ventricular torsion (°/cm)	3.9 ± 1.8

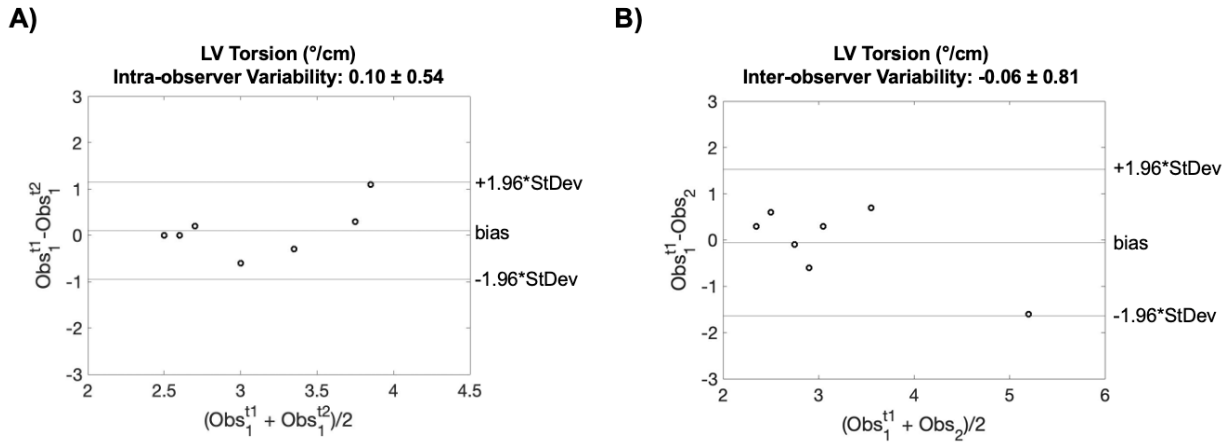

Figure 49. Bland-Altman plots showing A) intra-observer and B) inter-observer variability for 4DCT-derived left ventricular (LV) torsion in 7 subjects with normal LV systolic function.

7.4 Discussion

7.4.1 Main Findings

In this chapter we showed that there was moderate correlation and no significant difference between the CT and CMR-derived apical rotation and LV torsion measurements in the same subjects. The precision of the torsion estimate from CT was estimated to be ±1.2º/cm when

compared to the reference standard CMR tagging. In a cohort of subjects with normal LV systolic function. we computed a normal range for end-systolic 4DCT-derived LV torsion of 3.9º/cm±1.8º/cm. This is very similar to the normal value of LV torsion at end-systole as measured by CMR tagging, 3.9º/cm±1.3º/cm [130]. We also demonstrated that 4DCT-derived LV torsion is a highly reproducible metric. These results demonstrate the potential for 4DCT to provide prognostic functional information about LV torsion in addition to high quality anatomical data [130].

These results also demonstrate that the proposed algorithm for measuring LV torsion using 4DCT data can be performed on standard clinical images in a cohort of human subjects with varied cardiac function and image quality. The CT/MR cohort were not scanned specifically for our study, so we did not have control over image acquisition protocols or the characteristics of the subjects. Therefore, we had a fairly heterogenous population in regard to body mass index (BMI), normal or abnormal cardiac function as well as variable image quality and CT dose. Because of this, certain inclusion criteria were set in order to obtain a group of patients that would be appropriate for the pilot study for our proposed method for measuring endocardial torsion using 4DCT.

7.4.2 Limitations

As discussed in the previous chapter, comparison between two different imaging modalities has some limitations. For example, finding the corresponding locations from the 2D CMR data to regions within the 3D volumes in the CT data was subject to some uncertainty. The CTA was acquired within one heartbeat whereas the CMR images were averaged over several heartbeats. Also, the CMR data was acquired at end-expiration while the CTA data was acquired at end-inspiration which could lead to differences in cardiovascular loading conditions. Because of these factors, we would not expect to see a perfect correlation between the measurements from the two modalities. There was also an observed bias between the CMR and CT-derived basal rotation values. We hypothesize that this is caused by an underestimate of the rotation at

the base in the CT because there are very few fiducial markers on the endocardial surface in this region which are necessary for guiding the point-cloud registration algorithm.

In addition, point-cloud registration of the endocardial surface failed in one of the CT/MR subjects due to aberrant papillary muscle morphology. This is a weakness of the method because it only relies on the endocardial surface and does not have any transmural information. However, the proposed algorithm leverages the region of the CT volume where the greatest contrast and quantity of fiducial markers exists in CT images: the boundary between the endocardial tissue and the contrast-enhanced blood pool. The features on this surface are crucial for capturing the rotational motional of the LV [110]. In addition, use of this surface for analyzing cardiac function and the technique for extracting it from 4DCT volumes has been shown to yield high reproducibility [77], [90].

As discussed in the previous chapter, because of radiation dose concerns, a cohort of healthy controls is difficult to image with CT; therefore, subjects with normal LV function were assembled retrospectively based on information in the radiology report and 4DCT-derived GLS and EF. In addition, because 4DCT-derived torsion is more sensitive to poor image quality and the end-systolic blood pool size, additional constraints on EF, ESV, and CNR had to be added to the inclusion criteria. The normal values reported for the 13 subjects are what we can anticipated from patients commonly scanned at our institution. We also demonstrated in an initial reproducibility study in half these subjects that LV torsion is a reproducible metric with low inter- and intra-observer variability. However, larger studies need to be undertaken to validate these values and the reproducibility of the parameters.

7.5 Acknowledgments

Chapter 7, in part, is a reprint of the material as it is published in: Gabrielle M. Colvert, Juan E. Ortuño, W. Patricia Bandettini, Marcus Y. Chen, Maria J. Ledesma-Carbay, Elliot R. McVeigh. “4DCT-derived Endocardial Left Ventricular Torsion Correlated with CMR Tagging-

derived Torsion in the Same Subjects." in JACC: Cardiovascular Imaging (2020). The dissertation author was a primary author of this paper.

Chapters 7, is in part, is a reprint of the material as it is published in: Gabrielle M. Colvert, Ashish Manohar, Brendan T. Colvert, Andrew Schluchter, Francisco J. Contijoch, Elliot R. McVeigh. "Novel measurement of LV twist using 4DCT: quantifying accuracy as a function of image noise." in Proc. SPIE 10953, Medical Imaging 2019: Biomedical Applications in Molecular, Structural, and Functional Imaging. The dissertation author was a primary author of this paper.

Chapter 8: Conclusions and Future Directions

8.1 Summary of Work

This dissertation thoroughly investigated the development and application of novel methods for evaluating global and regional left ventricular (LV) function using 4D X-ray computed tomography (4DCT) data. First, we evaluate the accuracy and reproducibility of previously developed and validated metrics, like CT SQUEEZ, and newly proposed algorithms for measuring LV rotation, torsion, longitudinal strain, and circumferential strain through phantom experiments and cross-modality comparison studies. Then, we demonstrate the feasibility of these methods in patients with various cardiovascular disease states, such as mitral regurgitation (MR) and heart failure.

The first chapter reviewed the state of the field for minimally invasive percutaneous cardiac procedures, such as treatment of valvular heart disease with transcatheter valve replacement and treatment of heart failure with cardiac resynchronization therapy (CRT). It highlighted ways in which noninvasive imaging became an integral part of the success of the field. The review also discussed the current unmet clinical needs of these procedures and opportunities for 4DCT to make an impact on the clinical planning and outcomes of these interventions.

The second chapter introduced a method for measuring detailed 3D regional LV function in patients before and 1-month after transcatheter mitral valve implantation (TMVI) using 4DCT. We demonstrated that it was feasible to measure CT regional endocardial shortening (RS_{CT}) in subjects with highly abnormal regional LV function and highly abnormal geometry with high precision. Significant regional changes in RS_{CT} were observed following TMVI in all subjects, with high variability between the subjects evaluated. The regionally heterogeneous LV functional state of TMVI patients could not be fully described by changes, or lack thereof, in global parameters such as end-diastolic and end-systolic LV volumes, nor EF.

The third chapter described the development of the lead placement score (LPS) for 4DCT-guided CRT. In this chapter, we used 5-cross validated linear discriminant analysis (LDA) to

create three models for the two CT-based and one clinical definition of response to CRT in order to evaluate the prognostic value of 4DCT-derived metrics of LV shape, regional and global function, and dyssynchrony. The 4DCT-derived predictors evaluated were LV end-diastolic volume (EDV), LV end-systolic volume (ESV), $CURE_{tot}$, $CURE_{sys}$, TOS near the left lead, peak RS_{CT} near the left lead, endocardial end-diastolic (ED) sphericity (Sph_{ED}), and endocardial end-systolic (ES) sphericity (Sph_{ES}). In this initial proof-of-concept study, we showed using three example thresholds for the three LPS that we were able to retrospectively decrease the initial non-responder rates for all three definitions of response. The results from this study will be evaluated in future work using a separate validation cohort.

The fourth chapter introduced novel methods for evaluating LV endocardial function and discussed how they expanded on the technological foundations laid by the CT SQUEEZ method. The algorithms for measuring endocardial rotation and torsion, as well as regional endocardial longitudinal and circumferential strain from 4DCT data, were described in detail.

The fifth chapter described the validation of the 4DCT novel methods introduced in chapter 4 with phantom experiments. In this chapter, the accuracy and precision of endocardial LV rotation, torsion, regional longitudinal strain, and regional circumferential strain were quantified for different standard clinical scanning conditions producing variable image quality. Across a range of image quality (contrast-to-noise ratio 70.1 to 2.7), the absolute errors in rotation, torsion, and strain were low between the measured values and the ground truth values programmed into a 3D-printed endocardial LV phantom. We also demonstrated the high precision and reproducibility of these novel methods for measuring both global and regional LV deformation using 10 independent analyses at the lower limits of image quality achieved using standard clinical reconstruction protocols.

The sixth chapter demonstrated that the novel method for measuring 4DCT-derived regional strain introduced in chapter 4 and validated with phantom experiments in chapter 5 could be evaluated using standard clinical images in human subjects. There was good agreement

between the 4DCT- and CMR tagging-derived regional endocardial strain in the same subjects. Normal values of 4DCT-derived regional longitudinal, E_{ll}^{CT}, and circumferential, E_{cc}^{CT}, strain were measured in a cohort of subjects with normal LV function. This normal set of values was used to reproducibly identify abnormal segments in two subjects with previous MI.

The seventh chapter demonstrated that the novel method for measuring 4DCT-derived rotation and torsion introduced in chapter 4 and validated with phantom experiments in chapter 5 could be evaluated using standard clinical images in human subjects. This chapter describes the results of the first known study to perform a direct comparison between 4DCT and 2D CMR tagging-derived endocardial LV rotation and torsion in human subjects. Overall, there was moderate correlation between the two methods for measuring LV torsion and there was no significant difference between the measurements. Normal ranges of end-systolic 4DCT-derived apical rotation, basal rotation, LV twist, and LV torsion were also derived. The normal value of LV torsion was computed to be 3.9 º/cm ± 1.8º/cm which is similar to LV torsion measured by CMR tagging, or 3.9 º/cm ± 1.3º/cm [130]. We also demonstrate in a small cohort that 4DCT-derived LV torsion is a highly reproducible metric with low inter- and intra-observer variability. These results demonstrate the potential for cardiac CT to provide prognostic functional information about LV torsion in addition to high quality anatomical data.

Overall, in this dissertation we introduced, validated, and evaluated novel methods for quantifying regional and global LV function using contrast-enhanced 4DCT images in patients undergoing transcatheter-based procedures. We demonstrated that the previously validated CT SQUEEZ method could be measured in TMVI and CRT patients before and after both interventions. In these studies, we demonstrated that RS_{CT} (CT SQUEEZ-1) is a highly reproducible metric and has the potential to improve clinical planning and outcomes in these patient cohorts. In this dissertation, we also developed novel algorithms for measuring 4DCT-derived LV endocardial torsion and regional longitudinal and circumferential strain. We

demonstrated the high reproducibility of these metrics in both phantom experiments and in human subjects.

8.2. Future Directions and Outlook

In this dissertation, we demonstrated that 4DCT can be used to obtain reproducible estimates of both global and regional endocardial LV function. Combined with high resolution anatomical scans, these methods have the potential to allow for earlier diagnosis of cardiac diseases and the improvement of clinical planning and outcomes of cardiac procedures, especially minimally invasive interventions. As discussed in Chapter 1, 4DCT is already used in many structural heart procedures, like transcatheter aortic valve replacement (TAVR) and transcatheter mitral valve implantation (TMVI) to obtain measurements for device sizing [16], [24], [25]. Therefore, our proposed 4DCT methods for measuring endocardial deformation can be performed without extra radiation to understand the effects of valvular disease and device implantation on regional cardiac function. Future studies in larger cohorts will fully characterize the limits of detection of regional wall motion abnormalities in human subjects and evaluate the prognostic value of 4DCT-derived LV function as an alternative to CMR tagging and echocardiography. The novel 4DCT methods presented in this dissertation can be implemented immediately on many existing CT scanners as well as on existing datasets, retrospectively.

While we developed and tested the newly proposed algorithms for measuring 4DCT-derived LV torsion and regional longitudinal and circumferential strain introduced in chapter 4, we utilized and evaluated the prognostic value of CT SQUEEZ, a coordinate-free method that was previously created and validated by Dr. Elliot McVeigh and his lab. In chapter 2, we demonstrated that CT SQUEEZ is a highly reproducible metric which can be used to quantify regional endocardial function in TMVI patients with highly abnormal LV geometry and function. During this study we created a comprehensive LV function characterization report which was utilized to analyze changes in RS_{CT} (CT SQUEEZ-1) before and 1-month post TMVI in a standardized way

in 17 patients. Equipped with detailed maps of regional function, combined with clinical and procedure-related parameters, retrospective analysis of a larger patient cohort could provide an integrative approach for assessment of cardiac structure and function beyond EF and chamber volumes [31]. Recently, a study by Fukui *et al.* in 36 Tendyne TMVI patients showed that closer proximity of the epicardial pad to the true apex was predictive of favorable LV end-diastolic volume (EDV) reverse remodeling [131]. In our study with 17 patients and 4DCT-derived LV EDV, we could not confirm these results. However, in a much larger study, combining global functional analysis with our proposed regional evaluation of cardiac function using RS_{CT} could lead to a more precise understanding of the effect of MR and TMVI on regional LV function and remodeling and help determine which patients will benefit from valve replacement. The comprehensive report that we created can be used for this analysis.

We also showed the potential of 4DCT-derived metrics of LV shape, global and regional function, and dyssynchrony for predicting both CT- and clinically-based response to cardiac resynchronization therapy (CRT) through the development of the lead placement score (LPS) in an initial cohort of 44 patients. Example thresholds were chosen to demonstrate the potential for decreasing the non-response rate to CRT using the LPS while balancing the number of false positives and false negatives. In early studies characterizing regional myocardial strain in canines during ventricular pacing, it was shown using CMR tagging that strain is greatly reduced in the regions closest to the pacing site [132]. In 4/4 false positives from the ΔEF model and 5/5 false positives from the ΔESV model, placement of the left lead during CRT caused a large reduction in strain in the region near the pacing site. In these 9 patients, the rest of the heart did not compensate for this loss in function and therefore changes in EF and ESV did not reach the required response thresholds post CRT. However, 4/5 false negatives from the ΔEF model and 2/3 false negatives from the ΔESV model also lost function when the left lead was placed, but a remarkable increase in function on the opposite side of the heart occurred which compensated

for the loss and the patients were ultimately classified as responders. Future work will attempt to understand why some patients see this unexpected increase in function and others do not, perhaps by combining our 4DCT-metrics with measurements of myocardial viability from FDG PET [106], precise measurements of ED wall thickness, or other clinical parameters such as drug dosage. In addition, studies should be conducted in patients that do not respond to CRT and show this decrease in function or worsening dyssynchrony to see if they would benefit from turning the pacing off or from an alternative form of CRT which utilizes left bundle branch pacing [133].

As discussed, we also plan to evaluate the three LPSs that were created for the two CT-based definitions of response and the clinical response in a separate validation cohort. As shown in our results and discussed in previous studies, non-responder rates for CRT vary based on the definitions used, especially between functional and clinical responses. Consensus is needed for a composite definition which encompasses all aspects of therapeutic response such as strong indicators of correction of mechanical dyssynchrony, reverse remodeling, and freedom from heart failure-related hospitalization [15]. As shown in our study, an increase in the CURE index (indicating correction of mechanical dyssynchrony) and a decrease in endocardial sphericity (indicating reverse remodeling) was associated response to CRT. These parameters could be included in a composite definition of response and perhaps improve prediction capabilities as they are more direct indicators of LV function and remodeling compared to LV volumes and ejection fraction.

While the LPS models currently developed only include 4DCT-derived metrics, other parameters discussed in previous studies, such as the Seattle Heart Failure Model (SHFM-D) [59] and absence of scar as measured with late CT [50] and CMR [58] can be included in the models if they add prognostic value. In addition, we used linear discriminant analysis (LDA) to create these initial scores, but the prediction performance of more complex models like quadratic discriminant analysis (QDA) and support vector machines (SVMs), can also be evaluated [134].

Once the LPS have been validated in an independent cohort, a prospective trial can be run to determine if imaging-guided LV lead placement using the LPS decreases the fraction of non-responders compared to the standard of care implantation of a CRT device.

In the last four chapters of this dissertation, we introduce, validate, and establish normal ranges for 4DCT-derived endocardial LV rotation, torsion, and regional longitudinal and circumferential strain. After performing this extensive set of experiments in both phantoms and human subjects, we are confident that these novel methods can be used to build-on the results we achieved in the TMVI and CRT patients in chapters 2 and 3. An unmet clinical need in TMVI is being able to predict which patients will benefit from the treatment and those that will see a decline in function post intervention (as demonstrated in our feasibility study). In a recent study, Notomi *et al.* showed that in patients with nonischemic, chronic, secondary mitral regurgitation (MR) with a normal QRS width, 2-year survival and reverse remodeling post-surgical mitral valve replacement was associated with preserved LV torsion measured using speckle-tracking echocardiography prior to surgery [135]. While this was for surgical valve replacement, it indicates that LV torsion could be an important predictor of reverse remodeling in patients with severe MR.

The Tendyne device utilizes a tether anchored to the epicardial pad near the apex of the LV with a set tension level to hold the valve in place. At this time, no results have been reported which examine how this anchoring might affect the torsional motion and longitudinal shortening of the LV. Given the results discussed for surgical MR patients, future studies should examine if patients that do not respond to TMVI have reduced torsion prior to the intervention and if placement of the device negatively affects LV torsion given a specific tension value. As seen in this dissertation, however, LV torsion might not be a simple measurement in TMVI patients due to their abnormal LV geometry and highly heterogeneous regional function. Previous studies using CMR tagging have shown that regional differences in rotation do occur, even in hearts with normal LV function, and can be quantified [136]. Future work can be done to adapt the 4DCT

method proposed in this dissertation to measure regional LV rotation and evaluate this metric in TMVI patients and evaluate its prognostic value in other patient groups with wall motion abnormalities and abnormal geometries.

Again for surgical mitral valve replacement, Pandis *et al.* found that in patients with severe degenerative MR a higher LV global longitudinal strain, but not circumferential or radial strain, prior to intervention, signifying a subclinical maladaptive preload change, was associated with a significant loss of LV function after surgery [137]. Therefore, both global and regional longitudinal strain should also be quantified in TMVI patients. The novel 4DCT methods proposed in this dissertation can be used for this analysis. The results could be useful for optimizing the timing of the procedure before a severe maladaptive preload change occurs and for identifying appropriate candidates who will respond to device implantation given baseline LV torsion estimates.

For heart failure patients, recent studies have indicated that LV torsion shows immediate improvement in responders after CRT and is independently related to reverse remodeling at 6-months follow up [138]–[140]. These results indicate that LV torsion could have prognostic potential for predicting response to CRT. In addition, Helm *et al.* found using MRI tagging that circumferential strain was more sensitive to dyssynchrony in failing hearts than longitudinal strain [129]. While the results in Chapter 3 are promising, RS_{CT} encompasses both longitudinal and circumferential motion. Because of this, experiments should be performed to evaluate the sensitivity of 4DCT-derived circumferential strain vs. RS_{CT} for quantifying LV dyssynchrony. Further studies should be conducted using the novel methods proposed in this dissertation to evaluate the addition of 4DCT-derived LV torsion and circumferential strain for increasing the predictive power of the LPS.

Lastly, in this dissertation we demonstrated that contrast-enhanced 4DCT can be utilized to analyze LV function; however, the technique for extracting 3D deformation fields can also be applied to other structures in the heart. As shown in Figure 50, all chambers of the heart including

the LV, right ventricle (RV), left atrium (LA), right atrium, left atrial appendage (LAA), aorta, and pulmonary veins can be segmented from a contrast-enhanced 4DCT image and deformation of the surface can be quantified over the course of the cardiac cycle. For example, in patients with tricuspid regurgitation or pulmonary hypertension, global and regional function can be assessed in a highly reproducible manner [82]. The function of the LAA can also be quantified and used to predict thrombus formation and obtain precise measurements for LAA closure [141], [142].

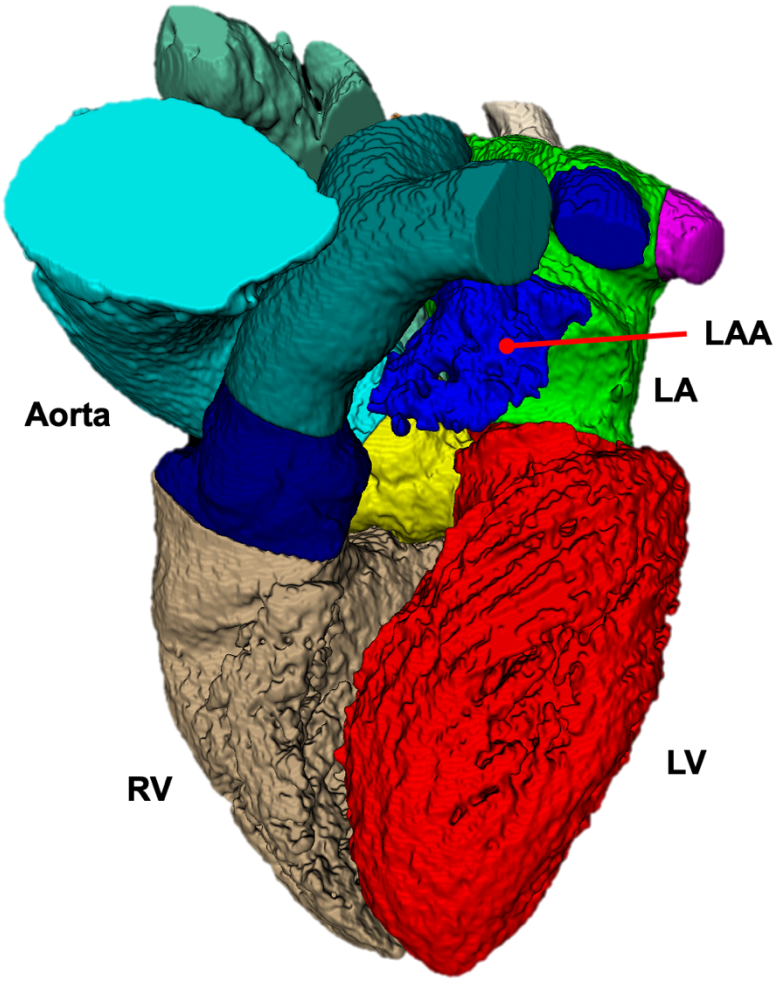

Figure 50. 3D full-heart segmentation from a 4DCT image at end-diastole, including the left ventricle (LV), right ventricle (RV), left atrium (LA), left atrial appendage (LAA), and aorta.

Aortic deformation over the course of the cardiac cycle can also be quantified and has the potential to gain a better understanding of the effects of aortic stenosis and valve replacement on

cardiovascular hemodynamics. Recent studies have shown that there is a significant decrease in atrial compliance observed after transcatheter aortic valve replacement (TAVR) which is associated with worse outcomes [143], [144]. Aortic compliance can be approximated noninvasively using the change in diameter and the pulse pressure and can therefore easily be quantified using 4DCT. A study can be performed to analyze aortic compliance before and after valve implantation to investigate the cause of the change in compliance. The results of this study could be used to inform future redesigns of existing valves or designs of new devices to counteract these effects in order to preserve or increase arterial compliance and improve outcomes.

LA function has also been shown to have prognostic value and can also be measured using 4DCT. Recently it has been shown that in patients with moderate to severe MR, LA function as measured with speckle-tracking echocardiography was associated with surgery-free survival [145]. The LA is central to the heart's adaptive mechanisms to chronic MR and therefore assessment of LA strain using 4DCT has potential for guiding if and when a patient should undergo valve repair or replacement. This is especially important as new TMVI devices are being developed which can be delivered through a puncture in the atrial septum, instead of transapically. Studies can be performed to evaluate LV and LA function to see if there is a difference in functional and clinical outcomes between the two delivery methods.

Overall, low dose, single heartbeat, contrast-enhanced cardiac 4DCT has the potential to make a significant impact on the fields of cardiovascular imaging and minimally invasive percutaneous interventions. The results presented throughout this dissertation strongly support this claim. This final chapter indicates that there are many more studies to be conducted that will benefit from the novel methods we have developed and validated.

References

[1] AHA, “Fact Sheet: Investing in Heart Disease and Stroke Research,” *Am. Hear. Assoc. Advocacy Dep.*, pp. 12–13, 2019.

[2] NIH, “Heart Disease - Fact Sheet,” no. October, 2010.

[3] Paul A. Heidenreich, Justin G. Trogdon, Olga A. Khavjou, Javed Butler, Kathleen Dracup, Michael D. Ezekowitz, Eric Andrew Finkelstein, Yuling Hong, S. Claiborne Johnston, Amit Khera, Donald M. Lloyd-Jones, Sue A. Nelson, Graham Nichol, Diane Orenstein, Peter W. F. Wilson, and Y. Joseph Woo, “Forecasting the future of cardiovascular disease in the United States: A policy statement from the American Heart Association,” *Circulation*, vol. 123, no. 8, pp. 933–944, 2011, doi: 10.1161/CIR.0b013e31820a55f5.

[4] Francesco Paneni, Candela Diaz Cañestro, Peter Libby, Thomas F. Lüscher, and Giovanni G. Camici, “The Aging Cardiovascular System: Understanding It at the Cellular and Clinical Levels,” *J. Am. Coll. Cardiol.*, vol. 69, no. 15, pp. 1952–1967, 2017, doi: 10.1016/j.jacc.2017.01.064.

[5] Susheel K. Kodali, Poonam Velagapudi, Rebecca T. Hahn, Dawn Abbott, and Martin B. Leon, “Valvular Heart Disease in Patients ≥80 Years of Age,” *J. Am. Coll. Cardiol.*, vol. 71, no. 18, pp. 2058–2072, 2018, doi: 10.1016/j.jacc.2018.03.459.

[6] Yuya Matsue, Kentaro Kamiya, Hiroshi Saito, Kazuya Saito, Yuki Ogasahara, Emi Maekawa, Masaaki Konishi, Takeshi Kitai, Kentaro Iwata, Kentaro Jujo, Hiroshi Wada, Takatoshi Kasai, Hirofumi Nagamatsu, Tetsuya Ozawa, Katsuya Izawa, Shuhei Yamamoto, Naoki Aizawa, Ryusuke Yonezawa, Kazuhiro Oka, Shin ichi Momomura, and Nobuyuki Kagiyama, “Prevalence and prognostic impact of the coexistence of multiple frailty domains in elderly patients with heart failure: the FRAGILE-HF cohort study,” *Eur. J. Heart Fail.*, vol. 22, no. 11, pp. 2112–2119, 2020, doi: 10.1002/ejhf.1926.

[7] Amy Groenewegen, Frans H. Rutten, Arend Mosterd, and Arno W. Hoes, “Epidemiology of heart failure,” *Eur. J. Heart Fail.*, vol. 22, no. 8, pp. 1342–1356, 2020, doi: 10.1002/ejhf.1858.

[8] Simon Yadgir, Catherine Owens Johnson, Victor Aboyans, Oladimeji M. Adebayo, Rufus Adesoji Adedoyin, Mohsen Afarideh, Fares Alahdab, Alaa Alashi, Vahid Alipour, Jalal Arabloo, Samad Azari, Celine M. Barthelemy, Catherine P. Benziger, Adam E. Berman, Ali Bijani, Juan J. Carrero, Félix Carvalho, Ahmad Daryani, Andre R. Durães, Alireza Esteghamati, Talha A. Farid, Farshad Farzadfar, Eduarda Fernandes, Irina Filip, Mohamed M. Gad, Samer Hamidi, Simon I. Hay, Olayinka Stephen Ilesanmi, Seyed Sina Naghibi Irvani, Mikk Jürisson, Amir Kasaeian, Andre Pascal Kengne, Abdur Rahman Khan, Adnan Kisa, Sezer Kisa, Dhaval Kolte, Navid Manafi, Amir Manafi, George A. Mensah, Erkin M. Mirrakhimov, Yousef Mohammad, Ali H. Mokdad, Ruxandra Irina Negoi, Huong Lan Thi Nguyen, Trang Huyen Nguyen, Molly R. Nixon, Catherine M. Otto, Shanti Patel, Thomas Pilgrim, Amir Radfar, David Laith Rawaf, Salman Rawaf, Wasiq Faraz Rawasia, Aziz Rezapour, Leonardo Roever, Anas M. Saad, Seyedmohammad Saadatagah, Subramanian Senthilkumaran, Karen Sliwa, Berhe Etsay Tesfay, Bach Xuan Tran, Irfan Ullah, Muthiah Vaduganathan, Tommi Juhani Vasankari, Charles D. A. Wolfe, Naohiro Yonemoto, and Gregory A. Roth, “Global, Regional, and National Burden of Calcific Aortic Valve and Degenerative Mitral Valve Diseases, 1990-2017,” *Circulation*, pp. 1670–1680, 2020, doi: 10.1161/CIRCULATIONAHA.119.043391.

[9] Clyde W. Yancy, Mariell Jessup, Biykem Bozkurt, Javed Butler, Donald E. Casey, Monica M. Colvin, Mark H. Drazner, Gerasimos S. Filippatos, Gregg C. Fonarow, Michael M.

Givertz, Steven M. Hollenberg, Jo Ann Lindenfeld, Frederick A. Masoudi, Patrick E. McBride, Pamela N. Peterson, Lynne Warner Stevenson, and Cheryl Westlake, “2017 ACC/AHA/HFSA Focused Update of the 2013 ACCF/AHA Guideline for the Management of Heart Failure: A Report of the American College of Cardiology/American Heart Association Task Force on Clinical Practice Guidelines and the Heart Failure Society of Amer,” *Circulation*, vol. 136, no. 6, pp. e137–e161, 2017, doi: 10.1161/CIR.0000000000000509.

[10] Stephen J. Greene, Javed Butler, Nancy M. Albert, Adam D. DeVore, Puza P. Sharma, Carol I. Duffy, C. Larry Hill, Kevin McCague, Xiaojuan Mi, J. Herbert Patterson, John A. Spertus, Laine Thomas, Fredonia B. Williams, Adrian F. Hernandez, and Gregg C. Fonarow, “Medical Therapy for Heart Failure With Reduced Ejection Fraction: The CHAMP-HF Registry,” *J. Am. Coll. Cardiol.*, vol. 72, no. 4, pp. 351–366, 2018, doi: 10.1016/j.jacc.2018.04.070.

[11] Berto J. Bouma and Barbara J. M. Mulder, “Changing Landscape of Congenital Heart Disease,” *Circ. Res.*, vol. 120, no. 6, pp. 908–922, 2017, doi: 10.1161/CIRCRESAHA.116.309302.

[12] Mario Carminati, Mauro Agnifili, Carmelo Arcidiacono, Nedy Brambilla, Claudio Bussadori, Gianfranco Butera, Massimo Chessa, Mohammed Heles, Angelo Micheletti, Diana G. Negura, Luciane Piazza, Antonio Saracino, Luca Testa, Maurizio Tusa, and Francesco Bedogni, “Role of imaging in interventions on structural heart disease,” *Expert Rev. Cardiovasc. Ther.*, vol. 11, no. 12, pp. 1659–1676, 2013, doi: 10.1586/14779072.2013.854166.

[13] Clifford J. Kavinsky, Marie-France Poulin, and Michael J. Mack, “Training in Structural Heart Disease: Call to Action,” *Circulation*, vol. 138, no. 3, pp. 225–228, 2018, doi: 10.1161/circulationaha.117.029072.

[14] Kevin Vernooy, Caroline J. M. Van Deursen, Marc Strik, and Frits W. Prinzen, “Strategies to improve cardiac resynchronization therapy,” *Nat. Rev. Cardiol.*, vol. 11, no. 8, pp. 481–493, 2014, doi: 10.1038/nrcardio.2014.67.

[15] Claude Daubert, Nathalie Behar, Raphaël P. Martins, Philippe Mabo, and Christophe Leclercq, “Avoiding non-responders to cardiac resynchronization therapy: A practical guide,” *Eur. Heart J.*, vol. 38, no. 19, pp. 1463–1472, 2017, doi: 10.1093/eurheartj/ehw270.

[16] Philipp Blanke, Jonathan R. Weir-McCall, Stephan Achenbach, Victoria Delgado, Jörg Hausleiter, Jilaihawi Hasan, Mohamed Marwan, Bjarne L. Nørgaard, Niccolo Piazza, Paul Schoenhagen, and Jonathon A. Leipsic, “Computed Tomography Imaging in the Context of Transcatheter Aortic Valve Implantation (TAVI)/Transcatheter Aortic Valve Replacement (TAVR),” *JACC Cardiovasc. Imaging*, vol. 12, no. 1, pp. 1–24, 2019, doi: 10.1016/j.jcmg.2018.12.003.

[17] Michael J. Mack, Martin B. Leon, Vinod H. Thourani, Raj Makkar, Susheel K. Kodali, Mark Russo, Samir R. Kapadia, S. Chris Malaisrie, David J. Cohen, Phillippe Pibarot, Jonathon Leipsic, Rebecca T. Hahn, Philipp Blanke, Mathew R. Williams, James M. McCabe, David L. Brown, Vasilis Babaliaros, Scott Goldman, Wilson Y. Szeto, Philippe Genereux, Ashish Pershad, Stuart J. Pocock, Maria C. Alu, John G. Webb, and Craig R. Smith, “Transcatheter Aortic-Valve Replacement with a Balloon-Expandable Valve in Low-Risk Patients,” *N. Engl. J. Med.*, p. NEJMoa1814052, 2019, doi: 10.1056/NEJMoa1814052.

[18] Zouhair Rahhab, Nahid El Faquir, Didier Tchetche, Victoria Delgado, Susheel Kodali, E. Mara Vollema, Jeroen Bax, Martin B. Leon, and Nicolas M. Van Mieghem, “Expanding the indications for transcatheter aortic valve implantation,” *Nat. Rev. Cardiol.*, vol. 17, no. 2, pp. 75–84, 2020, doi: 10.1038/s41569-019-0254-6.

[19] Davide Capodanno, Anna S. Petronio, Bernard Prendergast, Helene Eltchaninoff, Alec Vahanian, Thomas Modine, Patrizio Lancellotti, Lars Sondergaard, Peter F. Ludman, Corrado Tamburino, Nicolò Piazza, Jane Hancock, Julinda Mehilli, Robert A. Byrne, Andreas Baumbach, Arie Pieter Kappetein, Stephan Windecker, Jeroen Bax, and Michael Haude, “Standardized definitions of structural deterioration and valve failure in assessing long-term durability of transcatheter and surgical aortic bioprosthetic valves: A consensus statement from the European Association of Percutaneous Cardiovascular Interven,” *Eur. J. Cardio-thoracic Surg.*, vol. 52, no. 3, pp. 408–417, 2017, doi: 10.1093/EJCTS/EZX244.

[20] Tomohiko Taniguchi, Takeshi Morimoto, Hiroki Shiomi, Kenji Ando, Norio Kanamori, Koichiro Murata, Takeshi Kitai, Yuichi Kawase, Chisato Izumi, Makoto Miyake, Hirokazu Mitsuoka, Masashi Kato, Yutaka Hirano, Shintaro Matsuda, Kazuya Nagao, Tsukasa Inada, Tomoyuki Murakami, Yasuyo Takeuchi, Keiichiro Yamane, Mamoru Toyofuku, Mitsuru Ishii, Eri Minamino-Muta, Takao Kato, Moriaki Inoko, Tomoyuki Ikeda, Akihiro Komasa, Katsuhisa Ishii, Kozo Hotta, Nobuya Higashitani, Yoshihiro Kato, Yasutaka Inuzuka, Chiyo Maeda, Toshikazu Jinnai, Yuko Morikami, Ryuzo Sakata, and Takeshi Kimura, “Initial Surgical Versus Conservative Strategies in Patients with Asymptomatic Severe Aortic Stenosis,” *J. Am. Coll. Cardiol.*, vol. 66, no. 25, pp. 2827–2838, 2015, doi: 10.1016/j.jacc.2015.10.001.

[21] Frederick L. Grover, Sreekanth Vemulapalli, John D. Carroll, Fred H. Edwards, Michael J. Mack, Vinod H. Thourani, Ralph G. Brindis, David M. Shahian, Carlos E. Ruiz, Jeffrey P. Jacobs, George Hanzel, Joseph E. Bavaria, E. Murat Tuzcu, Eric D. Peterson, Susan Fitzgerald, Matina Kourtis, Joan Michaels, Barbara Christensen, William F. Seward, Kathleen Hewitt, and David R. Holmes, “2016 Annual Report of The Society of Thoracic Surgeons/American College of Cardiology Transcatheter Valve Therapy Registry,” *J. Am. Coll. Cardiol.*, vol. 69, no. 10, pp. 1215–1230, 2017, doi: 10.1016/j.jacc.2016.11.033.

[22] Paul N. Fiorilli and Howard C. Herrmann, “Transcatheter Mitral Valve Replacement: Rationale and Current Status,” *Annu. Rev. Med.*, vol. 71, pp. 249–261, 2020, doi: 10.1146/annurev-med-051418-060028.

[23] Alison Duncan, “Transcatheter Mitral Valve Replacement The Tendyne Device and Preprocedural Imaging,” in *Transcatheter Mitral Valve Therapies*, R. Waksman and T. Rogers, Eds. John Wiley & Sons Ltd, 2021, pp. 261–274.

[24] David W. M. Muller, Robert Saeid Farivar, Paul Jansz, Richard Bae, Darren Walters, Andrew Clarke, Paul A. Grayburn, Robert C. Stoler, Gry Dahle, Kjell A. Rein, Marty Shaw, Gregory M. Scalia, Mayra Guerrero, Paul Pearson, Samir Kapadia, Marc Gillinov, Augusto Pichard, Paul Corso, Jeffrey Popma, Michael Chuang, Philipp Blanke, Jonathon Leipsic, Paul Sorajja, David Muller, Paul Jansz, Marty Shaw, Mark Conellan, Roberto Spina, Wesley Pedersen, Paul Sorajja, R. Saeid Farivar, Richard Bae, Benjamin Sun, Darren Walters, Andrew Clarke, Gregory Scalia, Paul Grayburn, Robert Stoler, Robert Hebeler, Gry Dahle, Kjell Arne Rein, Arnt Fiane, Maya Guerrero, Paul Pearson, Ted Feldman, Michael Salinger, Steven Smart, Samir Kapadia, Marc Gillinov, Stephanie Mick, Amar Krishnaswamy, Augusto Pichard, Paul Corso, Michael Chuang, Jeffrey Popma, Jonathon Leipsic, Philippe Blanke, John Carroll, Isaac George, Emil Missov, and Andrew Kiser, “Transcatheter Mitral Valve Replacement for Patients With Symptomatic Mitral Regurgitation: A Global Feasibility Trial,” *J. Am. Coll. Cardiol.*, vol. 69,

no. 4, pp. 381–391, 2017, doi: 10.1016/j.jacc.2016.10.068.

[25] Philipp Blanke, Christopher Naoum, John Webb, Danny Dvir, Rebecca T. Hahn, Paul Grayburn, Robert R. Moss, Mark Reisman, Nicolo Piazza, and Jonathon Leipsic, “Multimodality imaging in the context of transcatheter mitral valve replacement establishing consensus among modalities and disciplines,” *JACC Cardiovasc. Imaging*, vol. 8, no. 10, pp. 1191–1208, 2015, doi: 10.1016/j.jcmg.2015.08.004.

[26] Paul Sorajja, Neil Moat, Vinay Badhwar, Darren Walters, Gaetano Paone, Brian Bethea, Richard Bae, Gry Dahle, Mubashir Mumtaz, Paul Grayburn, Samir Kapadia, Vasilis Babaliaros, Mayra Guerrero, Lowell Satler, Vinod Thourani, Francesco Bedogni, David Rizik, Paolo Denti, Nicolas Dumonteil, Thomas Modine, Ajay Sinhal, Michael L. Chuang, Jeffrey J. Popma, Philipp Blanke, Jonathon Leipsic, and David Muller, “Initial Feasibility Study of a New Transcatheter Mitral Prosthesis: The First 100 Patients,” *J. Am. Coll. Cardiol.*, vol. 73, no. 11, pp. 1250–1260, 2019, doi: 10.1016/j.jacc.2018.12.066.

[27] Philipp Blanke, Danny Dvir, Anson Cheung, Robert A. Levine, Christopher Thompson, John G. Webb, and Jonathon Leipsic, “Mitral annular evaluation with CT in the context of transcatheter mitral valve replacement,” *JACC Cardiovasc. Imaging*, vol. 8, no. 5, pp. 612–615, 2015, doi: 10.1016/j.jcmg.2014.07.028.

[28] Philipp Blanke, Danny Dvir, Anson Cheung, Jian Ye, Robert A. Levine, Bruce Precious, Adam Berger, Dion Stub, Cameron Hague, Darra Murphy, Christopher Thompson, Brad Munt, Robert Moss, Robert Boone, David Wood, Gregor Pache, John Webb, and Jonathon Leipsic, “A simplified D-shaped model of the mitral annulus to facilitate CT-based sizing before transcatheter mitral valve implantation,” *J. Cardiovasc. Comput. Tomogr.*, vol. 8, no. 6, pp. 459–467, 2014, doi: 10.1016/j.jcct.2014.09.009.

[29] Edward D. Nicol, Bjarne L. Norgaard, Philipp Blanke, Amir Ahmadi, Jonathon Weir-McCall, Pal Maurovich Horvat, Kelly Han, Jeroen J. Bax, and Jonathon Leipsic, “The Future of Cardiovascular Computed Tomography: Advanced Analytics and Clinical Insights,” *JACC Cardiovasc. Imaging*, vol. 12, no. 6, pp. 1058–1072, 2019, doi: 10.1016/j.jcmg.2018.11.037.

[30] Rick A. Nishimura, Catherine M. Otto, Robert O. Bonow, Blase A. Carabello, John P. Erwin, Lee A. Fleisher, Hani Jneid, Michael J. Mack, Christopher J. McLeod, Patrick T. O’Gara, Vera H. Rigolin, Thoralf M. Sundt, and Annemarie Thompson, *2017 AHA/ACC Focused Update of the 2014 AHA/ACC Guideline for the Management of Patients with Valvular Heart Disease: A Report of the American College of Cardiology/American Heart Association Task Force on Clinical Practice Guidelines*, vol. 135, no. 25. 2017.

[31] Maja Cikes and Scott D. Solomon, “Beyond ejection fraction: An integrative approach for assessment of cardiac structure and function in heart failure,” *Eur. Heart J.*, vol. 37, no. 21, pp. 1642–1650, 2016, doi: 10.1093/eurheartj/ehv510.

[32] Otto A. Smiseth, Hans Torp, Anders Opdahl, Kristina H. Haugaa, and Stig Urheim, “Myocardial strain imaging: How useful is it in clinical decision making?,” *Eur. Heart J.*, vol. 37, no. 15, pp. 1196-1207b, 2016, doi: 10.1093/eurheartj/ehv529.

[33] Daniela Cardinale, Alessandro Colombo, Giulia Bacchiani, Ines Tedeschi, Carlo A. Meroni, Fabrizio Veglia, Maurizio Civelli, Giuseppina Lamantia, Nicola Colombo, Giuseppe Curigliano, Cesare Fiorentini, and Carlo M. Cipolla, “Early detection of anthracycline cardiotoxicity and improvement with heart failure therapy,” *Circulation*, vol. 131, no. 22, pp. 1981–1988, 2015, doi: 10.1161/CIRCULATIONAHA.114.013777.

[34] Kashif Kalam, Petr Otahal, and Thomas H. Marwick, “Prognostic implications of global LV

dysfunction: A systematic review and meta-analysis of global longitudinal strain and ejection fraction," *Heart*, vol. 100, no. 21, pp. 1673–1680, 2014, doi: 10.1136/heartjnl-2014-305538.

[35] Vasileios Kamperidis, Nina Ajmone Marsan, Victoria Delgado, and Jeroen J. Bax, "Left ventricular systolic function assessment in secondary mitral regurgitation: Left ventricular ejection fraction vs. speckle tracking global longitudinal strain," *Eur. Heart J.*, vol. 37, no. 10, pp. 811–816, 2016, doi: 10.1093/eurheartj/ehv680.

[36] Sara Hungerford, Nicole Bart, Paul Jansz, Sharon Kay, Sam Emmanuel, Mayooran Namasivayam, Gry Dahle, Alison Duncan, Christopher Hayward, and David W. M. Muller, "Improved right ventricular function following transapical transcatheter mitral valve implantation for severe mitral regurgitation," *IJC Hear. Vasc.*, vol. 32, p. 100687, 2021, doi: 10.1016/j.ijcha.2020.100687.

[37] Marc André Bouchard, Claudia Côté-Laroche, and Jonathan Beaudoin, "Multi-Modality Imaging in the Evaluation and Treatment of Mitral Regurgitation," *Curr. Treat. Options Cardiovasc. Med.*, vol. 19, no. 12, 2017, doi: 10.1007/s11936-017-0589-4.

[38] William T. Abraham and David L. Hayes, "Cardiac Resynchronization Therapy for Heart Failure," *Circulation*, vol. 108, no. 21, pp. 2596–2603, 2003, doi: 10.1161/01.CIR.0000096580.26969.9A.

[39] Anthony S. L. Tang, George A. Wells, Mario Talajic, Malcolm O. Arnold, Robert Sheldon, Stuart Connolly, Stefan H. Hohnloser, Graham Nichol, David H. Birnie, John L. Sapp, Raymond Yee, Jeffrey S. Healey, and Jean L. Rouleau, "Cardiac-Resynchronization Therapy for Mild-to-Moderate Heart Failure," *N. Engl. J. Med.*, vol. 363, no. 25, pp. 2385–2395, 2010.

[40] Arthur J. Moss, W. Jackson Hall, David S. Cannom, Helmut Klein, Mary W. Brown, James P. Daubert, N. A. Mark III Estes, Elyse Foster, Henry Greenberg, Steven L. Higgins, Marc A. Pfeffer, Scott D. Solomon, David Wilber, and Wojciech Zareba, "Cardiac-Resynchronization Therapy for the Prevention of Heart-Failure Events," *N. Engl. J. Med.*, vol. 361, no. 14, pp. 1329–1338, 2009, [Online]. Available: https://www.nejm.org/doi/pdf/10.1056/NEJMoa0900212?articleTools=true.

[41] John M. Aalen, Erwan Donal, Camilla K. Larsen, Jürgen Duchenne, Mathieu Lederlin, Marta Cvijic, Arnaud Hubert, Gabor Voros, Christophe Leclercq, Jan Bogaert, Einar Hopp, Jan Gunnar Fjeld, Martin Penicka, Cecilia Linde, Odd O. Aalen, Erik Kongsgård, Elena Galli, Jens Uwe Voigt, and Otto A. Smiseth, "Imaging predictors of response to cardiac resynchronization therapy: Left ventricular work asymmetry by echocardiography and septal viability by cardiac magnetic resonance," *Eur. Heart J.*, vol. 41, no. 39, pp. 3813–3823, 2020, doi: 10.1093/eurheartj/ehaa603.

[42] Anders Sommer, Mads Brix Kronborg, Steen Hvitfeldt Poulsen, Morten Böttcher, Bjarne Linde Nørgaard, Kirsten Bouchelouche, Peter Thomas Mortensen, Christian Gerdes, and Jens Cosedis Nielsen, "Empiric versus imaging guided left ventricular lead placement in cardiac resynchronization therapy (ImagingCRT): study protocol for a randomized controlled trial.," *Trials*, vol. 14, pp. 1–9, 2013, doi: 10.1186/1745-6215-14-113.

[43] Daniel A. Auger, Kenneth C. Bilchick, Jorge A. Gonzalez, Sophia X. Cui, Jeffrey W. Holmes, Christopher M. Kramer, Michael Salerno, and Frederick H. Epstein, "Imaging left-ventricular mechanical activation in heart failure patients using cine DENSE MRI: Validation and implications for cardiac resynchronization therapy," *J. Magn. Reson. Imaging*, vol. 46, no. 3, pp. 887–896, 2017, doi: 10.1002/jmri.25613.

[44] Kenneth C. Bilchick, Veronica Dimaano, Katherine C. Wu, Robert H. Helm, Robert G. Weiss, Joao A. Lima, Ronald D. Berger, Gordon F. Tomaselli, David A. Bluemke, Henry R. Halperin, Theodore Abraham, David A. Kass, and Albert C. Lardo, “Cardiac Magnetic Resonance Assessment of Dyssynchrony and Myocardial Scar Predicts Function Class Improvement Following Cardiac Resynchronization Therapy,” *JACC Cardiovasc. Imaging*, vol. 1, no. 5, pp. 561–568, 2008, doi: 10.1016/j.jcmg.2008.04.013.

[45] Justin Gould, Baldeep S. Sidhu, Benjamin J. Sieniewicz, Bradley Porter, Angela W. C. Lee, Orod Razeghi, Jonathan M. Behar, Vishal Mehta, Mark K. Elliott, Daniel Toth, Ulrike Haberland, Reza Razavi, Ronak Rajani, Steven Niederer, and Christopher A. Rinaldi, “Feasibility of intraprocedural integration of cardiac CT to guide left ventricular lead implantation for CRT upgrades,” *J. Cardiovasc. Electrophysiol.*, vol. 32, no. 3, pp. 802–812, 2021, doi: 10.1111/jce.14896.

[46] Frank Ruschitzka, William T. Abraham, Jagmeet P. Singh, Jeroen J. Bax, Jeffrey S. Borer, Josep Brugada, Kenneth Dickstein, Ian Ford, John Gorcsan III, Daniel Gras, Henry Krum, Peter Sogaard, and Johannes Holzmeister, “Cardiac-resynchronization therapy in heart failure with a narrow QRS complexe,” *N. Engl. J. Med.*, vol. 369, no. 15, pp. 1395–1405, 2013, doi: 10.1056/nejmoa1306687.

[47] Victoria Delgado and Jeroen J. Bax, “Assessment of systolic dyssynchrony for cardiac resynchronization therapy is clinically useful,” *Circulation*, vol. 123, no. 6, pp. 640–655, 2011, doi: 10.1161/CIRCULATIONAHA.110.954404.

[48] Raphael K. Sung and Elyse Foster, “Assessment of Systolic Dyssynchrony for Cardiac Resynchronization Therapy Is Not Clinically Useful,” *Circulation*, vol. 123, no. 6, pp. 656–662, 2011, doi: 10.1161/CIRCULATIONAHA.110.954420.

[49] Rasmus Borgquist, Marcus Carlsson, Hanna Markstad, Anna Werther-Evaldsson, Ellen Ostenfeld, Anders Roijer, and Zoltan Bakos, “Cardiac Resynchronization Therapy Guided by Echocardiography, MRI, and CT Imaging: A Randomized Controlled Study,” *JACC Clin. Electrophysiol.*, vol. 6, no. 10, pp. 1300–1309, 2020, doi: 10.1016/j.jacep.2020.05.011.

[50] Daniel Benjamin Fyenbo, Anders Sommer, J. Tobias Kühl, Klaus F. Kofoed, Bjarne L. Nørgaard, Mads B. Kronborg, Kirsten Bouchelouche, and Jens C. Nielsen, “Transmural Myocardial Scar Assessed by Cardiac Computed Tomography: Predictor of Echocardiographic Versus Clinical Response to Cardiac Resynchronization Therapy?,” *J. Comput. Assist. Tomogr.*, vol. 43, no. 2, pp. 312–316, 2019, doi: 10.1097/RCT.0000000000000824.

[51] Christophe Leclercq, Owen Faris, Richard Tunin, Jennifer Johnson, Ritsuchi Kato, Frank Evans, Julio Spinelli, Henry Halperin, Elliot McVeigh, and David A. Kass, “Systolic improvement and mechanical resynchronization does not require electrical synchrony in the dilated failing heart with left bundle-branch block,” *Circulation*, vol. 106, no. 14, pp. 1760–1763, 2002, doi: 10.1161/01.CIR.0000035037.11968.5C.

[52] Elliot McVeigh, Owen Faris, Dan Ennis, Patrick Helm, and Frank Evans, “Electromechanical mapping with MRI tagging and epicardial sock electrodes,” *J. Electrocardiol.*, vol. 35, no. 4, pp. 61–64, 2002, doi: 10.1054/jelc.2002.37156.

[53] Owen P. Faris, Frank J. Evans, Daniel B. Ennis, Patrick A. Helm, Joni L. Taylor, A. Scott Chesnick, Michael A. Guttman, Cengizhan Ozturk, and Elliot R. McVeigh, “Novel technique for cardiac electromechanical mapping with magnetic resonance imaging tagging and an epicardial electrode sock,” *Ann. Biomed. Eng.*, vol. 31, no. 4, pp. 430–

440, 2003, doi: 10.1114/1.1560618.

[54] Elliot R. Mcveigh, Frits W. Prinzen, Bradley T. Wyman, Joshua E. Tsitlik, Henry R. Halperin, and William C. Hunter, “Paced Heart with Tagged MRI,” *Imaging*, 1998.

[55] Elliot McVeigh, “Measuring mechanical function in the failing heart,” *J. Electrocardiol.*, vol. 39, no. 4 SUPPL., pp. 24–27, 2006, doi: 10.1016/j.jelectrocard.2006.05.031.

[56] Alban GALLARD, Auriane BIDAUT, Arnaud HUBERT, Elif SADE, Sylvestre MARECHAUX, Marta Sitges, Jadranka SEPAROVIC-HANZEVACKI, Virginie LE. ROLLE, Elena GALLI, Alfredo HERNANDEZ, and Erwan DONAL, “Characterization of responder profiles for cardiac resynchronization therapy through unsupervised clustering of clinical and strain data,” *J. Am. Soc. Echocardiogr.*, 2021, doi: 10.1016/j.echo.2021.01.019.

[57] Quynh A. Truong, Jackie Szymonifka, Michael H. Picard, Wai ee Thai, Bryan Wai, Jim W. Cheung, E. Kevin Heist, Udo Hoffmann, and Jagmeet P. Singh, “Utility of dual-source computed tomography in cardiac resynchronization therapy—DIRECT study,” *Hear. Rhythm*, vol. 15, no. 8, pp. 1206–1213, 2018, doi: 10.1016/j.hrthm.2018.03.020.

[58] Kenneth C. Bilchick, Sujith Kuruvilla, Yasmin S. Hamirani, Raghav Ramachandran, Samantha A. Clarke, Katherine M. Parker, George J. Stukenborg, Pamela Mason, John D. Ferguson, J. Randall Moorman, Rohit Malhotra, J. Michael Mangrum, Andrew E. Darby, John Dimarco, Jeffrey W. Holmes, Michael Salerno, Christopher M. Kramer, and Frederick H. Epstein, “Impact of mechanical activation, scar, and electrical timing on cardiac resynchronization therapy response and clinical outcomes,” *J. Am. Coll. Cardiol.*, vol. 63, no. 16, pp. 1657–1666, 2014, doi: 10.1016/j.jacc.2014.02.533.

[59] Kenneth C. Bilchick, Daniel A. Auger, Mohammad Abdishektaei, Roshin Mathew, Min Woong Sohn, Xiaoying Cai, Changyu Sun, Aditya Narayan, Rohit Malhotra, Andrew Darby, J. Michael Mangrum, Nishaki Mehta, John Ferguson, Sula Mazimba, Pamela K. Mason, Christopher M. Kramer, Wayne C. Levy, and Frederick H. Epstein, “CMR DENSE and the Seattle Heart Failure Model Inform Survival and Arrhythmia Risk After CRT,” *JACC Cardiovasc. Imaging*, vol. 13, no. 4, pp. 924–936, 2020, doi: 10.1016/j.jcmg.2019.10.017.

[60] Eugene S. Chung, Angel R. Leon, Luigi Tavazzi, Jing Ping Sun, Petros Nihoyannopoulos, John Merlino, William T. Abraham, Stefano Ghio, Christophe Leclercq, Jeroen J. Bax, Cheuk Man Yu, John Gorcsan, Martin St John Sutton, Johan De Sutter, and Jaime Murillo, “Results of the predictors of response to crt (prospect) trial,” *Circulation*, vol. 117, no. 20, pp. 2608–2616, 2008, doi: 10.1161/CIRCULATIONAHA.107.743120.

[61] Fakhar Khan, Mumohan Virdee, Christopher Palmer, Peter Pugh, Denis O’Halloran, Maros Elsik, Philip A. Read, David Begley, Simon P. Fynn, and David P. Dutka, “Targeted Left Ventricular Lead Placement to Guide Cardiac Resynchronization Therapy,” *JACC*, vol. 59, no. 17, pp. 1509–1518, 2012, doi: 10.1016/j.jacc.2011.12.030.

[62] Fakhar Z. Khan, Mumohan S. Virdee, Christopher R. Palmer, Peter J. Pugh, Denis O’Halloran, Maros Elsik, Philip A. Read, David Begley, Simon P. Fynn, and David P. Dutka, “Targeted left ventricular lead placement to guide cardiac resynchronization therapy: The TARGET study: A randomized, controlled trial,” *J. Am. Coll. Cardiol.*, vol. 59, no. 17, pp. 1509–1518, 2012, doi: 10.1016/j.jacc.2011.12.030.

[63] Robin J. Taylor, Fraz Umar, Jonathan R. Panting, Berthold Stegemann, and Francisco Leyva, “Left ventricular lead position, mechanical activation, and myocardial scar in relation to left ventricular reverse remodeling and clinical outcomes after cardiac resynchronization therapy: A feature-tracking and contrast-enhanced cardiovascular

magnetic r," *Hear. Rhythm*, vol. 13, no. 2, pp. 481–489, 2016, doi: 10.1016/j.hrthm.2015.10.024.

[64] Oana Mirea, Efstathios D. Pagourelias, Jurgen Duchenne, Jan Bogaert, James D. Thomas, Luigi P. Badano, Jens Uwe Voigt, Jamie Hamilton, Stefano Pedri, Peter Lysyansky, Gunnar Hansen, Yasuhiro Ito, Tomoaki Chono, Jane Vogel, David Prater, Sungwook Park, Jin Yong Lee, Helene Houle, Bogdan Georgescu, Rolf Baumann, Bernhard Mumm, Yashuhiko Abe, and Willem Gorissen, "Variability and Reproducibility of Segmental Longitudinal Strain Measurement: A Report From the EACVI-ASE Strain Standardization Task Force," *JACC Cardiovasc. Imaging*, vol. 11, no. 1, pp. 15–24, 2018, doi: 10.1016/j.jcmg.2017.01.027.

[65] Nina C. Wunderlich, Herald Küx, Felix Kreidel, Ralf Birkemeyer, and Robert J. Siegel, "The Changing Paradigm in the Treatment of Structural Heart Disease and the Need for the Interventional Imaging Specialist," *Interv. Cardiol.*, vol. 11, no. 2, pp. 135–139, 2016, doi: 10.15420/icr.2016:12:2.

[66] M. Marwan, F. Ammon, D. Bittner, J. Röther, N. Mekkhala, M. Hell, A. Schuhbaeck, G. Gitsioudis, R. Feyrer, C. Schlundt, S. Achenbach, and M. Arnold, "CT-derived left ventricular global strain in aortic valve stenosis patients: A comparative analysis pre and post transcatheter aortic valve implantation," *J. Cardiovasc. Comput. Tomogr.*, vol. 12, no. 3, pp. 240–244, 2018, doi: 10.1016/j.jcct.2018.01.010.

[67] Stéphane Lafitte, Raymond Roudaut, Erwan Donal, Amira Zaroui, Adrien Salem, Severine Monzy, Patricia Reant, Cecile Hamon, Gilbert Habib, and Aude Mignot, "Global Longitudinal Strain as a Major Predictor of Cardiac Events in Patients with Depressed Left Ventricular Function: A Multicenter Study," *J. Am. Soc. Echocardiogr.*, vol. 23, no. 10, pp. 1019–1024, 2010, doi: 10.1016/j.echo.2010.07.019.

[68] Jeptha P. Curtis, Seth I. Sokol, Yongfei Wang, Saif S. Rathore, Dennis T. Ko, Farid Jadbabaie, Edward L. Portnay, Stephen J. Marshalko, Martha J. Radford, and Harlan M. Krumholz, "The association of left ventricular ejection fraction, mortality, and cause of death in stable outpatients with heart failure," *J. Am. Coll. Cardiol.*, vol. 42, no. 4, pp. 736–742, 2003, doi: 10.1016/S0735-1097(03)00789-7.

[69] Marco R. Di Tullio, Min Qian, John L. P. Thompson, Arthur J. Labovitz, Douglas L. Mann, Ralph L. Sacco, Patrick M. Pullicino, Ronald S. Freudenberger, John R. Teerlink, Susan Graham, Gregory Y. H. Lip, Bruce Levin, J. P. Mohr, Richard Buchsbaum, Conrado J. Estol, Dirk J. Lok, Piotr Ponikowski, Stefan D. Anker, and Shunichi Homma, "Left Ventricular Ejection Fraction and Risk of Stroke and Cardiac Events in Heart Failure: Data from the Warfarin Versus Aspirin in Reduced Ejection Fraction Trial," *Stroke*, vol. 47, no. 8, pp. 2031–2037, 2016, doi: 10.1161/STROKEAHA.116.013679.

[70] Patricia A. Pellikka, Lilin She, Thomas A. Holly, Grace Lin, Padmini Varadarajan, Robert O. Bonow, Hussein R. Al-Khalidi, Salvador Borges-Neto, Daniel S. Berman, Julio A. Panza, David L. Prior, Paul Grayburn, Patrice Desvigne-Nickens, Kerry L. Lee, Eric J. Velazquez, Ramdas G. Pai, Karol Miszalski-Jamka, Gerald M. Pohost, Federico M. Asch, and Jae K. Oh, "Variability in Ejection Fraction Measured By Echocardiography, Gated Single-Photon Emission Computed Tomography, and Cardiac Magnetic Resonance in Patients With Coronary Artery Disease and Left Ventricular Dysfunction," *JAMA Netw. Open*, vol. 1, no. 4, p. e181456, 2018, doi: 10.1001/jamanetworkopen.2018.1456.

[71] Cristian Mornoş, Athanasios Manolis, Dragos Cozma, Nikos Kouremenos, Ioanna Zacharopoulou, and Adina Ionac, "The Value of Left Ventricular Global Longitudinal Strain Assessed by Three-Dimensional Strain Imaging in the Early Detection of

Anthracycline- Mediated Cardiotoxicity," *Hell. J. Cardiol.*, vol. 55, pp. 235–244, 2014.

[72] Mads Ersbøll, Nana Valeur, Ulrik Madvig Mogensen, Mads Jønsson Andersen, Jacob Eifer Møller, Eric J. Velazquez, Christian Hassager, Peter Søgaard, and Lars Køber, "Prediction of all-cause mortality and heart failure admissions from global left ventricular longitudinal strain in patients with acute myocardial infarction and preserved left ventricular ejection fraction," *J. Am. Coll. Cardiol.*, vol. 61, no. 23, pp. 2365–2373, 2013, doi: 10.1016/j.jacc.2013.02.061.

[73] Paaladinesh Thavendiranathan, Frédéric Poulin, Ki Dong Lim, Juan Carlos Plana, Anna Woo, and Thomas H. Marwick, "Use of myocardial strain imaging by echocardiography for the early detection of cardiotoxicity in patients during and after cancer chemotherapy: A systematic review," *J. Am. Coll. Cardiol.*, vol. 63, no. 25 PART A, pp. 2751–2768, 2014, doi: 10.1016/j.jacc.2014.01.073.

[74] Colin O. Wu, Kihei Yoneyama, Eui-Young Choi, Joao A. C. Lima, Andre L. C. Almeida, Anders Opdahl, Sirisha Donekal, Raymond T. Yan, Boaz D. Rosen, Antoinette S. Gomes, Veronica R. S. Fernandes, and David A. Bluemke, "Prognostic value of myocardial circumferential strain for incident heart failure and cardiovascular events in asymptomatic individuals: the Multi-Ethnic Study of Atherosclerosis," *Eur. Heart J.*, vol. 34, no. 30, pp. 2354–2361, 2013, doi: 10.1093/eurheartj/eht133.

[75] Ify Mordi, Hiram Bezerra, David Carrick, and Nikolaos Tzemos, "The combined incremental prognostic value of LVEF, late gadolinium enhancement, and global circumferential strain assessed by cmr," *JACC Cardiovasc. Imaging*, vol. 8, no. 5, pp. 540–549, 2015, doi: 10.1016/j.jcmg.2015.02.005.

[76] Goo Yeong Cho, Thomas H. Marwick, Hyun Sook Kim, Min Kyu Kim, Kyung Soon Hong, and Dong Jin Oh, "Global 2-Dimensional Strain as a New Prognosticator in Patients With Heart Failure," *J. Am. Coll. Cardiol.*, vol. 54, no. 7, pp. 618–624, 2009, doi: 10.1016/j.jacc.2009.04.061.

[77] Elliot R. McVeigh, Amir Pourmorteza, Michael Guttman, Veit Sandfort, Francisco Contijoch, Suhas Budhiraja, Zhennong Chen, David A. Bluemke, and Marcus Y. Chen, "Regional myocardial strain measurements from 4DCT in patients with normal LV function," *J. Cardiovasc. Comput. Tomogr.*, vol. 12, no. 5, pp. 372–378, 2018, doi: 10.1016/j.jcct.2018.05.002.

[78] Amir Pourmorteza, Karl H. Schuleri, Daniel A. Herzka, Albert C. Lardo, and Elliot R. McVeigh, "A New Method for Cardiac Computed Tomography Regional Function Assessment: SQUEEZ," *Circ Cardiovasc Imaging*, vol. 5, pp. 243–250, 2012, doi: 10.1161/CIRCIMAGING.111.970061.

[79] M. S. Amzulescu, M. De Craene, H. Langet, A. Pasquet, D. Vancraeynest, A. C. Pouleur, J. L. Vanoverschelde, and B. L. Gerber, "Myocardial strain imaging: review of general principles, validation, and sources of discrepancies," *Eur. Hear. J. - Cardiovasc. Imaging*, vol. 32, pp. 1–15, 2019, doi: 10.1093/ehjci/jez041.

[80] Pengcheng Shi, Albert J. Sinusas, R. Todd Constable, Erik Ritman, and James S. Duncan, "Point-tracked quantitative analysis of left ventricular surface motion from 3-D image sequences," *IEEE Trans. Med. Imaging*, vol. 19, no. 1, pp. 36–50, 2000, doi: 10.1109/42.832958.

[81] Ping Yan, Albert Sinusas, and James S. Duncan, "Boundary element method-based regularization for recovering of LV deformation," *Med. Image Anal.*, vol. 11, no. 6, pp. 540–554, 2007, doi: 10.1016/j.media.2007.04.007.

[82] Francisco J. Contijoch, Daniel W. Groves, Zhennong Chen, Marcus Y. Chen, and Elliot R. McVeigh, “A novel method for evaluating regional RV function in the adult congenital heart with low-dose CT and SQUEEZ processing,” *Int. J. Cardiol.*, vol. 249, pp. 461–466, 2017, doi: 10.1016/j.ijcard.2017.08.040.

[83] Marcus Y. Chen and Andrew E. Arai, “submillisievert Median radiation Dose for coronary angiography with a second-generation,” *Radiology*, vol. 267, no. 1, pp. 76–85, 2013, doi: 10.1148/radiol.13122621/-/DC1.

[84] Amir Pourmorteza, Marcus Y. Chen, Jesper van der Pals, Andrew E. Arai, and Elliot R. McVeigh, “Correlation of CT-based regional cardiac function (SQUEEZ) with myocardial strain calculated from tagged MRI: an experimental study,” *Int. J. Cardiovasc. Imaging*, vol. 32, no. 5, pp. 817–823, 2016, doi: 10.1007/s10554-015-0831-7.

[85] Paul A. Yushkevich, Joseph Piven, Heather Cody Hazlett, Rachel Gimpel Smith, Sean Ho, James C. Gee, and Guido Gerig, “User-guided 3D active contour segmentation of anatomical structures: Significantly improved efficiency and reliability,” *Neuroimage*, vol. 31, no. 3, pp. 1116–1128, 2006, doi: 10.1016/j.neuroimage.2006.01.015.

[86] Nobuyuki Otsu, “A Threshold Selection Method from Gray-Level Histograms,” *IEEE Trans. Syst. Man. Cybern.*, vol. 9, no. 1, pp. 62–66, 2008, doi: 10.1109/tsmc.1979.4310076.

[87] Gabrielle Colvert, Ashish Manohar, Brendan Colvert, Andrew Schluchter, Francisco Contijoch, and Elliot R. McVeigh, “Novel measurement of LV twist using 4DCT: quantifying accuracy as a function of image noise,” *Med. Imaging 2019 Biomed. Appl. Mol. Struct. Funct. Imaging*, no. March, p. 54, 2019, doi: 10.1117/12.2512532.

[88] Juan E. Ortuño-Fisac, Gonzalo Vegas-Sánchez-Ferrero, Juan J. Gómez-Valverde, Marcus Y. Chen, Andrés Santos, Elliot R. McVeigh, and María J. Ledesma-Carbayo, “Automatic estimation of aortic and mitral valve displacements in dynamic CTA with 4D graph-cuts,” *Med. Image Anal.*, vol. 65, p. 101748, 2020, doi: 10.1016/j.media.2020.101748.

[89] A. Myronenko and X. Song, “Point set registration: Coherent point drift,” *IEEE Trans. Pattern Anal. Mach. Intell.*, vol. 32, no. 12, pp. 2262–2275, 2010, [Online]. Available: http://www.ncbi.nlm.nih.gov/pubmed/20975122%0Ahttp://ieeexplore.ieee.org/ielx5/34/5611449/05432191.pdf?tp=&arnumber=5432191&isnumber=5611449.

[90] Amir Pourmorteza, Noemie Keller, Richard Chen, Albert Lardo, Henry Halperin, Marcus Y. Chen, and Elliot McVeigh, “Precision of regional wall motion estimates from ultra-low-dose cardiac CT using SQUEEZ,” *Int. J. Cardiovasc. Imaging*, vol. 34, no. 8, pp. 1277–1286, 2018, doi: 10.1007/s10554-018-1332-2.

[91] Jeroen J. Bax, Philippe Debonnaire, Patrizio Lancellotti, Nina Ajmone Marsan, Laurens F. Tops, James K. Min, Niccolo Piazza, Jonathon Leipsic, Rebecca T. Hahn, and Victoria Delgado, “Transcatheter Interventions for Mitral Regurgitation: Multimodality Imaging for Patient Selection and Procedural Guidance,” *JACC Cardiovasc. Imaging*, vol. 12, no. 10, pp. 2029–2048, 2019, doi: 10.1016/j.jcmg.2019.03.036.

[92] Anders Sommer, Mads Brix Kronborg, Bjarne Linde Nørgaard, Steen Hvitfeldt, Kirsten Bouchelouche, Morten Böttcher, Henrik Kjærulf Jensen, Jesper Møller Jensen, Jens Kristensen, Christian Gerdes, Peter Thomas Mortensen, and Jens Cosedis Nielsen, “Multimodality imaging-guided left ventricular lead placement in cardiac resynchronization therapy : a randomized controlled trial,” *Eur. J. Heart Fail.*, vol. 18, pp. 1365–1374, 2016, doi: 10.1002/ejhf.530.

[93] Paul A. Yushkevich, Artem Pashchinskiy, Ipek Oguz, Suyash Mohan, J. Eric Schmitt, Joel M. Stein, Dženan Zukić, Jared Vicory, Matthew McCormick, Natalie Yushkevich, Nadav Schwartz, Yang Gao, and Guido Gerig, "User-Guided Segmentation of Multi-modality Medical Imaging Datasets with ITK-SNAP," *Neuroinformatics*, vol. 17, no. 1, pp. 83–102, 2019, doi: 10.1007/s12021-018-9385-x.

[94] Hari K. Narayan, Ronghui Xu, Nickolas Forsch, Sachin Govil, David Iukuridze, Lanie Lindenfeld, Eric Adler, Sanjeet Hegde, Adriana Tremoulet, Bonnie Ky, Saro Armenian, Jeffrey Omens, and Andrew D. McCulloch, "Atlas-based measures of left ventricular shape may improve characterization of adverse remodeling in anthracycline-exposed childhood cancer survivors: a cross-sectional imaging study," *Cardio-Oncology*, vol. 6, no. 1, pp. 1–9, 2020, doi: 10.1186/s40959-020-00069-5.

[95] Kathleen Gilbert, Wenjia Bai, Charlene Mauger, Pau Medrano-Gracia, Avan Suinesiaputra, Aaron M. Lee, Mihir M. Sanghvi, Nay Aung, Stefan K. Piechnik, Stefan Neubauer, Steffen E. Petersen, Daniel Rueckert, and Alistair A. Young, "Independent Left Ventricular Morphometric Atlases Show Consistent Relationships with Cardiovascular Risk Factors: A UK Biobank Study," *Sci. Rep.*, vol. 9, no. 1, pp. 1–9, 2019, doi: 10.1038/s41598-018-37916-6.

[96] Genevieve Farrar, Avan Suinesiaputra, Kathleen Gilbert, James C. Perry, Sanjeet Hegde, Alison Marsden, Alistair A. Young, Jeffrey H. Omens, and Andrew D. McCulloch, "Atlas-based ventricular shape analysis for understanding congenital heart disease," *Prog. Pediatr. Cardiol.*, vol. 43, pp. 61–69, 2016, doi: 10.1016/j.ppedcard.2016.07.010.

[97] R. Blomley, M. Weinmann, J. Leitloff, and B. Jutzi, "Shape distribution features for point cloud analysis – a geometric histogram approach on multiple scales," *ISPRS Ann. Photogramm. Remote Sens. Spat. Inf. Sci.*, vol. II–3, no. September, pp. 9–16, 2014, doi: 10.5194/isprsannals-ii-3-9-2014.

[98] Jonathan M. Behar, Ronak Rajani, Amir Pourmorteza, Rebecca Preston, Orod Razeghi, Steve Niederer, Shaumik Adhya, Simon Claridge, Tom Jackson, Ben Sieniewicz, Justin Gould, Gerry Carr-White, Reza Razavi, Elliot McVeigh, and Christopher Aldo Rinaldi, "Comprehensive use of cardiac computed tomography to guide left ventricular lead placement in cardiac resynchronization therapy," *Hear. Rhythm*, 2017, doi: 10.1016/j.hrthm.2017.04.041.

[99] Mihaela Silvia Amzulescu, Hélène Langet, Eric Saloux, Alain Manrique, Laurianne Boileau, Alisson Slimani, Pascal Allain, Clotilde Roy, Christophe de Meester, Agnès Pasquet, Mathieu De Craene, David Vancraeynest, Anne Catherine Pouleur, Jean Louis J. Vanoverschelde, and Bernhard L. Gerber, "Head-to-Head Comparison of Global and Regional Two-Dimensional Speckle Tracking Strain Versus Cardiac Magnetic Resonance Tagging in a Multicenter Validation Study," *Circ. Cardiovasc. Imaging*, vol. 10, no. 11, pp. 1–11, 2017, doi: 10.1161/CIRCIMAGING.117.006530.

[100] Michael R. Gold, Ulrika Birgersdotter-Green, Jagmeet P. Singh, Kenneth A. Ellenbogen, Yinghong Yu, Timothy E. Meyer, Milan Seth, and Patrick J. Tchou, "The relationship between ventricular electrical delay and left ventricular remodelling with cardiac resynchronization therapy," *Eur. Heart J.*, vol. 32, no. 20, pp. 2516–2524, 2011, doi: 10.1093/eurheartj/ehr329.

[101] Jagmeet P. Singh, Ronald D. Berger, Rahul N. Doshi, Michael Lloyd, Douglas Moore, and Emile G. Daoud, "Rationale and design for ENHANCE CRT: QLV implant strategy for non-left bundle branch block patients," *ESC Hear. Fail.*, vol. 5, no. 6, pp. 1184–1190, 2018, doi: 10.1002/ehf2.12340.

[102] Katherine C. Wu, “A CURE for What Ails in Cardiac Resynchronization Therapy: Defibrillator or Pacemaker Only?,” *JACC Cardiovasc. Imaging*, vol. 13, no. 4, pp. 937–939, 2020, doi: 10.1016/j.jcmg.2019.11.013.A.

[103] Zhennong Chen, Marzia Rigolli, Davis Marc Vigneault, Seth Kligerman, Lewis Hahn, Anna Narezkina, Amanda Craine, Katherine Lowe, and Francisco Contijoch, “Automated Cardiac Volume Assessment and Cardiac Long- and Short-Axis Imaging Plane Prediction from ECG-gated CT Volumes Enabled By Deep Learning,” *Eur. Hear. J. - Digit. Heal.*, no. 858, 2021, doi: 10.1093/ehjdh/ztab033.

[104] Rainer Hoffmann, Giuseppe Barletta, Stephan Von Bardeleben, Jean Louis Vanoverschelde, Jaroslaw Kasprzak, Christian Greis, and Harald Becher, “Analysis of left ventricular volumes and function: A multicenter comparison of cardiac magnetic resonance imaging, cine ventriculography, and unenhanced and contrast-enhanced two-dimensional and three-dimensional echocardiography,” *J. Am. Soc. Echocardiogr.*, vol. 27, no. 3, pp. 292–301, 2014, doi: 10.1016/j.echo.2013.12.005.

[105] Peter W. Wood, Jonathan B. Choy, Navin C. Nanda, and Harald Becher, “Left ventricular ejection fraction and volumes: It depends on the imaging method,” *Echocardiography*, vol. 31, no. 1, pp. 87–100, 2014, doi: 10.1111/echo.12331.

[106] Sebastian Lehner, Christopher Uebleis, Franziska Schüßler, Alexander Haug, Stefan Kääb, Peter Bartenstein, Serge D. Van Kriekinge, Guido Germano, Heidi Estner, and Marcus Hacker, “The amount of viable and dyssynchronous myocardium is associated with response to cardiac resynchronization therapy: Initial clinical results using multiparametric ECG-gated [18F]FDG PET,” *Eur. J. Nucl. Med. Mol. Imaging*, vol. 40, no. 12, pp. 1876–1883, 2013, doi: 10.1007/s00259-013-2516-6.

[107] Manuel D. Cerqueira, Neil J. Weissman, Vasken Dilsizian, Alice K. Jacobs, Sanjiv Kaul, Warren K. Laskey, Dudley J. Pennell, John A. Rumberger, Thomas Ryan, and Mario S. Verani, “Standardized Myocardial Segmentation and Nomenclature for Tomographic Imaging of the Heart,” pp. 539–542, 2002.

[108] Vikas Gupta, Jonas Lantz, Lilian Henriksson, Jan Engvall, Matts Karlsson, Anders Persson, and Tino Ebbers, “Automated three-dimensional tracking of the left ventricular myocardium in time-resolved and dose-modulated cardiac CT images using deformable image registration,” *J. Cardiovasc. Comput. Tomogr.*, vol. 12, no. 2, pp. 139–148, 2018, doi: 10.1016/j.jcct.2018.01.005.

[109] Yuki Tanabe, Teruhito Kido, Akira Kurata, Shun Sawada, Hiroshi Suekuni, Tomoyuki Kido, Takahiro Yokoi, Teruyoshi Uetani, Katsuji Inoue, Masao Miyagawa, and Teruhito Mochizuki, “Three-dimensional maximum principal strain using cardiac computed tomography for identification of myocardial infarction,” *Eur. Radiol.*, vol. 27, no. 4, pp. 1667–1675, 2017, doi: 10.1007/s00330-016-4550-9.

[110] Yechiel Lamash, Anath Fischer, Shemy Carasso, and Jonathan Lessick, “Strain analysis from 4-D cardiac CT image data,” *IEEE Trans. Biomed. Eng.*, vol. 62, no. 2, pp. 511–521, 2015, doi: 10.1109/TBME.2014.2359244.

[111] Ashish Manohar, Gabrielle M. Colvert, Andrew Schluchter, Francisco Contijoch, and Elliot R. McVeigh, “Anthropomorphic left ventricular mesh phantom: a framework to investigate the accuracy of SQUEEZ using Coherent Point Drift for the detection of regional wall motion abnormalities,” *J. Med. Imaging*, vol. 6, no. 04, p. 1, 2019, doi: 10.1117/1.jmi.6.4.045001.

[112] Gabrielle M. Colvert, Juan E. Ortuño, W. Patricia Bandettini, Marcus Y. Chen, María J.

Ledesma-Carbayo, and Elliot R. McVeigh, “4DCT-Derived Endocardial Left Ventricular Torsion Correlates With CMR Tagging–Derived Torsion in the Same Subjects,” *JACC Cardiovasc. Imaging*, vol. 13, no. 12, pp. 2677–2678, 2020, doi: 10.1016/j.jcmg.2020.05.022.

[113] Vahid Tavakoli and Nima Sahba, “Assessment of age-related changes in left ventricular twist by 3-dimensional speckle-tracking echocardiography.,” *J. Ultrasound Med.*, vol. 32, no. 8, pp. 1435–41, 2013, doi: 10.7863/ultra.32.8.1435.

[114] Ashish Manohar, Gabrielle Colvert, Andrew Schluchter, Francisco Contijoch, and Elliot R. McVeigh, “LV systolic point-cloud model to quantify accuracy of CT derived regional strain,” *Med. Imaging 2019 Image-Guided Proced. Robot. Interv. Model.*, no. March, p. 13, 2019, doi: 10.1117/12.2512635.

[115] Jing Shi, Cuizhen Pan, Dehong Kong, Leilei Cheng, and Xianhong Shu, “Left Ventricular Longitudinal and Circumferential Layer-Specific Myocardial Strains and Their Determinants in Healthy Subjects,” *Echocardiography*, vol. 33, no. 4, pp. 510–518, 2016, doi: 10.1111/echo.13132.

[116] G. Kocabay, D. Muraru, D. Peluso, U. Cucchini, S. Mihaila, S. Padayattil-Jose, D. Gentian, S. Iliceto, D. Vinereanu, and L. P. Badano, “Normal left ventricular mechanics by two-dimensional speckle-tracking echocardiography. Reference values in healthy adults. [Spanish]\rMecanica ventricular izquierda normal mediante ecocardiografi a speckle tracking bidimensional. Valores de referencia pa,” *Rev. Esp. Cardiol.*, vol. 67, no. 8, pp. 651–658, 2014, doi: 10.1016/j.recesp.2013.12.011.

[117] Christopher C. Moore, Elliot R. McVeigh, and Elias A. Zerhouni, “Quantitative tagged magnetic resonance imaging of the normal human left ventricle,” *Topics in Magnetic Resonance Imaging*, vol. 11, no. 6. pp. 359–371, 2000, doi: 10.1097/00002142-200012000-00005.

[118] Clément Charbonnel, Raphaele Convers-Domart, Sophie Rigaudeau, Anne Laure Taksin, Nicolas Baron, Juliette Lambert, Stéphanie Ghez, Jean-Louis Georges, Hassan Farhat, Jérôme Lambert, Philippe Rousselot, and Bernard Livarek, “Assessment of global longitudinal strain at low-dose anthracycline-based chemotherapy, for the prediction of subsequent cardiotoxicity,” *Eur. Hear. J. – Cardiovasc. Imaging*, p. jew223, 2017, doi: 10.1093/ehjci/jew223.

[119] Marie-pierre Jolly, Jennifer H. Jordan, Giselle C. Meléndez, Gary R. Mcneal, Ralph B. D. Agostino Jr, and W. Gregory Hundley, “Automated assessments of circumferential strain from cine CMR correlate with LVEF declines in cancer patients early after receipt of cardio-toxic chemotherapy,” pp. 1–12, 2017, doi: 10.1186/s12968-017-0373-3.

[120] Cristian Mornoş and Lucian Petrescu, “Early detection of anthracycline-mediated cardiotoxicity: the value of considering both global longitudinal left ventricular strain and twist [1],” *Can. J. Physiol. Pharmacol.*, vol. 91, no. 8, pp. 601–607, 2013, doi: 10.1139/cjpp-2012-0398.

[121] Eric J. Stöhr, Rob E. Shave, Aaron L. Baggish, and Rory B. Weiner, “Left ventricular twist mechanics in the context of normal physiology and cardiovascular disease: a review of studies using speckle tracking echocardiography,” *Am. J. Physiol. - Hear. Circ. Physiol.*, vol. 311, no. 3, pp. H633–H644, 2016, doi: 10.1152/ajpheart.00104.2016.

[122] Luigi P. Badano and Denisa Muraru, “Twist Mechanics of the Left Ventricle,” *Circ. Cardiovasc. Imaging*, vol. 12, no. 4, pp. 1–3, 2019, doi: 10.1161/circimaging.119.009085.

[123] Geert Litjens, Thijs Kooi, Babak Ehteshami Bejnordi, Arnaud Arindra Adiyoso Setio,

Francesco Ciompi, Mohsen Ghafoorian, Jeroen A. W. M. van der Laak, Bram van Ginneken, and Clara I. Sánchez, “A survey on deep learning in medical image analysis,” *Med. Image Anal.*, vol. 42, no. December 2012, pp. 60–88, 2017, doi: 10.1016/j.media.2017.07.005.

[124] Yefeng Zheng, Bogdan Georgescu, Adrian Barbu, Michael Scheuering, and Dorin Comaniciu, “Four-chamber heart modeling and automatic segmentation for 3D cardiac CT volumes,” *Med. Imaging 2008 Image Process.*, vol. 6914, no. 11, p. 691416, 2008, doi: 10.1117/12.770710.

[125] Chunliang Wang and Örjan Smedby, “Automatic whole heart segmentation using deep learning and shape context,” *Lect. Notes Comput. Sci. (including Subser. Lect. Notes Artif. Intell. Lect. Notes Bioinformatics)*, vol. 10663 LNCS, pp. 242–249, 2018, doi: 10.1007/978-3-319-75541-0_26.

[126] Ashish Manohar, Gabrielle M. Colvert, Andrew Schluchter, Francisco Contijoch, and Elliot R. McVeigh, “Anthropomorphic left ventricular mesh phantom: a framework to investigate the accuracy of SQUEEZ using Coherent Point Drift for the detection of regional wall motion abnormalities,” *J. Med. Imaging*, vol. 6, no. 04, p. 1, 2019, doi: 10.1117/1.jmi.6.4.045001.

[127] Maria J. Ledesma-Carbayo, J. Andrew Derbyshire, Smita Sampath, Andrés Santos, Manuel Desco, and Elliot R. McVeigh, “Unsupervised estimation of myocardial displacement from tagged MR sequences using nonrigid registration,” *Magn. Reson. Med.*, vol. 59, no. 1, pp. 181–189, 2008, doi: 10.1002/mrm.21444.

[128] Fusako Sera, Tomoko S. Kato, Maryjane Farr, Cesare Russo, Zhezhen Jin, Charles C. Marboe, Marco R. Di Tullio, Donna Mancini, and Shunichi Homma, “Left ventricular longitudinal strain by speckle-tracking echocardiography is associated with treatment-requiring cardiac allograft rejection,” *J. Card. Fail.*, vol. 20, no. 5, pp. 359–364, 2014, doi: 10.1016/j.cardfail.2014.02.006.

[129] Robert H. Helm, Christophe Leclercq, Owen P. Paris, Cengizhan Ozturk, Elliot McVeigh, Albert C. Lardo, and David A. Kass, “Cardiac dyssynchrony analysis using circumferential versus longitudinal strain: Implications for assessing cardiac resynchronization,” *Circulation*, vol. 111, no. 21, pp. 2760–2767, 2005, doi: 10.1161/CIRCULATIONAHA.104.508457.

[130] Kihei Yoneyama, Ola Gjesdal, Eui Young Choi, Colin O. Wu, W. Gregory Hundley, Antoinette S. Gomes, Chia Ying Liu, Robyn L. McClelland, David A. Bluemke, and Joao A. C. Lima, “Age, sex, and hypertension-related remodeling influences left ventricular torsion assessed by tagged cardiac magnetic resonance in asymptomatic individuals: The multi-ethnic study of atherosclerosis,” *Circulation*, vol. 126, no. 21, pp. 2481–2490, 2012, doi: 10.1161/CIRCULATIONAHA.112.093146.

[131] Miho Fukui, Paul Sorajja, Mario Gössl, Richard Bae, John R. Lesser, Benjamin Sun, Alison Duncan, David Muller, and João L. Cavalcante, “Left Ventricular Remodeling After Transcatheter Mitral Valve Replacement With Tendyne: New Insights From Computed Tomography,” *JACC Cardiovasc. Interv.*, vol. 13, no. 17, pp. 2038–2048, 2020, doi: 10.1016/j.jcin.2020.06.009.

[132] Frits W. Prinzen, William C. Hunter, Bradley T. Wyman, and Elliot R. McVeigh, “Mapping of regional myocardial strain and work during ventricular pacing: Experimental study using magnetic resonance imaging tagging,” *J. Am. Coll. Cardiol.*, vol. 33, no. 6, pp. 1735–1742, 1999, doi: 10.1016/S0735-1097(99)00068-6.

[133] Jincun Guo, Linlin Li, Guosheng Xiao, Tao Ye, Xinyi Huang, Fanqi Meng, Qiang Li, Simei Chen, and Binni Cai, “Remarkable response to cardiac resynchronization therapy via left bundle branch pacing in patients with true left bundle branch block,” *Clin. Cardiol.*, vol. 43, no. 12, pp. 1460–1468, 2020, doi: 10.1002/clc.23462.

[134] Sarah J. Dixon and Richard G. Brereton, “Comparison of performance of five common classifiers represented as boundary methods: Euclidean Distance to Centroids, Linear Discriminant Analysis, Quadratic Discriminant Analysis, Learning Vector Quantization and Support Vector Machines, as dependent on,” *Chemom. Intell. Lab. Syst.*, vol. 95, no. 1, pp. 1–17, 2009, doi: 10.1016/j.chemolab.2008.07.010.

[135] Yuichi Notomi, Randolph M. Setser, Takahiro Shiota, Maureen G. Martin-Miklovic, Joan A. Weaver, Zoran B. Popović, Hirotsugu Yamada, Neil L. Greenberg, Richard D. White, and James D. Thomas, “Assessment of left ventricular torsional deformation by Doppler tissue imaging: Validation study with tagged magnetic resonance imaging,” *Circulation*, vol. 111, no. 9, pp. 1141–1147, 2005, doi: 10.1161/01.CIR.0000157151.10971.98.

[136] Jonathan Sorger, Bradley T. Wyman, Owen P. Faris, William C. Hunter, and Elliot R. McVeigh, “Torsion of the Left Ventricle During Pacing with MRI Tagging,” *J Cardiovasc Magn Reson.*, vol. 5, no. 4, pp. 521–530, 2003.

[137] Dimosthenis Pandis, Partho P. Sengupta, Javier G. Castillo, Giuseppe Caracciolo, Gregory W. Fischer, Jagat Narula, Anelechi Anyanwu, and David H. Adams, “Assessment of longitudinal myocardial mechanics in patients with degenerative mitral valve regurgitation predicts postoperative worsening of left ventricular systolic function,” *J. Am. Soc. Echocardiogr.*, vol. 27, no. 6, pp. 627–638, 2014, doi: 10.1016/j.echo.2014.02.008.

[138] Chiara Sartori, Anna Degiovanni, Federica Devecchi, Paolo Devecchi, and Paolo Nicola Marino, “Acute Modifications of Left Ventricular Torsional Mechanics Induced by Cardiac Resynchronization Therapy Affect Short-Term Reverse Remodeling,” *Circ. J.*, vol. 83, no. 2, pp. 386–394, 2019, doi: 10.1253/circj.cj-18-0858.

[139] Leyla Elif Sade, Özlem Demir, Ilyas Atar, and Haldun Müderrisoglu, “Effect of Mechanical Dyssynchrony and Cardiac Resynchronization Therapy on Left Ventricular Rotational Mechanics,” 2008, doi: 10.1016/j.amjcard.2007.11.069.

[140] Matteo Bertini, Partho P. Sengupta, Gaetano Nucifora, Victoria Delgado, Arnold C. T. Ng, Nina Ajmone Marsan, Miriam Shanks, Rutger R. J. van Bommel, Martin J. Schalij, Jagat Narula, and Jeroen J. Bax, “Role of Left Ventricular Twist Mechanics in the Assessment of Cardiac Dyssynchrony in Heart Failure,” *JACC Cardiovasc. Imaging*, vol. 2, no. 12, pp. 1425–1435, 2009, doi: 10.1016/j.jcmg.2009.09.013.

[141] Manuel García-Villalba, Lorenzo Rossini, Alejandro Gonzalo, Davis Vigneault, Pablo Martinez-Legazpi, Eduardo Durán, Oscar Flores, Javier Bermejo, Elliot McVeigh, Andrew M. Kahn, and Juan C. del Álamo, “Demonstration of Patient-Specific Simulations to Assess Left Atrial Appendage Thrombogenesis Risk,” *Front. Physiol.*, vol. 12, no. February, pp. 1–14, 2021, doi: 10.3389/fphys.2021.596596.

[142] Andrew Schluchter, Chelsea Jan, Katherine Lowe, Davis Vigneault, Francsico Contijoch, and Elliot R. McVeigh, “A Vascular Landmark-Based Method for Highly Reproducible Measurement of Left Atrial Appendage Volume in CT,” *Circ Cardiovasc Imaging*, vol. 12, no. 12, 2019, doi: 10.1161/CIRCIMAGING.119.009075.A.

[143] Brian R. Lindman, Catherine M. Otto, Pamela S. Douglas, Rebecca T. Hahn, Sammy Elmariah, Neil J. Weissman, William J. Stewart, Girma M. Ayele, Feifan Zhang, Alan

Zajarias, Hersh S. Maniar, Hasan Jilaihawi, Eugene Blackstone, Khaja M. Chinnakondepalli, E. Murat Tuzcu, Martin B. Leon, and Philippe Pibarot, “Blood Pressure and Arterial Load after Transcatheter Aortic Valve Replacement for Aortic Stenosis,” *Circ. Cardiovasc. Imaging*, vol. 10, no. 7, pp. 1–12, 2017, doi: 10.1161/CIRCIMAGING.116.006308.

[144] Raquel Yotti, Javier Bermejo, Enrique Gutiérrez-Ibañes, Candelas Pérez Del Villar, Teresa Mombiela, Jaime Elízaga, Yolanda Benito, Ana González-Mansilla, Alicia Barrio, Daniel Rodríguez-Pérez, Pablo Martínez-Legazpi, and Francisco Fernández-Avilés, “Systemic vascular load in calcific degenerative aortic valve stenosis: Insight from percutaneous valve replacement,” *J. Am. Coll. Cardiol.*, vol. 65, no. 5, pp. 423–433, 2015, doi: 10.1016/j.jacc.2014.10.067.

[145] Liam Ring, Yasir Abu-Omar, Nikki Kaye, Bushra S. Rana, William Watson, David P. Dutka, and Vassilios S. Vassiliou, “Left Atrial Function Is Associated with Earlier Need for Cardiac Surgery in Moderate to Severe Mitral Regurgitation: Usefulness in Targeting for Early Surgery,” *J. Am. Soc. Echocardiogr.*, vol. 31, no. 9, pp. 983–991, 2018, doi: 10.1016/j.echo.2018.03.011.